TWO PHOTON AND TWO COLOUR IONIZATION OF ATOMS IN INTENSE EXTREME-UV AND OPTICAL LASER FIELDS

A THESIS SUBMITTED FOR THE DEGREE OF

DOCTOR OF PHILOSOPHY

PRESENTED TO:

THE SCHOOL OF PHYSICAL SCIENCES,
FACULTY OF SCIENCE AND HEALTH,
DUBLIN CITY UNIVERSITY

AUTHOR

VINCENT RICHARDSON

B. Sc. Hons.

Research Supervisors

PROF. JOHN COSTELLO, DR. MICHAEL MEYER

January 2011

Declaration

I hereby certify that this material, which I now submit for assessment on the programme of study leading to the award of Doctor of Philosophy, Ph.D. is entirely my own work, that I have exercised reasonable care to ensure that the work is original, and does not to the best of my knowledge breach any law of copyright, and has not been taken from the work of others save and to the extent that such work has been cited and acknowledged with the text of my work.

Signed: _____ **ID No.:** 52303434

Date: _____

Acknowledgements

I would like to thank first of all my supervisors Prof. John Costello and Dr. Michael Meyer for their continuous support and guidance. Many thanks are due to everyone from Ireland, Germany and France who have been patient with me whilst I have slowly learned basic atomic physics over the past three years or so.

I wish to thank the members of the physics department for making my time here enjoyable - Séamus, Éanna, Jiang Xi, Conor C, Colm 'The Fallon' Fallon, Mossy, Dara, Paddy K, Mairead, Ruth, Jack, Joe, Pat, Paddy H, Subhash, Brian and Catherine. Thanks also to past group members, Pádraig, Conor Mc, John D. and Caroline. I sincerely wish everyone good luck in the future.

I wish to thank the many people I had the pleasure of collaborating with over the past three years. I am indebted to all those who have contributed to and guided the experiments contained in this work, in particular Denis Cubaynes (Paris), Mathias Richter (Berlin), Wenbin Li (Shanghai), Stefan Duesterer, Paul Radcliffe, Andrei Sorokin (Hamburg), Hugo van der Hart (Belfast) and Lampros Nikolopoulos (Dublin). I am very grateful to have had the chance to work with many talented and enthusiastic scientists, all of whom were very willing to share with me their skills and knowledge and answer my questions. Thanks also to everyone who has helped me prepare manuscripts, posters and talks for trips and conferences.

Finally, I wish to thanks my friends and family for the support that allowed this work to be completed, despite my poor attempts to explain what on earth it was I studied. Special thanks to Emma for keeping me happy, and for letting me leave for weeks at a time.

Abstract

Inner shell ionization and excitation in atoms has been studied extensively for many decades using a variety of ultraviolet and X-ray light sources, especially, but not exclusively, synchrotrons. In addition, the study of multiphoton absorption by outer (valence) electrons rapidly followed the development of sufficiently intense optical and infrared laser systems. The advent of intense EUV and X-ray Free Electron Lasers (FELs), based on the principle of Self Amplifed Spontaneous Emission (SASE), has enabled the study of multiphoton ionization of inner shell electrons for the first time. Results on the interaction of intense and ultrashort extreme ultraviolet FEL pulses with a specific focus on multiphoton ionization of neon, krypton and xenon are presented in this thesis. As a guide, some common FEL parameters utilised as part of experiments presented here included pulse energies of up to 50 μJ with average (envelope) durations of 30 fs for photon energies of 46 eV and 93 eV, with a beam diameter of typically 3 mm (unfocused) and focussed spot sizes of < 50 μm. A tightly focused FEL beam at 93 eV hence results in intensities on the order of 10^{16} Wcm^{-2}

In a complementary experiment, ionization of a Ne^+ target by combining EUV radiation from FLASH with an intense, synchronized optical laser was investigated. The ejected electrons undergo stimulated emission and absorption in the presence of the IR field, creating so-called 'sidebands' in the photoelectron spectrum. It was found that the photoelectron spectra exhibit a strong dependence on the relative polarisation of the two fields as well as the magnetic substates of the residual doubly-charged ionic core. This experiment utilised a second, IR laser, the pulses of which were spatially and temporally overlapped with those of the FEL. For reference, the 800 nm IR laser was operated in both 'long' (3 ps) and 'short' (120 fs) pulse modes, with 'long' mode used for coarse synchronisation purposes. Typically, the IR laser was focused to a spot size on the order of 50 μm.

List of Figures

Contents

Chapter 1

Introduction - Free Electron Lasers and Elements of Photoionization

This chapter is divided into two distinct sections. In Part I, the topic of Free Electron Lasers is introduced, while in Part II a number of key features of photoionization are discussed.

1.1 Part I - FEL Theory and Operation: An Historic Perspective

A vacuum-UV (VUV) free electron laser (FEL), operating at the then record short wavelength of 98 nm was reported by DESY in 2000 [1]. Gigawatt peak power was achieved soon afterwards [2]. A milestone was reached in 2006, when, whilst operating at the then shortest wavelength of 13.7 nm, a signal from the 5th harmonic of the fundamental wavelength (evidence of lasing at 2.7 nm) was detected [3]. It was the world's first example of a coherent radiation source capable of reaching far into the water window. The development of this new, high brilliance light source permits the study of the structure and dynamics of matter under intense irradiance at unprecedented high photon energies and ultrafast (femtosecond) timescales. Among other applications, the diffractive imaging of macromolecules is possible as the high intensity and ultrashort pulsewidth allow one to record a diffractive image with high signal to noise ratio in a single FEL shot before the molecule fragments.

The first reference to what would be recognised today as an FEL can be traced to the paper by Pantell, Soncini, and Puthoff [4], in which the authors postulated that stimulated Compton scattering of a relativistic electron beam by a periodic transverse magnetic field could be used to obtain lasing action. Using the theory

of relativity, it was deduced that the emitted radiation from the electrons would be blueshifted to shorter wavelengths in the observer's (or laboratory) frame by a factor inversely proportional to γ, where $\gamma = \frac{1}{(1-v^2/c^2)}$ and v and c have the usual meanings (further details are given later). Building on this principle, the first workable system was proposed in 1971 [5]. Experimental results were subsequently obtained from the first FEL single pass amplifier [6] and oscillator [7] systems operating in the optical wavelength regime.

Subsequently, a theoretical framework was developed by Kroll and McMullin which pointed towards the possibility of achieving positive single-pass gain [8] and which correctly stated that amplification of the emitted radiation was due to the ponderomotive microbunching of the electron beam. The first proposal to use the FEL collective instability to produce optical radiation using a single-pass amplifier starting from shot noise, was published by Kondratenko and Saldin in 1979 [9] with a followup paper in 1980 [10]. Single-pass amplification with start-up from noise was also investigated by Bonifacio, Pellegrini, and Narducci [11].

Bonifacio et al. [12] first used the term self amplified spontaneous emission (SASE) in connection with an FEL amplifier starting from shot noise. In 1986, Kim [13], conducted a full 3D analysis of the spontaneous emission characteristics of relativistic electrons as a function of distance along the undulator length and predicted both the exponential gain in output power, as well as the onset of saturation. Briefly, an undulator consists of a linear arrangement of magnets, in which the north-south pole orientation alternates. The resultant periodic magnetic field forces incoming electron beams to undergo a small amplitude oscillation, causing radiation emission.

In 1982 Derbenev, Kondratenko, and Saldin first proposed to use the instability in a single-pass amplifier starting from shot noise for a soft XFEL [14]. They suggested the use of a storage ring to provide the electron beam, as at that time storage rings delivered the highest electron beam quality. A similar proposal was discussed by Murphy and Pellegrini in 1985 [15]. At that stage, the shortest lasing wavelength was considered to be in the region of 10 nm, due to, among other things, the electron beam quality.

An important milestone was reached in 1992, when it was proposed by Pellegrini to use a radio frequency (RF) photocathode electron gun (to produce high charge density electron bunches) in conjunction with a two-mile section of the Stanford linear accelerator (linac), to produce lasing in the Soft X-ray region i.e. $<$10 nm [16]. It was directly as a result of this proposal that the American Linac Coherent Light Source (LCLS) project came into existence. Shortly afterwards, it was reported that high gain had been reached by a single pass SASE system operating

in the IR regime where a gain of 10^5 was achieved [17]. This was the first demonstration of the SASE FEL mechanism. After many years of development, efforts to produce saturated gain using a SASE FEL were successful. In 2000, a group at Argonne National Laboratory (ANL) demonstrated gain in a visible (390 nm) SASE FEL [18]. In 2001, the VISA collaboration, between Brookhaven National Laboratory (BNL), University of California Los Angeles (UCLA) and the Stanford Linear Accelerator Centre (SLAC), demonstrated lasing and saturated gain at 830 nm [19]. As mentioned above, in September 2001, the VUV-FEL at DESY demonstrated lasing and saturated gain at 98 nm [2]. In January 2002, saturation was achieved at 82 nm [20], and in 2005 lasing at 32 nm was demonstrated [21]. THE VUV-FEL facility at DESY continued to record shorter and shorter wavelengths, finally reaching the so-called 'water window' in 2007 [3] (in fact, it was the fifth harmonic of the 13.5 nm fundamental that was recorded inside the water window, at 2.7 nm). This region is known as the 'water window' since water molecules are transparent there - this is crucial to the field of biological imaging. The VUV-FEL Facility was renamed FLASH, The Free Electron Laser, Hamburg in 2005.

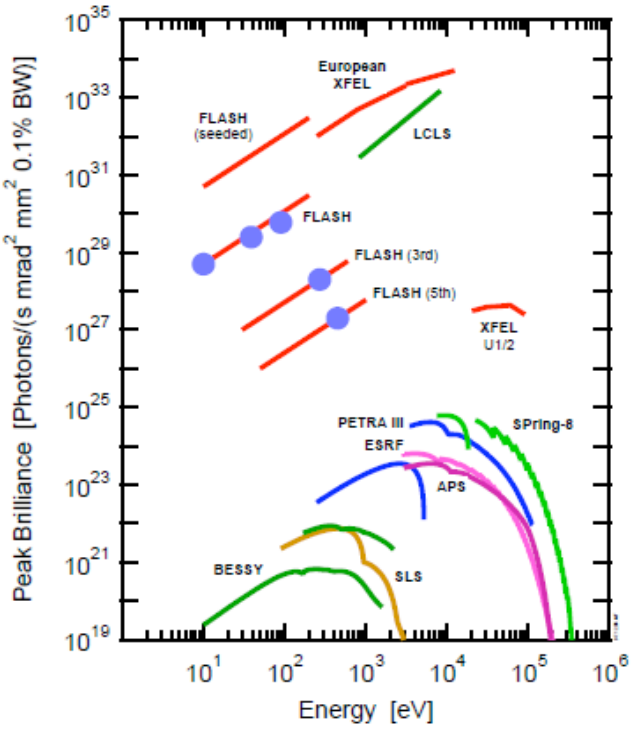

Figure 1.1: Peak brilliance of XFELs versus third generation SR light sources. Full blue circles show experimental performance of FLASH at DESY in summer 2006 at 13.5 nm and its harmonics [3].

At the time of writing (late 2010), FLASH routinely lases deep in the EUV, pro-

ducing 4.45 nm photons in pulses of duration in the range of 10 fs to 300 fs, at pulse energies approaching 100 μJ. LCLS, meanwhile, recently hosted the first user experiments, in which this author took part (Nov. '09), providing x-ray photons with energies up to 2 keV at impressive pulse energies on the order of millijoules, in similarly short pulse lengths of 50 to 250 fs. 2014 will see the commissioning of the XFEL, the European X-Ray Free Electron Laser in Hamburg. It plans to lase at up to 12.4 keV region by accelerating electron bunches to energies of up to 17.5 GeV. See Fig. 1.1 where the expected XFEL operating range is compared with other FELs and synchrotron facilities.

1.1.1 FEL LINAC

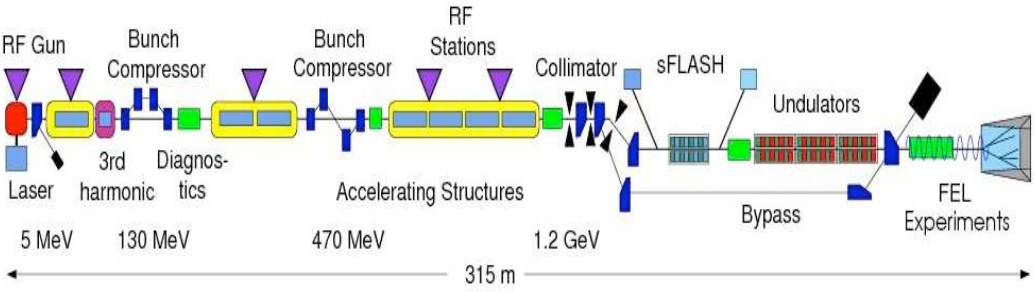

Figure 1.2: Layout of the EUV-FEL beamline at the FLASH facility.

Shown in Fig. 1.2 is the layout of the FEL at FLASH. From left to right, the RF gun consists of a photoinjector (Sec. 1.1.2) which creates electron bunches with energies on the order of 5 MeV. This is followed by a series of accelerating structures (Sec. 1.1.3) which bring the electron bunch energy up to around 1 GeV. The bunch compressors (Sec. 1.1.3) compensate for the natural dispersion experienced by the bunches as they traverse the accelerating modules. Finally, the undulators (Sec. 1.1.4) force the relativistic electron beam through a periodic transverse magnetic field, where it is forced to perform a slalom-type motion. The acceleration of the electrons along this path results in the emission of photons. An FEL can reach the resonant gain regime and saturate in a single pass along the undulator. The wavelength of the emitted radiation can be tuned using the electron beam energy and the magnetic field strength of the undulator, as can be seen from Eqn. 1.1

$$\lambda_{FEL} = \frac{\lambda_u}{2\gamma^2}(1 + \frac{K^2}{2}) \tag{1.1}$$

where λ_u is the undulator period in millimetres, K = e$B_u\lambda_u/2\pi m_e$c is the undulator parameter, B_u is the rms value of the undulator field in Tesla, and γ = E/$m_e c^2$

is the relativistic factor. The principles underlying FEL operation are discussed in more detail in Sec. 1.1.4.

1.1.2 The Photoinjector

The initial electron bunches are required to be extremely small spatially, have a high current density and in addition a small energy spread. This was made possible by the development of a radio frequency (RF) electron gun, originally intended for use in linear collider experiments. Briefly a photocathode in the photoinjector is irradiated with a train of laser pulses (pulse duration: 10 ps) from a neodymium: yttrium-lithium-fluoride (Nd:YLF) laser to produce a train of electron bunches. The cathode is usually made of molybdenum and coated with a thin Cs_2Te layer to achieve a quantum efficiency for photoelectron emission of typically 5 - 10%. A high power accelerating RF electric field on the order of 40 MV/m imparts enough energy to the emitted electrons to transfer them to the accelerator stage.

The relatively long exciting laser pulse (10 ps) is chosen to ensure that the inherent high density of the electron bunch does not lead to instabilities. The 50 A collimated bunch, however, needs to be accelerated as soon as possible in order to minimise the effects of electrostatic repulsion. The electron bunches enter the accelerator module at a repetition frequency of 5 - 10 Hz, carrying a charge of typically less than 1 nC per bunch, and are usually several hundred microns in length.

It is at this point that the temporal 'jitter' of the FEL pulse train is introduced, as photoemission from the cathode is essentially a random process. The electron bunches generated have current densities that are temporally and spatially out of phase. That is, the electrons are not concentrated or localised in any systematic way within the bunches. This essentially has the effect of making it impossible for lasing to occur at the exact same point in the undulator for all electron bunches, the result of which manifests itself in stochastically distributed temporal separation of the emitted radiation. The pulse to pulse jitter, at the time of writing, on the order of 500 fs.

1.1.3 Electron Acceleration & Bunch Compression

High peak currents of several kiloamperes are needed for extreme-ultraviolet and X-ray free-electron laser action. These cannot be produced directly in the electron gun. Therefore, moderately long bunches with a peak current of about 50 A are created in the source. As it is difficult to increase the charge density further due to space charge effects, the bunches are instead compressed longitudinally.

At FLASH, the electron injector section is followed by five 12-meter-long ac-

celerator modules containing eight superconducting cavities cooled by superfluid helium. The cavities are made from pure niobium and consist of nine cells. The electron bunches are accelerated in the linear accelerator (LINAC) to relativistic velocities as quickly as possible, in order to prevent the electrons in the bunch from drifting apart due to the mutual repulsion between the negative charges.

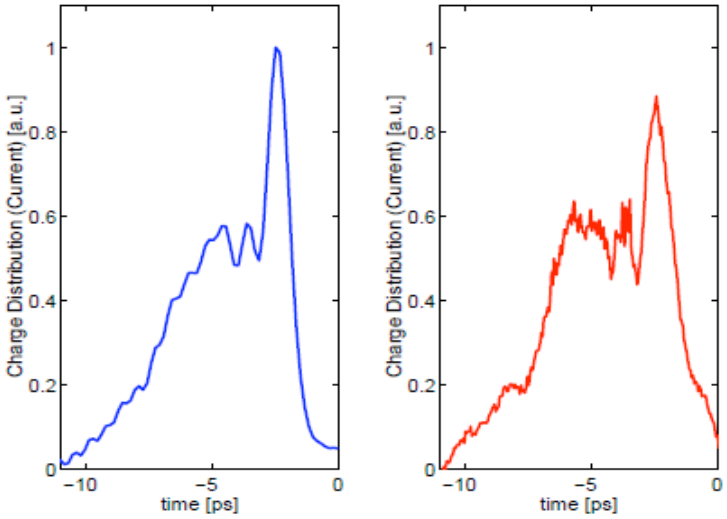

Figure 1.3: Longitudinal profile of the electron bunches as measured with two different methods. On the left hand side [22] the profile is deduced from a diffractive imaging measurement, whilst on the right hand side [23] the profile is derived from a streaking technique.

The subsequent spatial bunch compression is achieved via the use of two magnetic chicanes [24, 25] (see Fig.1.2). The phase of the driving RF field is adjusted such that the bunch is accelerated on the rising edge of the pulse. This introduces a slight energy chirp and results in those electrons at the tail of the bunch receiving a slight energy increase relative to those at the front of the bunch. By the end of the chicane, in which higher energy electrons take a shorter path, the electrons initially at the tail of the bunch have caught up with those at the front resulting in spatial, and concomitant temporal, compression. Using a phase difference of 10° a bunch of length of 2.5 mm can expect to be compressed by a factor of approximately five i.e. 0.5 mm.

Finally the result is an electron bunch containing a narrow leading spike with a width of less than 100 femtoseconds containing approximately 10%-20% of the total bunch charge (Fig. 1.3). This is followed by the remaining part of the bunch which extends to a few picoseconds in duration. This leading spike provides the high peak currents necessary (on the order of many kiloamps) to initiate the SASE process in the undulator, while the long tail does not possess sufficient beam current to generate any significant FEL gain.

By varying the parameters of the bunch compressors (mainly the RF voltage, the RF phase and the chicane path length) it was possible to control the width of the lasing fraction of the electron bunch, resulting in a controlled variation of the radiation pulse length between 30 fs and 100 fs [26]. However, in 'normal' operation, that is, during routine user operation, the pulse length is not varied.

1.1.4 The Undulator

The electron bunch exiting the LINAC enters the 30 m long undulator chain, having been accelerated to $\sim$ 1 GeV, and compressed longitudinally during its flight. As each relativistic bunch traverses the periodic magnetic field of the undulator it is forced to travel in an oscillatory path. The electrons begin to emit on-axis radiation in a narrow bandwidth around a resonance wavelength λ_{FEL} given by Eq. 1.1, and repeated here for convenience:

$$\lambda_{FEL} = \frac{\lambda_u}{2\gamma^2}(1 + \frac{K^2}{2}) \tag{1.2}$$

where λ_u is the undulator period in millimetres, K = eB$_u\lambda_u/2\pi m_e$c is the undulator parameter, B$_u$ is the rms value of the undulator field in Tesla, and γ = E/m$_e$c^2 = 1957.E$_e$ [GeV] is the relativistic factor. A sample calculation using some typical FEL operating parameters is given here. A 1 GeV bunch results in a γ of 1957. K equals 1.198 for a B$_u$ of .47 T and a λ_u of 2.73 cm. This gives λ_{FEL} a value of approximately 7 nm. For a complete derivation, see Chapter 5 of reference [27]. This leads to a resonance condition that occurs when the radiation field leads the electron bunch by a distance λ after one undulator period.

1.1.5 FEL Radiation

The resonance condition described above occurs after a single pass of the bunch through the undulator. The SASE radiation has a typical bandwidth of 0.5-1% and is highly collimated, with a divergence of less than 1 mrad. The temporal structure of a typical FEL pulse from FLASH is shown in Fig. 1.4. The typical repetition rate is 5 Hz (but can be as high as 10 Hz), which is equivalent to the macro bunch rate i.e. users can request single (one micro bunch per macro bunch) or multi bunch macropulses. As many as 800 microbunches can be requested per pulse. Depending on the beamline, the FEL spot size varies from 100 μm (FWHM) if unfocussed [28] to $\sim$ 3μm (FWHM) if focussed with a high quality normal incidence multilayer mirror [29]. The output of a SASE FEL is usually quoted in terms of its peak brilliance (see Fig. 1.1) and is in units of photons/s/mm^2/mrad^2/0.1% BW, where 0.1% BW denotes a bandwidth of $10^{-3}\nu$ centred around the frequency ν. Brilliance

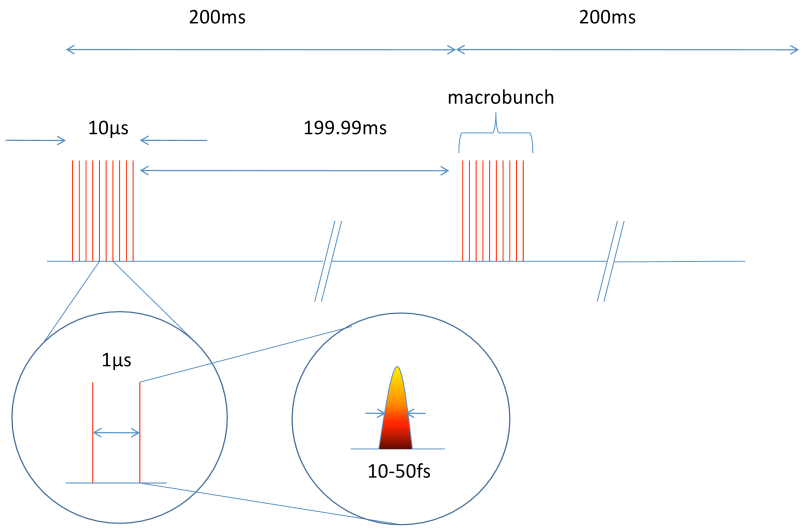

Figure 1.4: Pulse structure of the FLASH FEL operating at a macropulse repetition rate of 5 Hz. In this example, each macrobunch of 10 μs duration contains 10 micropulses. Each micropulse is due to a single electron microbunch and is separated by 1μs from neighbouring micropulses. The number of microbunches is variable, as is the temporal separation of microbunches within the macrobunch [28].

takes into account the photon flux (photons per second in a given bandwidth), and also the high phase-space density of the photons, i.e. a small effective source area which is highly collimated.

Since the exponential amplification process in a SASE FEL starts from spontaneous emission (shot noise) in the electron bunch, the SASE FEL radiation itself is of a stochastic nature, meaning that individual radiation pulses differ in their intensity, temporal structure and spectral distribution.

The key to the SASE-FEL process is the interaction of the electrons within each bunch with the radiation field generated in the undulator. As the electrons travel through the undulator on their oscillatory trajectories, the transverse component of their motion will couple to the transverse electric field of the radiation, causing an energy transfer between the electron and the light wave. This coupling is critically dependent on the high charge density within the bunch. The 'FEL instability' arises as a result of the interaction between the electron and the radiation field and leads to an instability in the electron bunch. Depending on the phase of the electron with respect to the radiation field it may either be accelerated or decelerated by the field, leading to a periodic velocity modulation of the electrons within the beam with a period equal to the wavelength λ of the applied radiation field [30]. This periodic

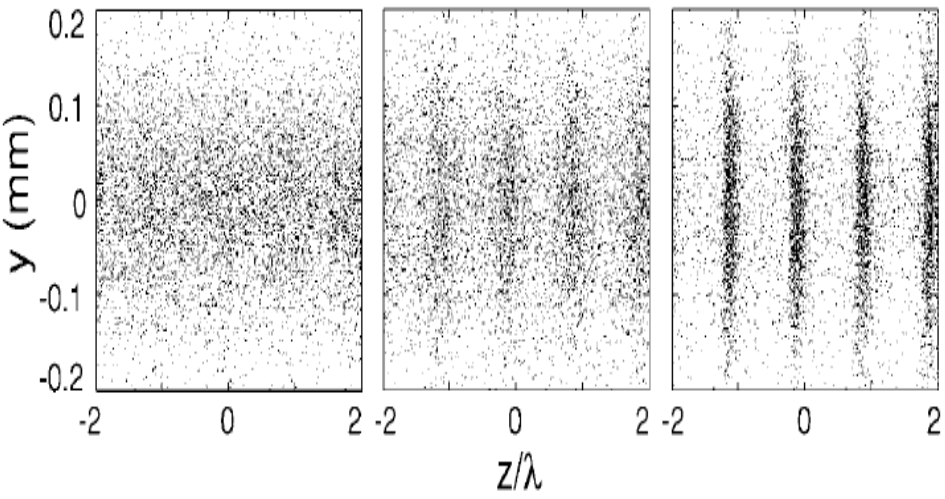

Figure 1.5: Simulation of the density modulation of the electron beam as it progresses along the undulator. Each microbunch becomes modulated in this way as it interacts with the radiation field. The peaks are separated by λ, meaning photons emitted at each peak add coherently. Left: at the entrance to the undulator, Centre: in the middle of the exponential growth regime, Right: at the undulator exit.) [30].

velocity modulation leads to a longitudinal density modulation of the electrons, as can seen in Fig.1.5. This modulation is the key to coherent photon emission.

1.2 Part II - Photionization of Atoms

The study of the photoionization of atoms has provided many fundamental insights into light - matter interactions for radiation in the UV to X-ray band of the electromagnetic spectrum. This interaction, in the most basic sense, has the potential to provide detailed information on the structure of atoms, molecules and solids, specifically, the structure and arrangement of the electrons. The photoelectric effect involves a photon of sufficient energy knocking an electron out of an atom, as first discovered by Hertz in 1887 [31]. The subsequent electron yield is dependent on many factors, including the photon energy and bandwidth of the light source, the binding energy or work function of the electronic subshell or metal under investigation, and inter / intra-subshell electron - electron correlation effects.

Electron spectroscopy can be broadly classified into three modes - Photoelectron Spectroscopy (PES), Constant Final State (CFS) Spectroscopy, and Constant Initial / Ionic State (CIS) Spectroscopy. The experimental method used in this thesis is PES, in which for a fixed photon energy $h\nu$, all photoemitted electrons over a range of kinetic energies are collected, typically with a time-of-flight (TOF) spectrometer [32, 33, 34]. In CFS, the photon energy is scanned and only electrons with a select

kinetic energy are collected. This is also known as the Constant Kinetic Energy (CKE) method. For this purpose, Hemispherical Deflection Analysers (HDA) [35] are often used (although other detectors based on the principles of electrostatic deflection to measure only electrons with a specific energy, such as Cylindrical Mirror Analysers (CMA) may also be suitable. See [36] for an early example). In CIS, both $h\nu$ and the kinetic energy window are scanned incrementally, such that the value E_k - $h\nu$ is constant.

There are a number of reasons for using TOF PES. Firstly, it allows one to sample a whole energy spectrum simultaneously. As will be seen later, this property facilitated the collection of individual photoelectron spectra, each generated by a single laser pulse. Secondly, by employing retarding fields of different values at the entrance of the TOF, one is able to detect both high and low kinetic energy electrons with good resolution (albeit not always simultaneously). Retarding fields can of course be used for other analysis methods. Initial experiments in the field were limited to measuring the total electron yield (see, for example, [37], whilst more sophisticated experiments were made possible later on with the development of spectrometer systems that allowed energy resolved measurements to be made (see [38] for one of many early examples). Time-of-Flight (TOF) spectrometry allowed electron spectra to be recorded, in which partial ionization yields (i.e. yields from different electronic subshells) could be recorded and compared. Further improvements in experimental techniques led to the development of angle resolved electron spectrometry, in which the angular distribution of emitted photoelectrons could be analysed. As a result, in conducting a modern photoionization experiment, one could expect to obtain high resolution, angularly resolved partial and total cross section measurements of atomic beams.

1.2.1 Photoionization Cross Sections

The probability of ionization of an atomic system by electromagnetic radiation is given by the value of the total photoionization cross section. This value is generally expressed as a function of incident photon energy. A useful measurement is the partial cross section, in which emitted electrons are ascribed to their initial electron orbital. Furthermore, electron lines in the spectra can additionally be subdivided into satellite or 'shake' lines (Sec. 1.2.2.1), and Auger electron lines (Sec. 1.2.4). Some of these are illustrated in Fig.1.6.

The cross section for a photoionizing transition (that is, a transition in which the final state is in the continuum) with unpolarised electromagnetic radiation of energy $h\nu$ is given by Eq. 1.3 [39]

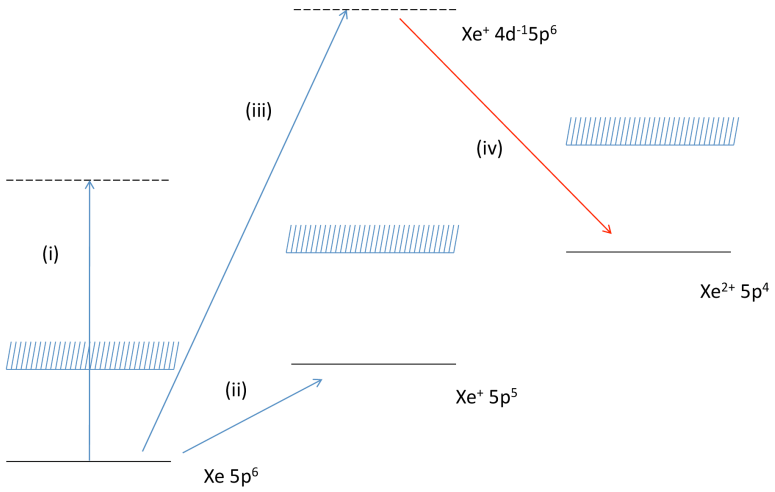

Figure 1.6: An energy level diagram is presented here outlining some of the photoionization terms used throughout this work. (i) Excitation, (ii) ionization (iii) Inner shell ionization (iv) Auger Decay.

$$\sigma_{if}(h\nu) = \frac{4\pi^2 \alpha a_0^2 (h\nu)}{3} |M_{if}|^2 \tag{1.3}$$

where α is the fine structure constant, a_0 is the Bohr radius, and $h\nu$ is the incident photon energy [39]. The term $|M_{if}|$ is the transition matrix element coupling the initial state i and final state f and is essentially a measure of the transition amplitude with the photoelectron line intensity proportional to the square on this value. The transition probability depends on the square of this quantity and is written explicitly as Eq. 1.4 [40]

$$|M_{if}|^2 = |\int_0^\infty R_{\epsilon_2 l_2}(r) r R_{n_1 l_1} r^2 dr|^2 \tag{1.4}$$

where $R_{n,l}$ and $R_{\epsilon,l}$ are well defined radial wavefunctions of the nl^{th} and ϵl^{th} bound (n_1,l_1) and continuum ($\epsilon_2 l_2$) states, and l_2=$l_1 \pm 1$ respectively. Cross sections are generally expressed in units of megabarns (1Mb = 10^{-18}cm^2).

The differential cross section for a given photon energy $h\nu$ is given by [41]

$$\frac{d\sigma_{if}(h\nu)}{d\Omega}(\theta) = \frac{\sigma_{if}(h\nu)}{4\pi}[1 + \beta_{if}(h\nu) P_2(cos\theta)] \tag{1.5}$$

where θ is a measure of the angle between electric field vector of the incoming polarised photon beam and the direction of the outgoing electron. $P_2(\cos\theta)$ is a

second degree Legendre polynomial.

It should be noted that on absorption of a photon of sufficiently high energy, the electron emission is not homogenous over all angles. The angular distribution of photoemitted electrons from a given subshell is described by β, the so-called asymmetry parameter. Another interesting aspect of angle resolved measurements is that it allows one to further characterise the ionization event. An electron promoted above threshold into the continuum is still subject to the rules of angular momentum conservation (the angular momentum of the electron must change by unity i.e. $l\pm$ 1). For example, an electron removed from a p subshell into the continuum can change its angular momentum by one unit and have ϵs or ϵd momenta. Whilst appearing to have the same kinetic energy, the electrons would have very different angular distributions. This interesting property will be examined later in Chapter 5.

By fixing θ at the so called 'magic angle' of 54.7°, the polynomial has a value of zero, meaning that the measurement at this angle is directly proportional to the partial cross section i.e. is not dependent on the angle. In addition, if σ is known for a given angle, measurement of the differential cross section yields the β parameter. On extraction of the β parameter, one can derive the phase shift of the outgoing partial electron waves using the following expression [42]:

$$\beta = \frac{l(l-1)R_{l-1}^2 + (l+1)(l+2)R_{l+1}^2 - 6(l+1)R_{l-1}R_{l+1}cos(\delta_{l+1} - \delta_{l-1})}{(2l+1)[lR_{l-1}^2 + (l+1)R_{l+1}^2]} \tag{1.6}$$

where $R_{l\pm1}$ are solutions to the radial part of the Schrödinger equation.

1.2.2 Correlation Effects and Interchannel Interaction

Of course, the many electron nature of atoms can lead to a drastic modification of the photoionization cross-section. A non-exhaustive list of additional processes that occur as a result of the motion of electrons include autoionization, satellite or 'shake' state formation, Auger decay and Post Collision Interaction (PCI). The production of doubly excited atoms or ions i.e. atoms or ions in which a pair of electrons have been simultaneously promoted, is also a direct result of many-body, 'correlative' effects, as is the formation of doubly charged ions from double electron ejection. New theoretical models have been developed to reproduce these exotic ionization mechanisms. A good overview can be found in [43].

Perhaps the simplest approach to treating photoionization of a single electron is by means of the Hartree-Fock approximation [44]. In this framework, an initial guess is made of the form of the electron orbitals in terms of Hartee-Fock type or-

bitals. These orbitals take into account an average effective potential felt by an electron as a result of the nuclear charge and the field due to neighbouring electrons. This modified potential is known as the Hartree potential. The Fock term takes into account the Pauli exclusion principle, that is, that no two electrons can share the same four quantum numbers. The self - consistent nature of the method refers to the way in which the electron wavefunctions and potential are derived. This method makes an initial guess for the potential usually using screened hydrogenic wavefunctions to construct that starting potential - this potential is subsequently used to obtain an initial estimate of the electron wavefunctions. Subsequently, a new potential is derived. The process is repeated iteratively until a solution for the potential and wavefunctions is converged upon. The removal of an electron, for example, perturbs the self-consistent field, resulting in initial and final states of a transition experiencing different potentials. This method is therefore an improvement on the one-electron approximation.

An improvement to the treatment of the photoionization process came with the development of the Random Phase Approximation (RPA) [45]. In this method, the electron system of an atom is treated as a collective 'electron cloud'. Ionization and vacancy creation lead to perturbations in the cloud resulting in a redistribution of the electron charge, and the launch of collective oscillations. The strength and nature of these oscillations is described in terms of the target 'polarisability'. The description of the ionization process in this fashion allows for the inclusion of more complicated ionization and excitation pathways, such as double excitation (in which two electrons are simultaneously excited, leaving behind a double vacancy). This technique can be further improved by taking into account the interaction between electrons in different subshells, in a framework known as Random Phase Approximation with Exchange (RPAE) [46]. Hence the technique includes both direct removal of an electron by the absorption a photon and indirect removal or excitation of another electron via correlation.

A further modification to the RPA is the Generalised Random Phase Approximation with Exchange (GRPAE). This approach takes into account the change in the electric field felt by an outgoing electron due to the creation of a hole in the corresponding subshell. In addition, this perturbation in the potential affects the states of all the other electrons in the system. The creation of a hole in the subshell, particularly an inner shell hole, leads to an adjustment of the Coloumbic 'screening' felt by outer and continuum electrons. Subsequent relaxation or rearrangement of electrons within shells can lead to further multiple excitation or ionization of the atom. This approach is commonly used in the theoretical treatment of correlated interactions such as autoionization and satellite or shake state formation.

1.2.2.1 Satellite / 'Shake' State Formation

As mentioned in the preceding paragraph, another example of electron correlation is the formation of satellite, or 'shake', states. These occur when an electron is removed from an atom via photoionization. As the electron is ejected, it interacts with another electron and changes its energy. In a shake-up process, an electron is promoted to a higher lying, unfilled orbital, whilst a shake down state involves an electron moving to a state of lower binding energy [47]. A shake off process involves the promotion of the second electron into the continuum (i.e., ionization). An example of such an excitation scheme is shown later in Chapter 3, specifically in Neon. In this case, a neutral Ne target was ionized via Ne $2s^2 2p^6 + h\nu \rightarrow Ne^+ 2s^2 2p^4 nl + e^-$. In this example, one electron has been ejected by absorption of a photon, however the resultant ion has not been left in the ground state configuration - an additional electron from the 2p subshell has been promoted to a higher lying bound state. If the second electron is ejected into the continuum and possesses comparable energies, the two free electrons can interact, and it is this process that is known as Post-Collision Interaction (PCI), leading to a strong modification of the photoionization cross section [48]. Another interesting example of PCI in the case of 1s photoionization in neon: $h\nu$ + Ne$\rightarrow$ $Ne^+(1s^{-1}) + e^-_{photo} \rightarrow Ne^{++}(2p^{-2}) + e^-_{Auger} + e^-_{photo}$. PCI occurs between the photoelectron and the Auger electron. The strength of the interaction depends on the mutual velocities of the emitted electrons and manifests itself in the asymmetric distortion of the line shape and in the shift of their maxima in photoelectron and Auger electron spectra, as seen in [49], for example.

1.2.3 Inner Shell Ionization

Much of the work presented in this thesis involves the interaction of EUV radiation with inner shell electrons. The promotion of tightly bound electrons to either an excited autoionizing state or directly into the continuum and any subsequent relaxation effects lead to many surprising and interesting phenomena. Inner-shell photoionization differs from outer-shell processes in that the relaxation of the ion with an inner-shell vacancy is considerably more complex, even aside from the Auger or X-ray emission processes which result from the filling of the vacancy [43]. From a physical point of view, removal of an outer-shell electron strongly affects the other outer-shell electrons which it partially screens. According to Gauss's law of electrostatics, this electron vacancy exerts no force inside the shell, i.e., on inner-shell electrons. The primary effect, therefore, of the removal of an outer-shell electron on inner shells is a step change in the potential energy [50]. However, removing

an inner-shell electron changes the potential experienced by all electrons in both it's own shell and those at greater radial distances (outer shells) due to screening effects, thereby leading to much more significant relaxation effects.

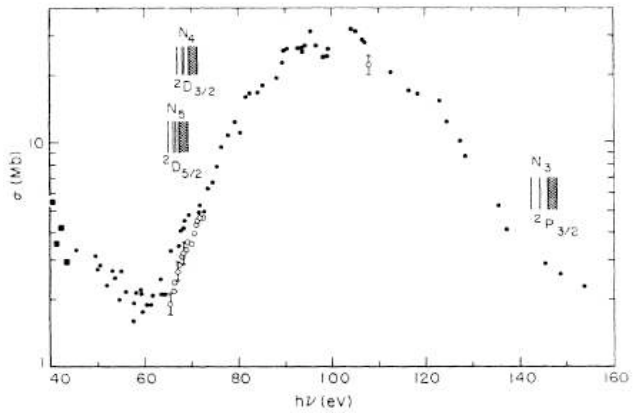

Figure 1.7: Photoionization cross section of Xe in the region from 40 eV to 150 eV. The 4d and 4p ionization thresholds are labelled. The cross section reaches a maximum of approximately 22 Mb at 100 eV, over 30 eV above the 4d ionization threshold [51].

Perhaps the most comprehensive literature reviews on the topic of inner shell photoionization processes are contained within the now, admittedly, not so recent works of Sonntag [52] and Schmidt [53]. In the former, a comprehensive review of EUV spectroscopy of free metal atoms has been compiled, whereas the latter has concentrated on those aspects of spectroscopy involved in the use of synchrotron radiation and rare gas atoms. Several experimental techniques have been employed to record EUV spectra of a range of atoms since the 1960s, including, but not limited to, fluorescence spectroscopy, in which one seeks to detect emitted photons; photoelectron spectroscopy, in which the ejected electrons are the primary source of information; and photoion spectroscopy, in which the resultant ion yield after an excitation or ionization event is recorded. The technique used in this work was photoelectron spectroscopy (PES). Perhaps the first experimental measurement to deal with the inner shell absorption by atoms was that of Madden and Codling [54], in which the 3d and 4d photoabsorption spectra of Kr and Xe respectively were recorded photographically. In the same year, Ederer [51] measured the photoionization cross section of Xe in the region of the 4d-ϵf continuum resonance, and noted the delayed onset of the photoionization maximum. The result is reproduced in Fig. 1.7. Further work on the absorption spectra of neutral atoms was to come from Connerade *et al* in the 70s, a selection of which include a comparision of the absorption spectra of increasingly heavy elements [55], along with spectra in the vacuum ultraviolet region of heavy transition [56, 57, 58] and rare gas [59] elements.

The study of ultraviolet absorption spectroscopy was extended to ionic targets with development of the resonant laser driven ionization (RLDI) [60] and merged beam [61] techniques. Using the electron impact technique, Peart, Dolder and collaborators obtained the first measurements of absolute cross sections for ion targets, notably Rb^+, Cs^+, Ca^+, and Sr^+ [62]. A synchrotron source was subsequently used to obtain high resolution photoionization cross section measurements, as in Ba^+ [63], Ca^+[64] and Sr^+ [65]. More recent cross section measurements have been obtained by the groups of Bizau (a selection of which include Fe^{4+} [66], Xe^+ [67], Xe^{3+} to Xe^{6+} [68] and Si^{4+} [69]), Covington (for example, C^{3+} [70] and Ar^+ [71]) and West (Ca^+ - Ni^+ [72]).

Studies of the photoion yield of ions as a result of vacuum ultraviolet photoexcitation were pioneered by the group of Koizumi *et al*, and some examples are listed below. Using a merged photon-ion beam technique allowed for the study of relative photoion yield of Ba ions following the creation of an inner 4d hole [73], and subsequently Sr ions following direct 3d ionization [74].

A comprehensive review of all work in the field of inner shell spectroscopy is not attempted in this work, however relevant literature surveys have been compiled and can be found at the beginning of Chapters 3, 4 and 5.

1.2.4 Auger Decay

A vacancy created in an inner shell may be filled by an electron from any of the outer subshells. This has a finite probability of occurring as a radiative transition, with a photon carrying away the difference in energy between the two subshells. The probability that an inner shell vacancy decays in this manner is called the fluorescence yield, and is normally of the order of 10^{-4}, hence is considerably more likely that the filling of the inner-hole occurs via a non-radiative transition. If the excess energy is transferred to an electron in one of the other outer subshells giving it enough energy to become unbound and enter into the continuum, this relaxation process is known as the Auger effect and the secondary electron emitted is called the Auger electron [75]. The normal Auger effect can be reasonably well described as a two-step process, leading to double ionization. The manner in which the inner vacancy is filled is described as follows:

- Normal Auger decay: The initial vacancy leads to vacancies in subshells different in n and l, e.g. $3s^{-1} \rightarrow 4s^{-1}\ 4p^{-1}$.
- Coster-Kronig decay: After the decay of the initial vacancy, one of the subsequent two vacancies is in a different subshell of the n^{th} shell of the original vacancy, i.e. same n but different l, e.g. $3s^{-1} \rightarrow 3p^{-1}4s^{-1}$.

- Super Coster-Kronig decay: This refers to a particular case where the initial vacancy in the n^{th} shell leads to two vacancies in subshells from the same n, e.g. $3s^{-1} \rightarrow 3p^{-2}$.

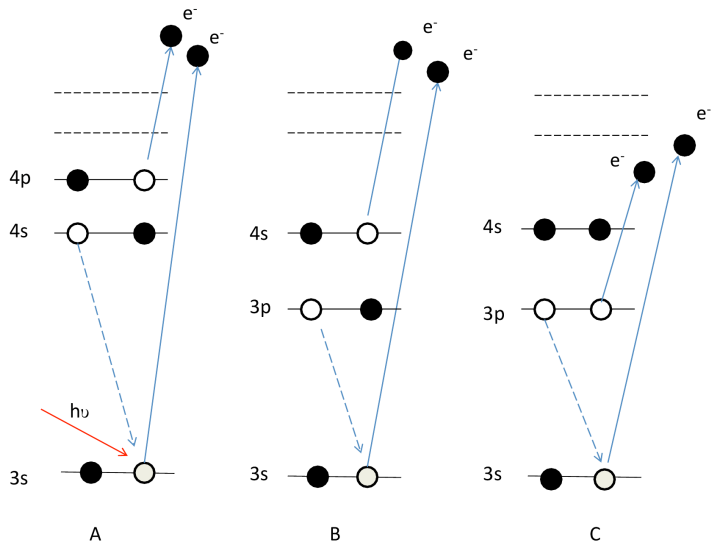

Figure 1.8: Shown schematically here (A) Normal Auger decay, (B) Coster-Kronig decay and finally (C) Super Coster-Kronig decay.

These decay mechanisms are illustrated in Fig.1.8. Auger decay events can be further classified, as illustrated in Fig.1.9, according to the secondary emission process. As can be seen in Fig.1.9, a number of different transitions are possible following inner-shell ionization. 'Normal' Auger decay generally refers to the scheme as shown by 'A', in which the incoming photon has enough energy to completely remove an inner-shell electron. The hole is subsequently filled by an electron from an outer shell, and the excess energy is transferred or released by the emission of a second electron. In the scheme labelled 'B', the incoming photon has an energy such that the inner-shell electron is resonantly excited and promoted to an empty, bound subshell. The bound electron is not freed and does not take part in the secondary emission process. The bound electron is hence referred to as a 'spectator' electron. One such example of this process is given in Chapter 4, in which an inner 3d electron in Kr is resonantly excited via two photon absorption to an unoccupied 4d shell. The excited electron remains bound whilst the hole is filled by a 4p electron. In a second step another 4p electron is subsequently promoted to the continuum. Finally, mechanism 'C' illustrates a 'participator' decay process, in which the excited electron is also the one that plays a role in the subsequent relaxation

process and is released as the secondary electron.

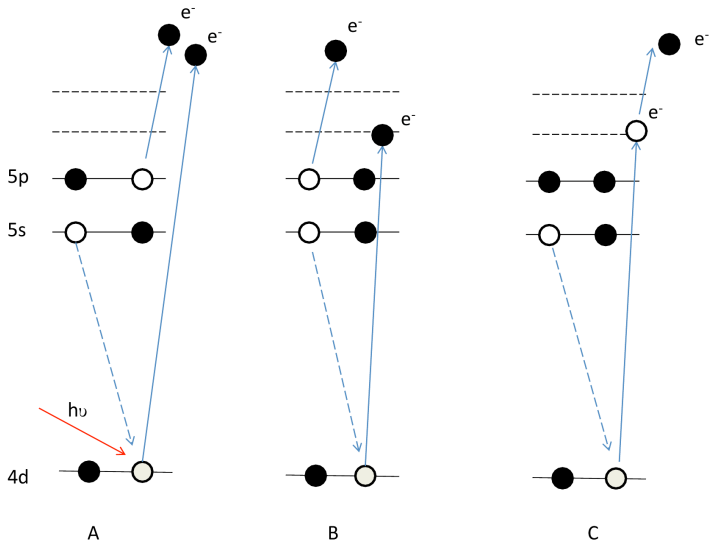

Figure 1.9: Schematic representation of (A) normal Auger decay, (B) spectator Auger decay and finally (C) participator Auger decay.

The decay rate for inner shell excited states is extremely fast, with rates ranging from 10^{12-1}s up to 10^{15-1}s, corresponding to lifetimes of pico- to femtoseconds. This is as compared to valence excited states, which have typical decay rates on the order of $10^{9}s^{-1}$.

1.2.5 Photoionization Maxima

It is now well established that ionization of the d-shells of some elements, do not yield expected absorption edges, but a broad peak extending over tens of eV, and lying far above the photoionization threshold [76]. This effect is known as *delayed onset*. As mentioned previously, this was first seen by Ederer [51] and independently by Lukirskii [77]. The is due to the shape of the positive electrostatic potential energy term in the radial Schrödinger equation [78]

$$V_{eff} = V(r) + \frac{l(l+1)\hbar^2}{2mr^2} \tag{1.7}$$

Goeppert-Mayer first pointed out that, for large values of l i.e. for d or f electrons, this relationship can lead to a double valley profile in the potential [78]. In the case of Xe, the 4d electron must tunnel through a potential barrier, resulting in a photoionization maximum located approximately 30 eV above the ionization threshold, as seen in Fig. 1.7. The theoretical treatment of such a transition was

summarised in the work of Fano and Cooper in [79]. An alternate treatment was proposed by Amusia and co-workers in which the enlarged photoionization cross section was attributed to the resonant excitation of all the electrons in the 4d subshell [80]. Other such examples of delayed onsets or 'shape' resonances are found in the Ba, Ba^{+} and Ba^{2+} [81] and Sr^{+}, Sr^{2+} and Sr^{3+} [82] isonuclear sequences, Ba, La, and Ce [83] and Sm, Eu and Gd [84]. A quite recent review of the subject of 4d photoionization is to be found, in addition to new experimental data for Ce, Nd, Gd, Dy, and Er lanthanide atoms, in [85].

1.2.5.1 Collective Effects

It is now understood that some of the core assumptions invoked in the understanding of the photoelectric effect such as, for example, that single photon processes dominate, and that electrons participate independently in the absorption of light, can break down under certain circumstances [86]. Examples of such circumstances include the use of very strong field lasers, as one can no longer assume only one photon will be absorbed. Another example concerns effects due to the collective response of a group, or even an entire subshell of electrons that occur when the electron-electron interaction is on the same order of magnitude as the electron-nucleus interaction and / or the spin-orbit interaction. Some of the chief manifestations of so-called 'collective effects', or many-body processes is the broadening of giant resonances, simultaneous multielectron excitation or ionization, and various shake processes. In the case of giant resonances, initial attempts to describe them theoretically while assuming that each electron moves within a single common potential were not successful. It was first demonstrated in [87] that, for the case of Xe, the interaction of at all ten electron in the 4d subshell is required in order to achieve sufficient accuracy in the theoretical description of the experimentally measured cross section. Perhaps the best summaries of the associated phenomena are contained in the works of Amusia [80, 43].

1.2.6 Wavefunction Collapse

It is interesting to note that as one moves from Z=54 (Xe) to Z=57 (La), the 4f wavefunction has moved from residing in the outer well to occupying the inner well, as noted in Sec. 1.2.5. This effect is called wavefunction collapse. The layout of the periodic table can be attributed to wavefunction collapse; in Ca I, the ground state is $4s^2$ as opposed to $3d^2$, as the 4s radial wavefunction lies closer to the core within the potential barrier and is hence preferentially filled. As Z increases further, the inner-well region of the effective potential (V_{eff}) becomes deeper and wider, which

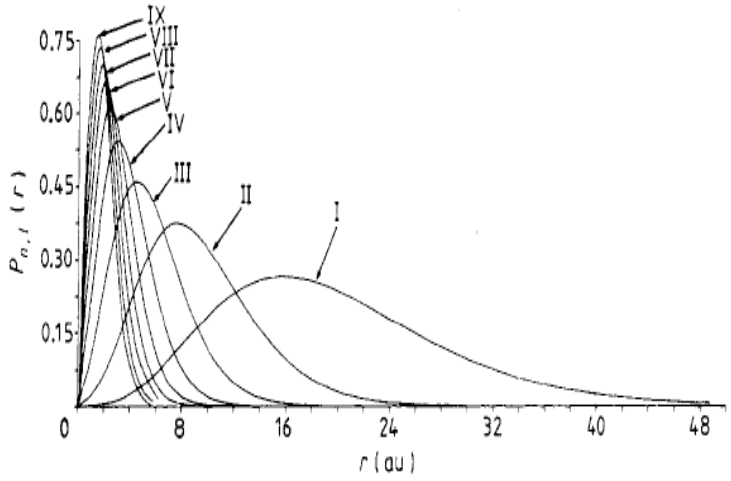

Figure 1.10: The 4f wavefunction of the $4d^9 4f$ excited configuration for the early members of the Xe isonuclear sequence. This is a term dependent calculation i.e. only the 4f radial wavefunction arising from the ^{1}P term is displayed [88]. The numerals I, II refer to the ion stage of Xe, with Xe I indicating neutral Xe.

eventually results in the collapse of the 4d, 5d, nd functions, and the formation of the second, third, n^{th} transition series of elements. The inner well of V_{eff} does not become sufficiently wide and deep to hold the 4f wavefunction until La where the lanthanide series of rare-earth elements begins at Ce. The collapse of the 5f wavefunction marks the beginning of the actinide series of elements. This phenomenon is also responsible for the subsequent sudden increase in binding energies of the 3d, 4d, 5d, 4f and 5f electronic orbitals.

Wavefunction collapse can also occur as a result of increasing ionization along an isonuclear and isoelectronic sequences, not just with increasing Z. This effect is shown in the case of the 4f orbital along the Ba [81, 89] and Xe [88, 90] isonuclear and Xe isoelectronic [91, 92] sequences. In Fig. 1.10, the 4f radial wavefunction for a series of ion cores is displayed. For increasing ionization, it is clear that the contraction and localisation of the square of the wavefunction ($|\Psi_{4f}(r)|^2$) is closer to the core.

1.2.7 Multiphoton Ionization

The field of a monochromatic laser can be imagined as a group of photons each possessing an energy E=$h\nu$ and propagating co-linearly. If such an ensemble of photons meets an atom, the electrons can take up the energy of one or more photons. For example, an atom may absorb two photons simultaneously. In this case, the ionization probability is proportional to the number of pairs of photons. Hence,

the ionization probability will depend on the square of the photon flux, and this is in fact demonstrated experimentally later in Chapters 3 and 4.

The theory of simultaneous two photon absorption was first described by Goeppert-Mayer, in 1931 [93]. In molecular physics, the two photon absorption cross section is ofter given in units of GMs. It is possible to calculate two photon (in fact, n photon) photoionization cross sections [94, 95], by employing an equation similar to equation 1.3. It involves, however, replacement of the one photon transition matrix element with that of an n photon matrix element. The calculation of these transition strengths is entirely non-trivial, requiring the use of time dependent second-order perturbation theory. Recently (2004), the task of computing ionization rates for two photon inner shell ionization was undertaken in the doctoral thesis of Peter Koval [96]. Numerically, the multiphoton ionization cross section takes the form

$$\sigma_{if}(h\nu) = \frac{4\pi^2 \alpha a_0^2 (h\nu)}{3} |M_2^{fi}|^2 \tag{1.8}$$

where M_2^{fi} is the two photon transition matrix element and is written as

$$|M_2^{fi}|^2 = |\sum_v \frac{\langle f| \sum_j r_j |v\rangle \langle v| \sum_j r_j |i\rangle}{E_v - E_i - E_L}|^2 \tag{1.9}$$

where v denotes the intermediate virtual state involved in the two photon transition. For a complete derivation, see [96].

Two-photon excitation occurs at a photon energy of half that required for the one-photon process. The electric dipole transitions now allow two channels and two final states, normally unreachable in one-photon excitation, as the angular momentum coupling condition Δl=$\pm$1 no longer applies (the rule is now Δl=0, $\pm$2). Essentially, a transition must take place between states whose angular momentum is the same, or differs by two units. Two-photon ionization resembles the two photon excitation except that the final state is unbound in the continuum. In addition, a two-photon excitation depends strongly on the polarization of light. For example, the channels s $\rightarrow$ p $\rightarrow$ d and s $\rightarrow$ p $\rightarrow$ s are open in case of linearly polarized light, but only the s $\rightarrow$ p $\rightarrow$ d channel is open for circularly polarized light (with beams of the same helicity) [97, 98].

1.2.7.1 MPI in the Strong Field Regime

At very high intensities, the field of the laser can become strong enough to distort the potential barrier of the nucleus so that the electron may momentarily experience a lower binding energy, in what is commonly referred to as field-ionization [99]. The Keldysh parameter is commonly used as a guide to determine whether a laser

field will induce multiphoton ionization (as described in the preceding paragraph, and examined in detail in Chapters 3 and 4) or tunnelling ionization, in which the electric field of the laser is strong enough (and its frequency low enough) that the electron essentially experiences a quasi-static potential which can be lowered by the laser field. The low frequency of the applied laser field ensures the electron has more time to experience the lowered potential and escape before the potential is restored in the second half of the laser cycle.

The Keldysh parameter γ is a unitless quantity that relates the ionization potential to the ponderomotive energy (U_p) and was introduced to define the transition between the multiphoton and tunnelling regimes [99]. Expressed in atomic units this parameter is defined as Eq.1.10

$$\gamma = \sqrt{\frac{I_p}{2U_p}} \tag{1.10}$$

where U_p is the ponderomotive energy and is given as

$$U_p = 9.337 \times 10^{-20} I_0 \lambda^2 \tag{1.11}$$

with I_0 as the peak laser intensity in units of Wcm^{-2} and λ as the laser wavelength in units of nanometers. Generally speaking, in the case of multiphoton ionization in moderately intense fields or rare gas atoms which have high ionization potentials, U_p is less than the ionization potential, resulting in a large value of γ. In a typical experiment at FLASH, with 93 eV photons (13.3nm) at intensities on the order of 10^{16} Wcm^{-2}, U_p is on the order of 0.2 eV, resulting in $\gamma > 1$ for a Ne atom. Conversely, long wavelength (on the order of hundreds of nm, or μm), high intensity lasers typically result in a value of $\gamma < 1$, and ponderomotive energies comparable to the incident photon energies. An 800 nm IR laser, for example, generating an intensity of 5×10^{14} Wcm^{-2} incident on the same Ne target yields a value of γ = 0.34 as a result of the high ponderomotive energy (on the order of 50 eV, far in excess of the photon energy), indicating the tunnel ionization regime.

1.3 Summary

In the first section of this chapter, an introduction and brief overview of the operation of the Free Electron Laser in Hamburg (FLASH) was presented. Much of the terminology used throughout the rest of the work has been presented. In addition, a brief overview of the theory of photoionization has been compiled, along with a summary of important or landmark experimental measurements over the past few decades.

The next chapter introduces the experimental system, based around the Magnetic Bottle Electron Spectrometer (MBES), used to conduct photoelectron spectroscopy measurements on rare gas targets at FLASH. Two configurations of the system are detailed, (i) introduction of a back-reflecting multilayer mirror to increase the FEL laser intensity in the interaction region and (ii) addition of a second, infrared (IR) laser to study two colour ionization.

Chapter 2

Experimental Systems and Procedures

The experiments detailed in this work concern photoelectron spectroscopy measurements of rare gas targets conducted under high vacuum conditions. Photoelectron detection was carried out using a magnetic bottle-type electron spectrometer. Experiments detailed in Chapters 3, 4 and 5 used almost identical base setups as detailed in [100]. To summarise briefly, those experiments presented in Chapters 3 and 4 utilised a back reflecting multi-layer mirror in order to focus the FEL beam to a point in front of the entrance aperture of a time-of-flight spectrometer. The experiment described in Chapter 5 saw the introduction of a second, 800 nm, IR laser which propagated collinearly with the FEL in the chamber. In this instance, both beams were brought to a common focus in front of the spectrometer entrance aperture without the need for back-reflecting optics.

2.1 Experimental Hall

Fig. 2.1 shows the layout of the FLASH user facility with the FEL as well as THz and bending magnet radiation beamlines entering into the hall from the bottom. The experimental hall is positioned 30 m behind the dipole magnet that separates the electron and the photon beam emerging from the undulator in the accelerator tunnel. The approximately 60 m long photon beam transport system delivers the FEL pulses under ultra-high vacuum (UHV) conditions to five experimental stations. The extreme-ultraviolet pulses are guided to one of five different end stations via evacuated beamlines, held at ultrahigh vacuum in order to minimise losses due to absorption. In contrast to synchrotron facilities a single-pass FEL can serve only one experiment at a time. The FLASH beam is delivered directly to the beamlines

BL1, BL2 and BL3. BL3, the beamline utilised in Chapter 3, provides users with an unfocused FEL beam in order to allow installation of experiment-specific focusing optics by retracting the toroidal focusing mirror upstream. BL1 and BL2 provide users with a focused FEL of spot size 100 μm and 20 μm respectively. Due to the inherent bandwidth of the FEL radiation, beamlines PG1 and PG2 were installed with a high-resolution monochromator to produce EUV radiation of yet narrower bandwidth.

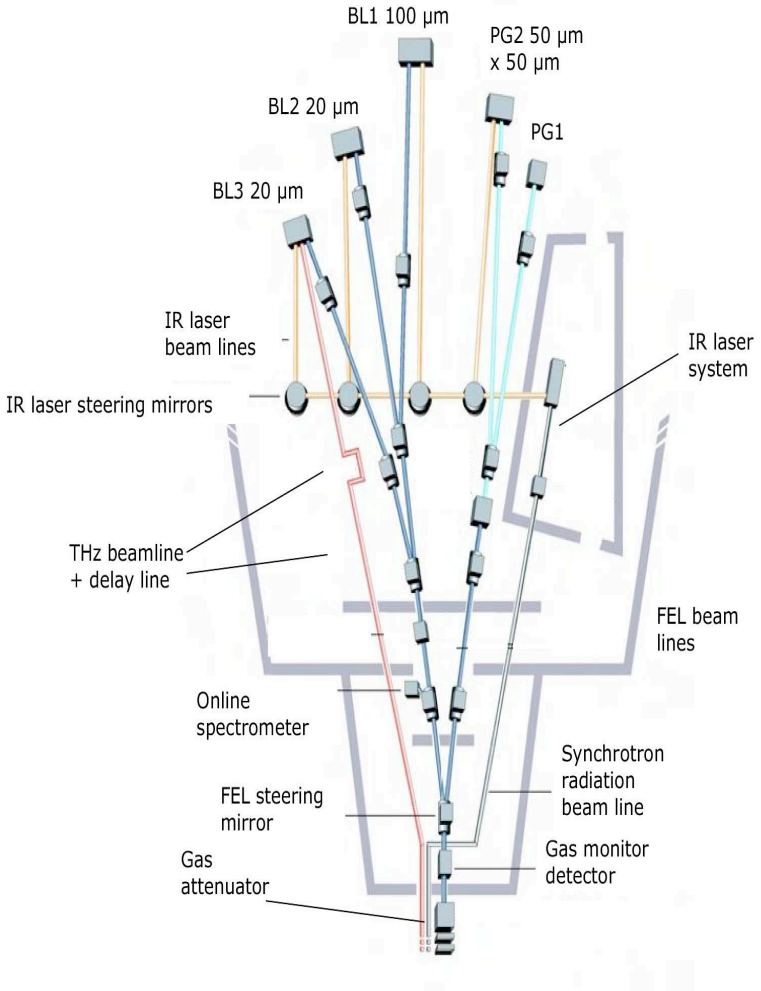

Figure 2.1: Schematic layout of the FLASH experimental hall. The five beamlines are designated as follows: FEL beam in dark blue, IR laser in orange, monochromatized FEL beam in light blue, and THz radiation in red[28].

2.1.1 Gas Monitor Detector

Before being separated into individual beamlines, the FEL radiation is passed through an attenuation system based on gas absorption and a set of four gas-monitor de-

tectors (GMDs) for intensity and beam position determination. In order to monitor the photon flux and pulse energy of the EUV radiation, these GMDs were developed [101] as tools to provide shot-to-shot measurements of the pulse energy, and can be used to obtain the absolute number of photons per pulse. The detector uses the photoionization of a low density rare gas (Xe) and provides a measure of the FEL pulse energy of up to 1 mJ covering a dynamic range of seven orders of magnitude. They are radiation transparent due to the very low particle density. Electrons and ions created upon photoionization are extracted and accelerated in opposite directions by a homogeneous electric field. Faraday cups are used to detect the large number (10^6 - 10^9) of charged particles created in a single FEL pulse (shown in Fig. 2.2). It was an essential tool for analysing the electron yield as a function of pulse intensity, a technique that will be discussed later. The average pulse energy for the experiments carried out to date was about 40 μJ but it fluctuated from about 5 μJ to 100 μJ thereby allowing us to build intensity dependent plots of the electron yield by referencing single shot data to the GMD.

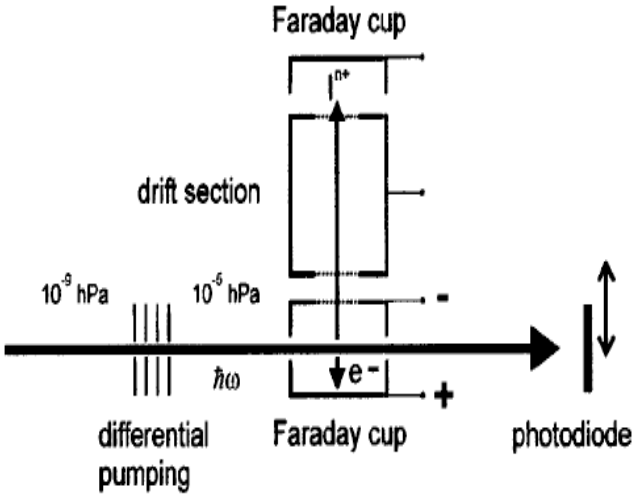

Figure 2.2: Schematic diagram of the gas-monitor detector [102].

2.2 Experimental Setup for One Colour Spectroscopy

Fig. 2.3 and Fig. 2.4 illustrate the salient features of the setup. The main features are the multilayer mirror, which is positioned so that the divergent FEL beam is brought to a focus at the entrance aperture of the TOF. It is moved by means of a 3-axis translation stage. The spot size (specifically, the diameter) at the focus of the mirror was estimated from the target depletion effect [103] to be close to 5 μm . A

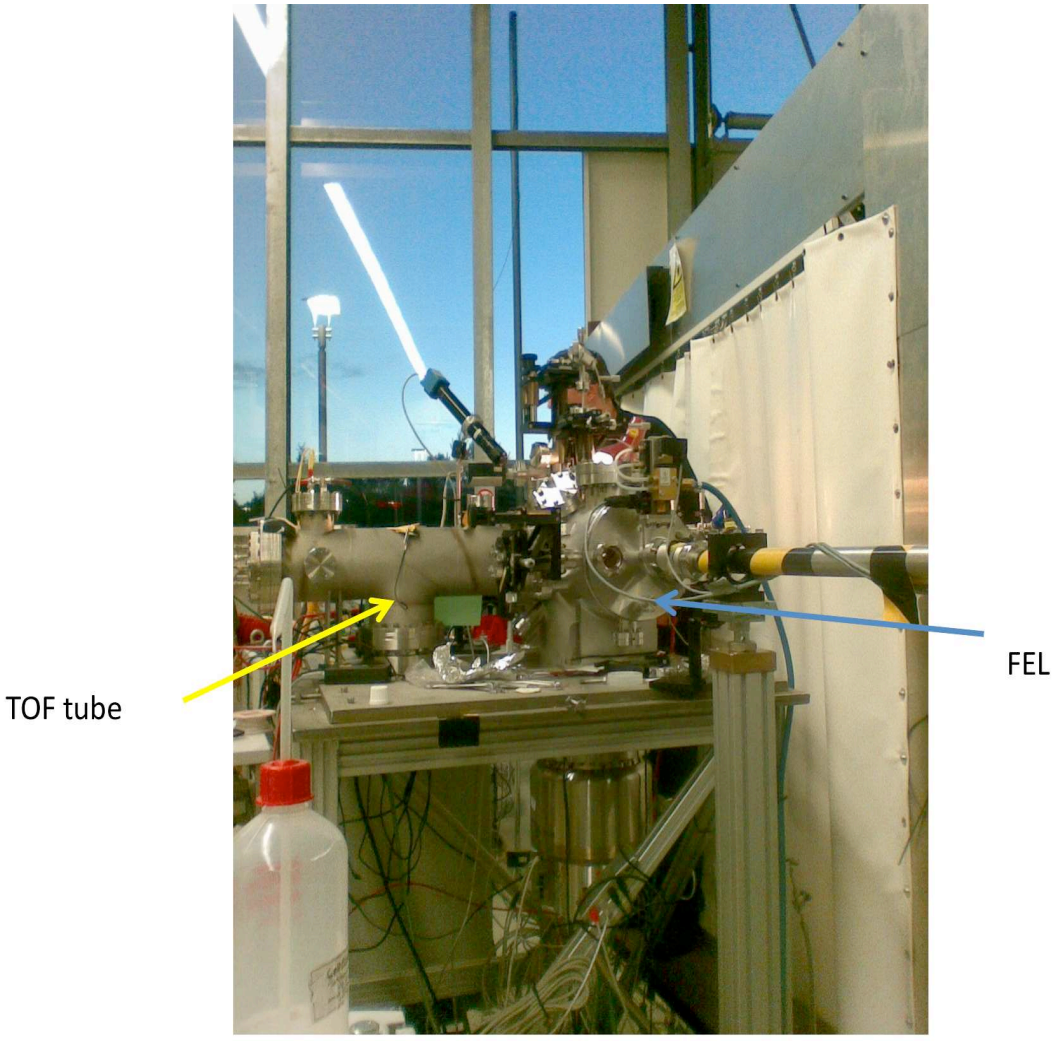

Figure 2.3: A photograph taken at a recent experiment. The incoming FEL path is shown, along with the relative orientation of the spectrometer.

magnetic bottle type electron spectrometer was positioned on the electro-optic axis such that the magnet pushed electrons from the interaction region into the time-of-flight spectrometer. Typical base pressures were on the order of 10^{-8} mbar, with rare gas pressures generally around 10^{-5}-10^{-6} mbar used in experiments. A beam block in front of the mirror enabled us to determine the signal produced by the unfocussed incoming beam (diameter of about 10 mm). Using this background signal, appropriately weighted, we were able to extract the electron spectrum corresponding to the strongly focused FEL beam only. This is done to ensure that the detected signal is not due to the second harmonic of the FEL, as the mirror does not reflect it.

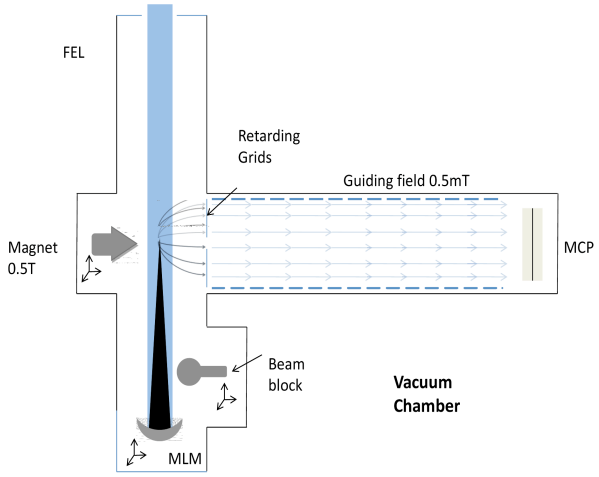

Figure 2.4: Experimental setup: The main component of the system is a magnetic bottle-type electron spectrometer. Focusing of the FEL beam was achieved by a spherical multilayer mirror. Spectra were taken with the unfocused and the unfocused plus focused FEL beam in the chamber by using a beam block in front of the mirror (see text for details).

2.2.1 The Magnetic Bottle Electron Spectrometer

A magnetic bottle electron spectrometer (MBES) [104, 105] was used to measure the kinetic energy of electrons produced in the photoionization of rare gas atoms by the EUV FEL beam. The main components of the electron spectrometer are the extraction region, the field-free drift tube and the MCP electron detector. Electrons produced by photoionization in the interaction region were directed towards the entrance slit of the 0.65 m long flight tube by a strong permanent magnet (0.5 T). The permanent magnetic field collects emitted electrons, driving them towards the entrance aperture of the spectrometer. By the time the electrons reach the retardation grids their paths are almost parallel. The magnetic field results in detection

of electrons emitted in almost any direction in the interaction region i.e. it can provide a single shot spectrum due to its high collection efficiency over a 4π solid angle [106]. However, this very useful feature comes at the expense of angular resolution. A solenoid producing a weak guiding field (0.5 mT) causes the electrons to undergo a spiral path to the micro-channel plate (MCP) detector. A time-of-flight (TOF) detection scheme allows the kinetic energies of all the photoelectrons to be measured from a single oscilloscope trace. Single shot or averaged TOF spectra were recorded with the aid of a fast digital oscilloscope (LeCroy Wavemaster 8600A). The energy resolution in the electron spectra was mainly determined by the bandwidth of the FEL (0.5% 1%) and the MBES (at best 5% of the electron kinetic energies). A typical photoelectron spectrum is displayed in Fig. 2.5.

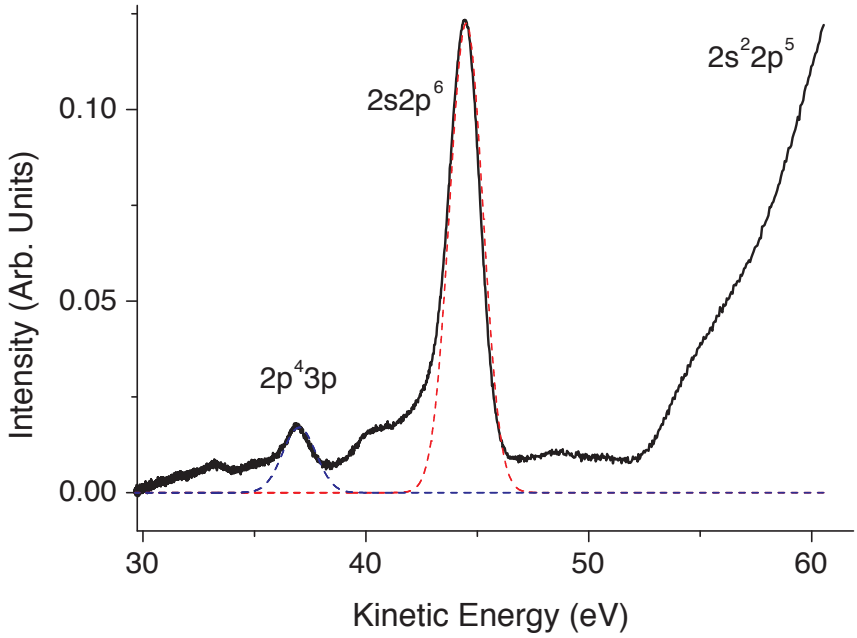

Figure 2.5: Electron spectrum produced by the interaction of FLASH operating at the photon energy of (93 $\pm$ 1) eV with a Ne gas target. The peak labels indicate the configuration of the Ne^+ ion after ionization i.e. $2s2p^6$ refers to direct emission of a 2s electron.

2.2.1.1 Resolution Limitations

The TOF spectrum shows very narrow lines at short flight times (high kinetic energies) and broad lines at long flight times (small kinetic energies), but when converting the spectra on the kinetic energy scale the opposite is the case, since the resolution is a constant percentage of the kinetic energy (5% in this case). This

results in the fast high energy peaks becoming broad and the low kinetic energy peaks appearing quite narrow. One can see in Fig. 2.5 how broad the fast $2p^{-1}$ line is in comparison to the slower $2s^{-1}$ and satellite lines. It is for this reason that a retardation field is applied in front of the entrance aperture of the spectrometer. The aim is to minimise the velocity of the electrons in the drift tube whose energy we wish to measure. This serves two purposes; firstly as mentioned earlier, our resolution is best for slow electrons. Secondly, as the MCP signal is sampled by the storage oscilloscope at fixed time intervals, slow electron spectra consist of more data points, thereby increasing resolving power further.

2.2.2 Multilayer Mirrors

Extreme ultraviolet radiation is characterized by the high absorption at normal and low angle incidence it experiences when incident on most materials. This, understandably, has made the development of high reflectance multilayer mirrors that can operate at normal incidence angles entirely non-trivial [107]. Developments in advanced deposition techniques, such as DC Magnetron Sputtering, have resulted in multilayer interference coatings, or simply, multilayer mirrors, that possess high reflectance (on the order of 70%) at normal and near-normal angles of incidence in the spectral range of 10-15nm for both flat and curved substrates [108, 109].

Briefly, multilayer optics work on the principle of interference of reflected waves. The mirrors utilised in this thesis were constructed of alternating layers of materials with differnt refractive indices, in this case silicon and molybdenum, with a periodicity of $\lambda/2$. The spectral bandpass of the mirror is inversely proportional to the number of layers, N. Incident radiation is partially reflected at each layer and constructive interference occurs causing those partial waves that are in phase to add coherently. This is accomplished when the Bragg equation is satisfied, i.e. $n\lambda = 2.d.\sin\alpha$, where n is the Bragg order, α is the angle of incidence, d is the period i.e. period thickness (combination of two layers) and λ has the usually meaning. By keeping the period constant but minimising the thickness of the material with the highest absorbance, the reflectivity of the structure is maximised.

Shown in Fig. 2.6 and Fig. 2.7 is the measured reflectivity as a function of incident photon energy. Both mirrors were deposited on a curved substrate with a radius of curvature (ROC) of 400 mm, providing a focal length of 200 mm. The mirror optimised for normal incidence at 93 eV photon energy consists of 40 layers, resulting in a bandwidth of approximately 5% or approximately 5 eV. The mirror reflectivity is an impressive 68%, which taking into account the diffusion between layers, is possibly the maximum available. It produces a focal spot of 3 μm, which for an FEL pulse of 10 fs duration carrying an energy of 10 μJ provides intensities

in the region of 10^{16} Wcm^{-2}.

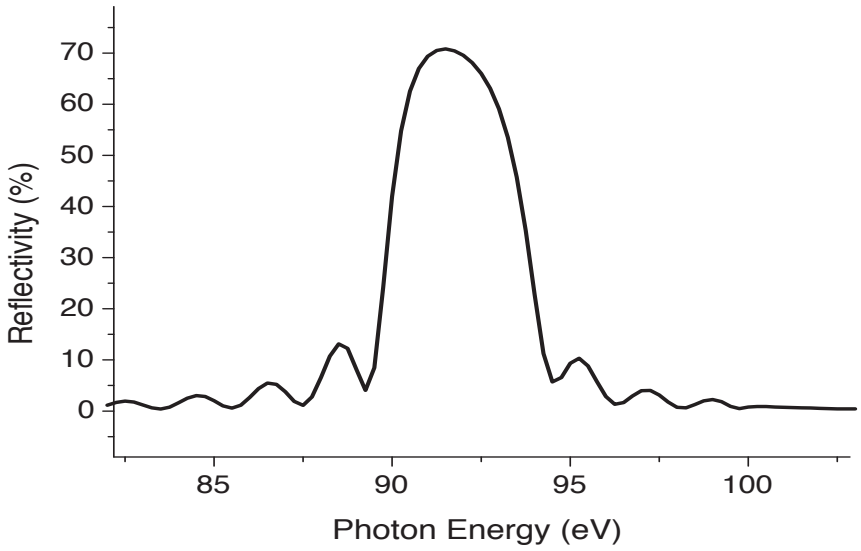

Figure 2.6: Computed reflectivity as a function of incident photon energy for a molybdenum-silicon (Mo/Si) mirror at normal incidence. The mirror consists of approximately 40 layer pairs with a thickess of 6.7 nm. Peak reflectivity approaches 68% at 93 eV. Computed using the online application at [110].

The 46 eV mirror is coated in order to optimise reflectance at an incidence angle of 3°. However, it can be used at any angle between 0° and 5° without any significant losses (due to larger spot size diameter). The off-axis configuration ensures that the interaction regions of the unfocused and focused beams are spatially separated. This solved the problem inherent in normal incidence back reflecting mirrors i.e. the focused beam interacts with a target that has potentially been ionized by the incident, unfocused beam. As a result of the relatively low amount of layer pairs (N=20), it has a modest bandwidth of around 5 eV, while its reflectivity is on the order of 30%. It can yield an intensity in the focal region on the order of 5×10^{14} Wcm^{-2}.

A drawback with this mirror is the high reflectivity at around 92 eV, the second harmonic of 46 eV. However, in our experiments, no strong signal resulting from the second harmonic was detected.

2.3 Experimental Setup for Two Colour Ionization Studies

Users at FLASH can avail of an ultrafast optical laser system via a dedicated optical beamline based on a Ti:Sapphire laser generating intense 800 nm IR radiation. The

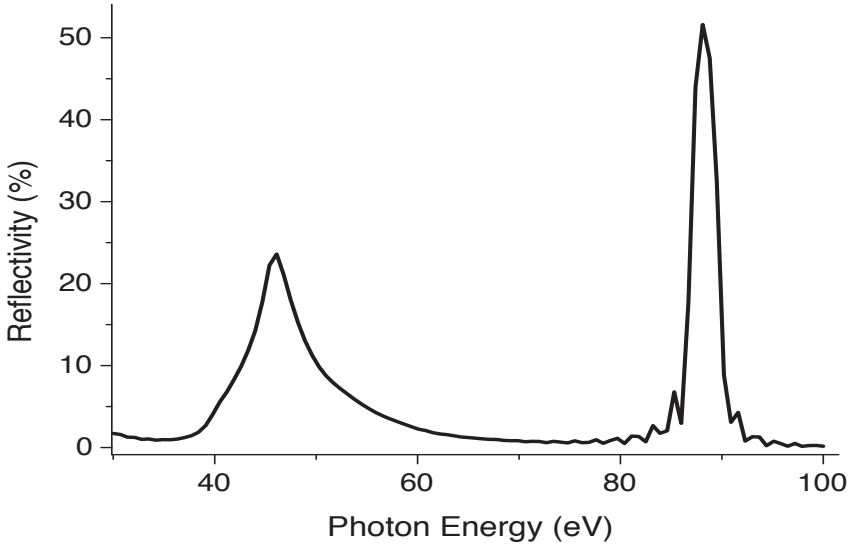

Figure 2.7: The theoretical reflectivity of the 46 eV mirror is shown here as a function of photon energy. It consists of 20 bilayers, so bandwidth is higher than that of the 93 eV mirror. The mirror was able to achieve a focal spot size on the order of 5 μm [111].

pulse length can be varied on request, from 120 fs $\rightarrow$ 3 ps. The delivery of the IR pulses to the experimental end-stations is synchronised with the FEL pulses. The alterations to the experimental setup are illustrated in Fig. 2.8

2.3.1 Spatial Overlap of EUV and IR Laser Pulses

The strength of any two colour excitation signal is critically dependent on the degree of spatial overlap of the EUV and optical laser beams. Spot sizes of the FEL and IR beams at the entrance to the spectrometer were approximately 30 μm and 50 μm, respectively. Utilising a custom made phosphor screen (15 μm layer of $Y_3Al_50_{12}$: Ce, 2.8 μm grain diameter), the foci of the beams were imaged and aligned. Light from the FEL caused causes the phosphor to fluoresce (FEL photons are absorbed, and re-emitted at longer wavelengths, in this case bright green coloured), whilst light from the Ti:Sapphire source is scattered by the relatively large grains (relative compared to the wavelength of the IR light). Both the scattered and fluorescent light are visible on a CCD camera, enabling spatial profiling.

Spatial alignment is achieved primarily by moving the focus of the IR beam relative to the FEL beam, as movement of the FEL focus is not recommended during beamtime. The IR beam is moveable in three dimensions; two lateral (in the plane of the focus), and one longitudinal (along the direction of the beams). Movement

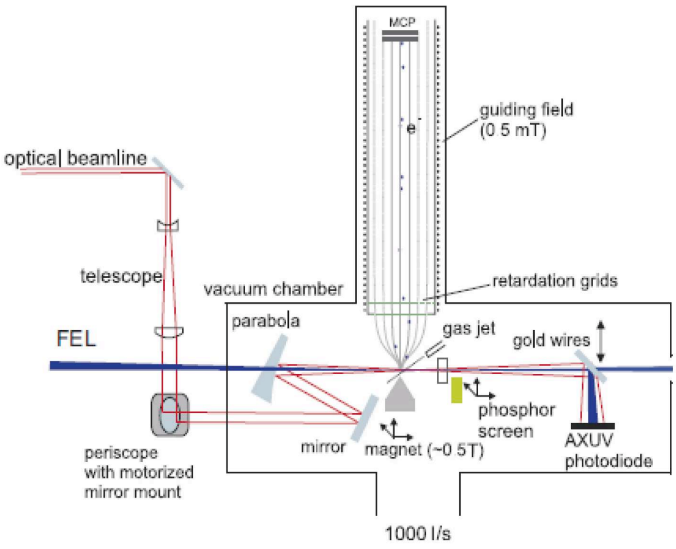

Figure 2.8: Experimental set-up for the pump-probe experiments using the combination of the FEL with an optical laser [100].

transverse to the direction of the FEL is made possible with the use of a stepper motor to control the orientation of a parabolic mirror located outside the vacuum chamber. Movement along the direction of propagation was achieved by varying the divergence of the beam using a 1:1.5 Galilean telescopic system (f_1 = - 200 mm, f_2 = 300 mm). By changing the distance between the two lenses, the divergence is altered, hence shifting the focal position. Movement of $\pm$1 mm in the longitudinal direction was achievable.

2.3.2 Temporal Overlap

Somewhat more difficult to achieve than spatial overlap, temporal synchronisation of the two independently generated pulses is achieved by varying the time delay between the arrival of successive FEL and IR pulses. The principal method of controlling the relative delay is through use of a variable optical delay stage located outside the chamber in the laser hutch some 20 m from the experimental chamber. With this setup, the arrival time of the IR pulses can be varied over a period of up to 1000 ps, with a resolution of a few femtoseconds. Two methods are used consecutively to achieve a zero time delay i.e. perfect temporal synchronisation.

A coarse overlap (within tens of picoseconds) was initially achieved using a

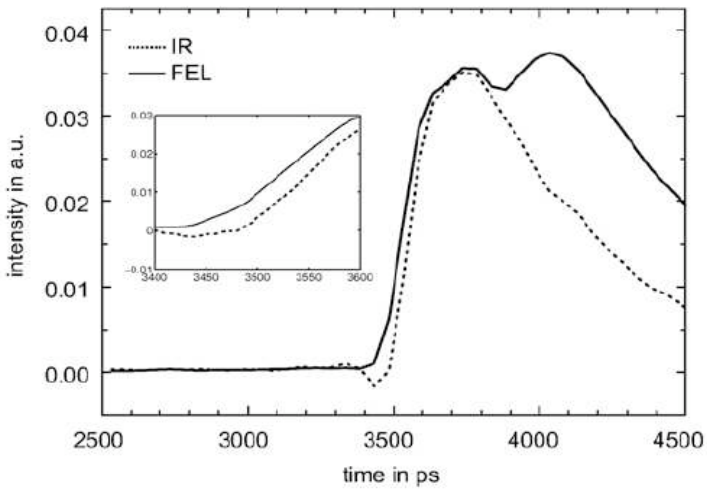

Figure 2.9: A typical set of traces obtained from the fast photodiode setup. The inset shows the negative slope of the IR response corresponding to the rise in signal from the FEL [100].

radiation hardened photodiode (Model: AXUV-HS3), sensitive to both EUV and IR radiation. For this purpose, a custom built, self contained electronic circuit was built by Dr. John Dardis [112], containing the diode and appropriate bias, with the capability to output the resultant photodiode traces to the digital scope (LeCroy Wavemaster 8600A). A typical readout is given in Fig. 2.9. Note the inset, showing the negative slope of the IR response corresponding to the rise in signal from the FEL. Further, more accurate temporal synchronisation was performed using a cross correlation technique, the so called laser assisted photoelectric effect or LAPE. By plotting the intensity of the first photoelectron sideband as a function of relative delay, one can build up a cross-correlation trace or function. If the temporal profile of both radiation sources is known then the temporal jitter between the two sources can be obtained. The resulting measurement of the time delay is on a time scale comparable to that of the width of the laser pulses [113].

2.4 Summary

In this section, a brief history of free electron lasers has been given, along with specific details on the operation of FLASH, the Free Electron Laser in Hamburg. In addition, the most important components of the two experimental systems utilised in this work have been described in detail, for use in one and two colour photoionization experiments.

Chapter 3

Two Photon ionization of Ne and Xe in the "Extreme Ultraviolet"

3.1 Introduction

An atom subjected to an intense electric field, in the form of a laser, for example, may become ionized. This process can happen via a number of competing pathways. An electron may absorb a single photon of sufficiently high energy and be liberated from the atom in a single step. The kinetic energy of the freed electron is equal to the photon energy minus the binding energy of the electron, as was described by Einstein in his 1905 paper as the photoelectric effect [114]. In this case, the ionization rate is proportional to the intensity of the laser. If an inner shell electron is ionized, an additional electron may be liberated in a process known as Auger decay, in which an inner shell hole is filled by an outer shell electron. The excess energy of the system is then shed via ionization of an additional electron [75]. With the development of sufficiently intense lasers, ionization of an atom by more than one photon became feasible, as demonstrated first in [115] and [116].

It was soon discovered that the signal arising from multiphoton ionization (MPI) scaled as I^N, where N is the number of photons required to ionize the atom. In effect, one could confirm an MPI pathway by measuring the signal as a function of laser intensity. A log-log plot of ion yield against laser intensity (in Wcm^{-2}) would produce a straight line graph with slope of N, where N represents the order of the process [117].

Alongside ongoing experimental work, advances in theoretical work resulted in a framework from which experimental results could be interpreted. The first papers to build on the work of Goeppert-Mayer [93] and Zernik [118, 119] on two photon absorption to provide a theory of N-photon transitions initially dealt with

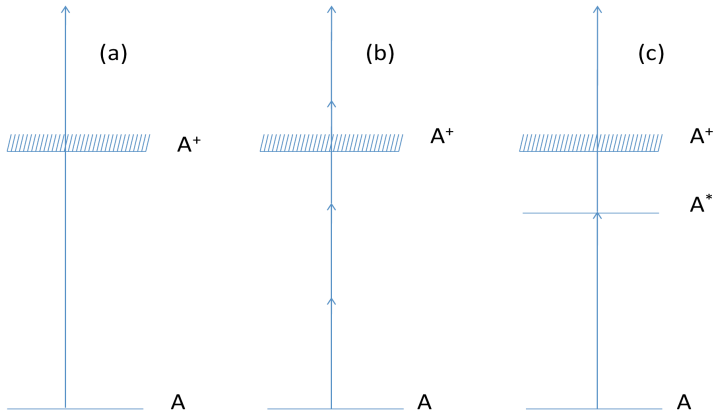

Figure 3.1: Schematic energy level diagram of element 'A', illustrating some of the terms used throughout this chapter (a) single photon ionization, (b) multiphoton ionizations and (c) resonantly enhanced multiphoton ionization. Note that the excited intermediate state that facilitates the resonance may not necessarily lie below the first ionization threshold.

hydrogen and rare gas atoms [95] and also alkali atoms [94]. Fine structure phenomena were incorporated into the framework by P. Lambropoulos [120] to take into account spin-orbit level splitting of the target atom. The dependence of the ionization yield on the temporal coherence of the laser pulse was investigated initially in [121]. A comprehensive review [122] summarised developments in the field up to the mid 1970s.

In the early 1980s it was discovered that the multiphoton ionization rate could be greatly enhanced if a transition (involving one or more photons) promoted an electron to an unoccupied bound state. This pathway is referred to as resonantly enhanced multiphoton ionization (REMPI) [123], and is illustrated schematically in Fig. 3.1(c). MPI using picosecond laser pulses was studied in [124], in which no enhancement due to intermediate resonances was apparent due to the short temporal nature of the laser pulses (the resultant increase in intensity ponderomotively shifted the intermediate levels out of resonance). Absolute multiphoton cross sections of Kr and Xe were obtained in [125] (see Fig. 3.2) These data were obtained with the aid of a UV (λ = 293 nm) laser operating at the then unprecedented UV intensity of 10^{13} Wcm^{-2}. The cross sections obtained were found to be in good agreement with theoretical estimates.

Another aspect of multiphoton ionization that was under investigation in the early eighties was the process of above-threshold ionization (ATI). First described theoretically by Gontier *et al* [126], this MPI event involves free electrons in the continuum (above-threshold) undergoing stimulated emission or absorption of ad-

ditional photons. These types of transitions are also referred to as 'continuum - continuum' transitions [127]. These transitions manifest themselves in the photoelectron spectra as extra peaks separated in energy by an amount equal to the photon energy of the ionizing laser field. The first experimental evidence was published by the group of Agostini *et al* [128]. The original spectrum showing the ATI peaks is displayed in Fig. 3.3

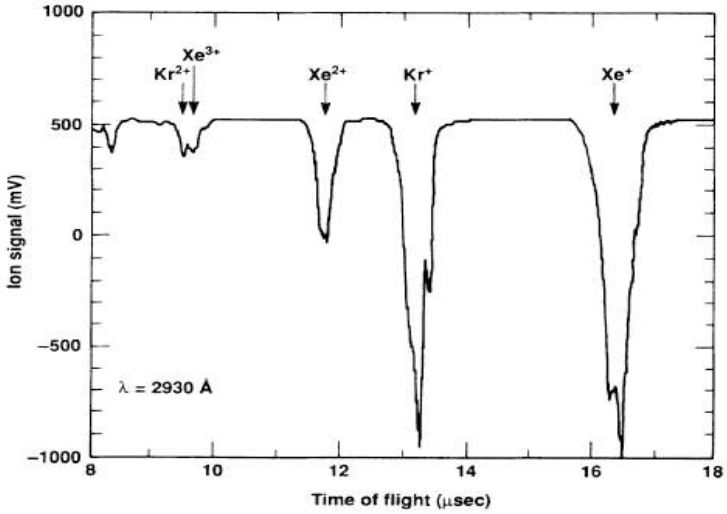

Figure 3.2: A resonantly enhanced time-of-flight spectrum in which ion states of xenon and krypton are separated by their mass/charge ratio. Obtained using 293nm laser light at intensites on the order of 10^{13}Wcm^{-2}[125].

An interesting debate started in the mid 1980s centred on the results of Luk *et al* [129]. The observation of very high charge states (U^{10+}), suggested as the result of multiphoton absorption (99 photons), initially raised some doubts regarding the validity of the prevailing perturbative approach to MPI (that is, the unperturbed Hamiltonian for a single bound electron in a single oscillating electric field is modified to take into account an electric field operator containing multiphoton absorption terms). It was postulated in [130, 131] that the collective excitation of an entire valence electron shell could in principle transfer large amounts of energy to inner shells, facilitating unprecedented levels of photon absorption. This non-linear approach, in which, at suitably high laser intensities, coherent multi-electron oscillations become the dominant absorption mechanism, seemed to adequately describe the experimental results. However, it was shown soon after that no valence shell electrons would ever experience the order of laser intensity required to induce collective effects, as the outer shell would be sequentially stripped of electrons as it experienced the rising edge of an intense laser pulse. The seemingly unusually high degree of ionization could in fact be attributed to sequential, one electron ion-

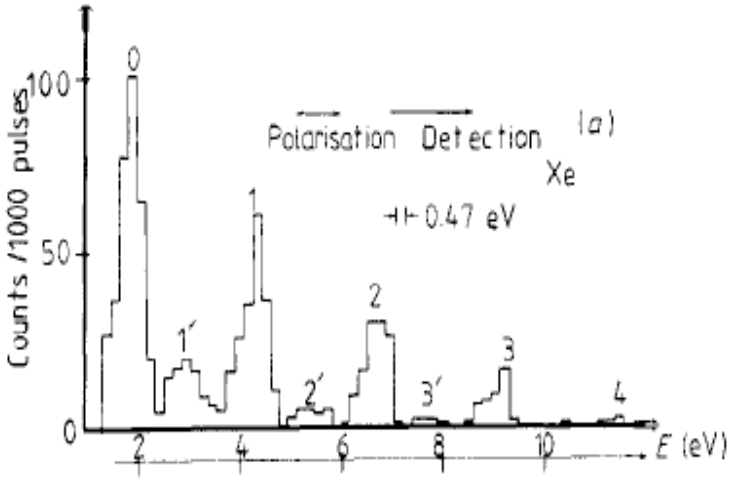

Figure 3.3: Photoelectron spectrum of Xe using a 2.34eV, 200mJ Nd:YAG laser system illustrating above ATI / continuum - continuum transitons. The 1′, 2′ notation indicates ATI originating from the $^2P_{1/2}$ core configuration [128] i.e. Xe + n$h\nu \rightarrow Xe^+$ ($5p^5\ ^2P_{1/2}$ + e^- (1′, 2′, ...))

ization as summarised in [132], in which high order multiphoton ionization rates and relative ionic populations through the laser pulse were derived. The idea of multielectron excitation was soon revisited by the group of DiMauro *et al* [133], in an experiment in which multiphoton single and double ionization of Ca was investigated. It was found that ionization via a correlated, doubly excited bound state was a dominant pathway. The role of these doubly excited states was investigated in [134], and in the early and mid 1990s the first observation of non-sequential double ionization was made [135]. Using ultrafast laser pulses (120 fs) in the optical wavelength regime ensured that tunnel ionization, as opposed to 'conventional' multiphoton ionization, was the dominant double ionization (DI) mechanism. This mechanism was subsequently investigated with improved intensity resolution in [136] in order to determine better the ion-yields. The exact nature of the double ionization mechanism was not clearly understood until relatively recently. Several 'mechanisms' were proposed, including sequential ionization, in which each of the two electrons are emitted independently by two separate absorption events, and sequential ionization involving only one photon, in which the freed first electron knocks out a second via a collision. Strong experimental evidence for a 'rescattering' model, in which the liberated electron is driven back into the target by the laser field causing the ejection of a second electron, was published by the groups of Fittinghoff *et al* [137], Corkum [138] and Dietrich *et al* [139]. The development of Cold Target Recoil Ion Momentum Spectroscopy (COLTRIMS) enabled kinematically complete experiments to be carried out, in which more than one electron

emerging from a multiple ionization event could be observed simultaneously [140].

3.2 Two-Photon Inner-Shell Ionization of Xe in the Extreme-Ultraviolet

It should be noted that, some years ago, high order harmonic sources developed to the point where they could attain the threshold intensities to drive two photon processes in an atom. The very first results were reported in breakthrough experiments at the very limit of intensities that can be obtained with high order harmonic sources, These included two photon single [141] and double [142] ionization of He and single ionization of the valence shells of Ar and Xe [143]. However these studies still only concerned valence electrons. In contrast FLASH provides a monochromatic (bandwidth $< 1\%$), wavelength tunable light source, with focussed intensities which can approach 10^{16} W.cm^{-2} and so has provided the platform for a dramatic expansion of the range of sequential and simultaneous multiphoton ionization experiments that could be both planned and performed at EUV wavelengths. One such study, in which interesting insights into dynamics of two photon double ionization was investigated using a COLTRIMS system, was reported in [144]. The fundamental nature of this three body problem has attracted significant theoretical interest, and the reader is directed to [145], in which a time-dependent solution to the Schrodinger equation for a two-electron system is derived.

Hence, the advent of high-intensity extreme ultraviolet (EUV) and X-ray free electron lasers (FELs) subsequently heralded a new era in the study of nonlinear optical processes, in which the applied laser field exhibits a high degree of coherence in addition to an unprecedented combination of high average and peak intensity at high photon energy. As a result, inner-shell electrons can become important mediators of the multiphoton-matter interaction.

Yet another interesting example of a non-linear process is summarised briefly here. At intensities in excess of 10^{15} Wcm^{-2}, nearly 50 photons of 90eV photon energy interact within 10 to 20 femtoseconds with a single xenon atom and lead to the emission of up to 21 electrons. Neon, argon, and krypton do not show this high degree of photoionization under the same experimental conditions [146]. If these interesting results are due, even in part, to the 4d-ϵf giant continuum resonance, it raises the question whether the resonance also contributes to multiphoton excitation from the inner 4d shell.

This resonance is, in comparison to the other rare gases, a particular feature of Xe in the EUV and arises in the photon energy range from about 85 to 115 eV [43]. For many years, it has represented a prime example of the impact of electron cor-

relation on inner-shell photoionization at low irradiance [147, 86]. The correlations may be described by a collective motion of the ten 4d electrons, driven by the oscillation field of the electromagnetic wave, which results in the emission of one of their members. The effective radial potential for the emitted ϵf electron shows a bi-well structure [148]. The potential barrier between the inner and the outer region of the atom explains the delayed onset of the 4d one-photon ionization leading to the strong and broad one-photon 4d-ϵf resonance feature, known as the giant resonance. In the case of Xe, it is centred 30 eV above the 4d ionization threshold and dominates most of the 4d oscillator strength [See Chapter 1.2.5 1.2.6]

The proposal that the strength and nature of this resonance may also drive, at high irradiance, simultaneous multiphoton excitation from the inner 4d shell constitutes the core of the matter, so an investigation was initiated an into the underlying processes using electron spectroscopy at FLASH [3].

3.2.1 Experimental Setup

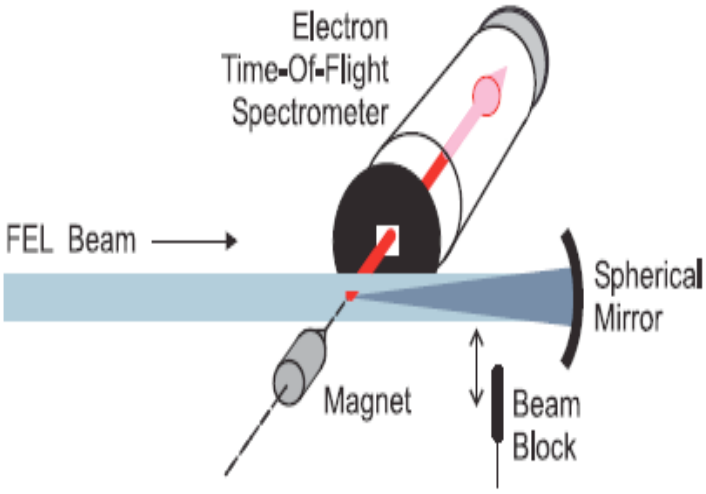

Figure 3.4: Experimental setup: a magnetic bottle type electron spectrometer was used for the electron analysis. Focusing of the FEL beam was achieved by a spherical multilayer mirror. Spectra were taken with the unfocused and the unfocused plus focused FEL beam in the chamber by using a beam block in front of the mirror

The setup has been described previously in some detail, so only the most important features are mentioned here. Fig. 3.4 illustrates the salient features of the experimental set-up. It is essentially a combination of set-ups described in [29, 146, 100]. The photon energy of (93 $\pm$ 1) eV was chosen as it permitted us to employ a high-quality spherical Si/Mo multilayer mirror [108], of the type used in EUV-lithography systems, to focus the FEL beam. The characteristics of the mirror have

been described in detail in the preceding chapter. The reflectance of the mirror at the photon energy of 93 eV was of the order of 65% while the focal spot-size diameter was close to 3μm. The pulse energy was measured on a shot-to-shot basis using a gas-monitor detector (GMD) [102, 101]. In the focus, an irradiance of up to 10^{16} Wcm^{-2} could be achieved. The Xe gas filled the experimental vacuum chamber homogeneously at a pressure of 10^{-6} mbar. The base chamber pressure was 2×10^{-8} mbar. Emitted electrons were analyzed using the magnetic bottle type electron spectrometer [100, 149] (described in Ch.2). A retardation voltage was applied to the entrance aperture to the TOF to prevent electrons with kinetic energies below a given threshold entering the flight tube. A beam block in front of the mirror enabled us to determine the signal produced by the unfocussed incoming beam with a diameter of a few millimetres and to extract in this way the electron spectrum corresponding to the strongly focused FEL beam only.

Since the pulse energy fluctuates from shot to shot, it is necessary to record it for each and every FEL pulse. The device used to do this is called a Gas Monitor Detector or GMD for short. A typical GMD signal is presented in Fig. 3.5. The GMD output is essentially a photoionization signal of xenon. The pulse energy of the FEL pulse is directly proportional to the area under the first peak of the GMD signal, and, at least in the intensity range for this experiment, the response of the gas monitor is linear over our entire range of intensities. That is, a pulse with twice the amount of energy of a subsequent laser pulse will result in a GMD signal for which the area under the first peak is twice as large. This linear response is of course dependent on the detector not being saturated, which occasionally was the case in some of our experimental runs.

As every single photoelectron spectrum is tagged with a corresponding GMD signal, so too is every background. The background in this experiment, that is, the signal produced in the focal region of the mirror *in the absence of gas* is significant. In a workaround to account for this issue, all single-shot spectra were first sorted according to the intensity of the GMD signal. Background spectra measured without Xe in the chamber were also sorted according to FEL intensity. Then corresponding background and Xe electron signal spectra were subtracted. Importantly, they were averaged to minimise error due to fluctuations, with a typical average spectrum containing 100 single shot spectra.

3.2.2 Results

The results presented in this section were taken at a mean FEL pulse energy of approximately 30 μJ, with maximum pulse energies in the region of over 45 μJ, and minimum pulse energies of 10 μJ. These measurements are recorded upstream in

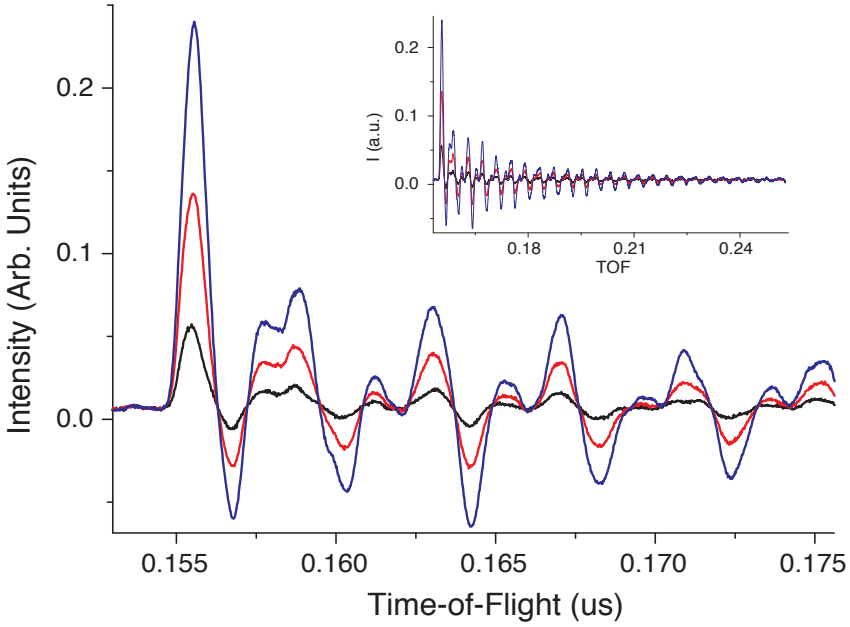

Figure 3.5: Shown here are typical photoion signals from the GMD. The strength of the GMD pulse is directly proportional to the area under the first peak. Inset: The GMD signal in its entirety, exactly as it would appear on a digital readout, such as an oscilloscope. The blue curve was generated by a particularly strong FEL pulse, the black curve by one of the weaker pulses.

one of the beam diagnostic areas. Taking into account the beamline transmission (35%) and the steering mirror reflectivity (56%), the pulse energy in the interaction region is smaller by a factor of approximately 5. An average pulse energy of 45 / 5 = 9 μJ at a pulse length of 10 fs, focused to 3 μm results in a peak intensity of approximately 1×10^{16} Wcm^{-2}.

For the unfocussed beam and/or for low intensities of the FEL beam, one-photon ionization is the dominant process. Part of the corresponding electron spectrum is displayed in Fig. 3.6 showing the 4d photolines at kinetic energies of 25.5 eV and 23.5 eV which correspond to ionization of the $4d_{5/2}$ and $4d_{3/2}$ spin-orbit components, respectively. The corresponding $N_{4,5}O_{2,3}O_{2,3}$ Auger lines appear in the kinetic energy region extending from 30 to 35 eV. The discrete Auger features labelled 1 to 9 in references [150, 151] are blended into two asymmetric features here, centred at 30.7 eV and 33.2 eV, as a result of the resolution limit of the magnetic bottle spectrometer. Additionally, at higher kinetic energies, some broad lines corresponding to the emission of 5p and 5s electrons were observed at about 80 and 70 eV, which are not shown here. This spectrum is included here for illustra-

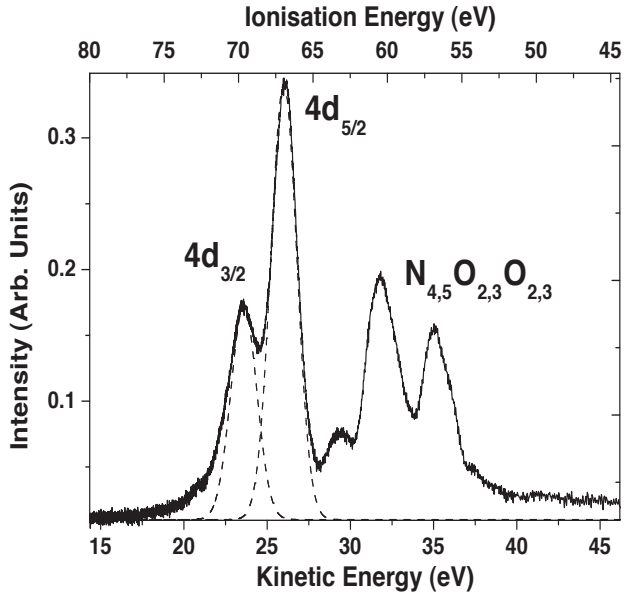

Figure 3.6: Electron spectrum produced by the interaction of FLASH operating at the photon energy of (93 $\pm$ 1) eV with a Xe gas target. The data were obtained at the lowest irradiance used in the experiment, of the order of 10^{10}Wcm^{-2}. The spectrum is dominated by the one-photon 4d ionization and the subsequent $N_{4,5}O_{2,3}O_{2,3}$ Auger decay. The FWHM of the fits is 2.2 eV, which is in part due to the not insignificant bandwidth of the FEL.

tive purposes, as these Auger lines have of course been examined previously in thorough detail. This spectrum confirms the monochromatic properties of the FEL, as the binding energy of the electrons is well known, allowing one to predict accurately and confirm the kinetic energy of the photoelectrons. In addition, the relative line heights are correct, indicating that our MCP intensity calibration is sufficiently adequate (the response is linear across this drift energy region).

The spectrum presented in Fig. 3.6 consists of the average of 100 single shot photoelectron spectra. It is an average of the spectra corresponding to the lowest energy FEL laser pulses in order to maximise the kinetic energy resolution. It was found that for the gas pressure and laser parameters used all but the weakest signals resulted in saturation. This approach maximised the resolving power, otherwise the spin-orbit splitting of the $4d^{-1}$ photoelectron line would not have been resolved. Furthermore, the spectrum presented in Fig. 3.6 indicates that the TOF kinetic energy calibration is quite good.

An additional broad and asymmetric line appears in electron spectra recorded at higher FLASH irradiance, of the order of 10^{16} Wcm^{-2} in the focus, centered at a kinetic energy of about 118 eV as shown in Fig. 3.7. A retarding field of -90V

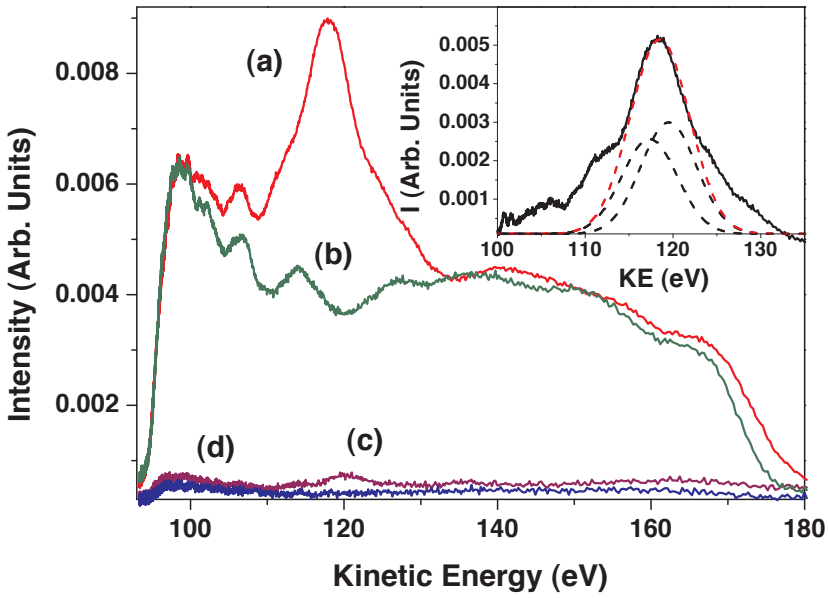

Figure 3.7: Electron spectra recorded at the highest FLASH irradiance of about 10^{16}Wcm^{-2} in the focus. The photon energy was (93 $\pm$ 1) eV. Spectra recorded under different experimental conditions are shown: (a) focused plus unfocussed FEL interacting with Xe, (b) focussed and unfocussed FEL interacting with residual gas, (c) unfocussed FEL interacting with Xe, (d) unfocussed FEL interacting with residual gas. The inset shows the pure Xe spectrum due to the focused FEL, i.e. the difference spectrum (a-b)-(c-d), fitted by the sum of two Gaussians separated by 2 eV.

was applied to the entrance to the time-of-flight tube for this series of spectra, so that photoelectrons produced by one-photon processes were rejected and electron signals obtained were due solely to multiphoton processes. Spectra were recorded with, and without, Xe gas in the chamber to allow the determination of the background contribution from residual gas and scattered light. In addition, the spectra recorded show only a very small contribution from the second harmonic of the FEL radiation when the spherical mirror was blocked. Due to the statistical nature of SASE FELs, the emitted light is expected to contain a finite contribution from odd and even harmonics of the fundamental. The second and third harmonic content has been measured previously [106] for at a photon energy of 38.5 eV, with a contribution on the order of 0.3 - 0.4 % for both second and third. The spectral composition is not expected to be radically different at the photon energies used throughout this work.

3.2.3 Discussion

In order to prove the observation of a multiphoton process, the integrated intensity of the broad line at about 118 eV kinetic energy in Fig. 3.7 was measured as a function of the FEL pulse energy. The result is shown in Fig. 3.8 on a double-logarithmic scale. In fact, the almost quadratic dependence obtained, with a slope of 1.95 $\pm$ 0.12, confirms that the feature at 118 eV arises from a two photon process. In the case of a photoelectron line, the corresponding ionization energy is 2 $\times$ (93 $\pm$ 1) eV - (118 $\pm$ 2) eV = (68 $\pm$ 3) eV which fits well with the 4d ionization energy range of atomic Xe (Fig. 3.6).

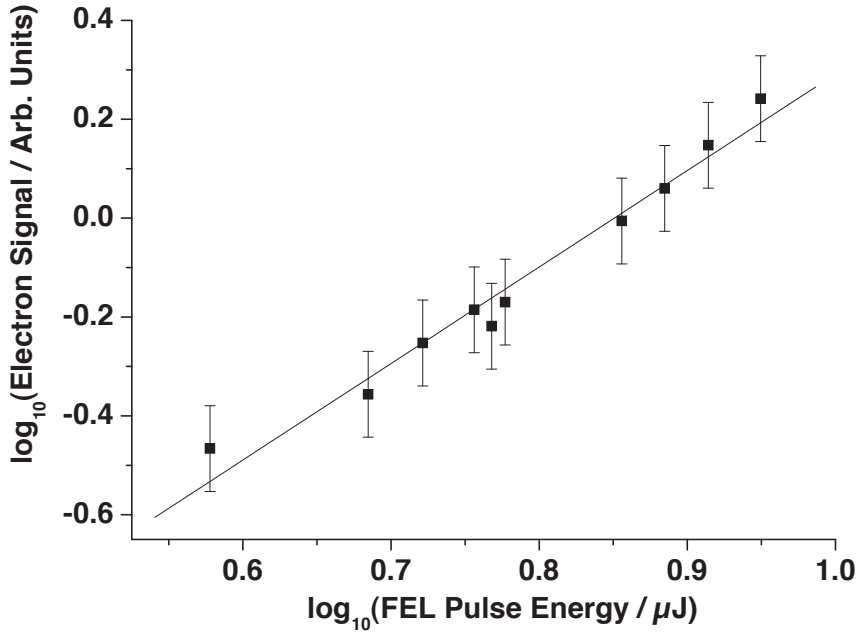

Figure 3.8: Electron yield of the 118 eV feature in Fig. 3.7 as a function of pulse energy. The slope of the linear fit is 1.95 $\pm$ 0.20 and confirms that the feature arises from a two-photon ionization process.

However, from ion spectroscopy results obtained on Xe at 93 eV and irradiance levels beyond 10^{15} Wcm^{-2} [29], one may conclude that the FEL field produces and interacts with a highly ionized target. Hence, photoelectron emission from Xe ions has to be taken into consideration. Xe^+ as a target has four $4d^{-1}$ ionization thresholds at 71.6 eV, 72.9 eV, 74.9 eV, and 76.2 eV [152] which would yield photolines in the kinetic energy range from 110 to 115 eV but Xe^+, in particular, appears only weakly in the ion spectra even at very high FEL intensity as seen in Fig. 3.9 [29].

More highly charged ions appear in much greater numbers but yield electrons

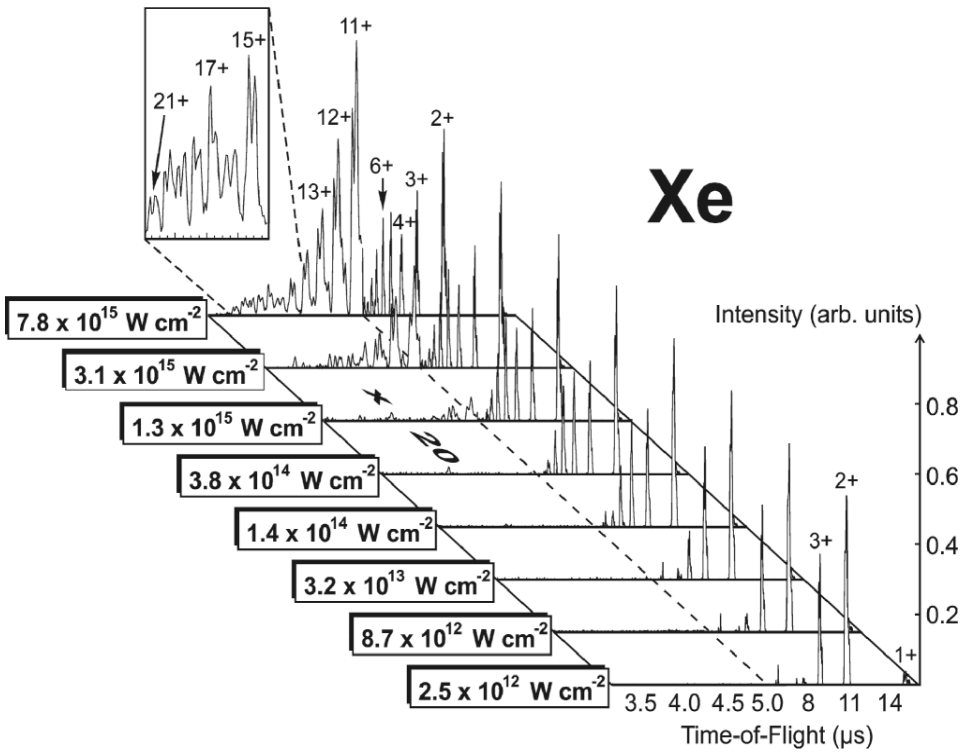

Figure 3.9: Ion TOF mass/charge spectra of xenon taken at a photon energy of 93 eV, displayed here as a function of intensity. The relative abundance of Xe^{2+} and Xe^{3+} compared to Xe^{+} is clear [29].

with kinetic energies below 100 eV due to the increased $4d^{-1}$ ionization energies for doubly and more highly charged Xe ions. O-shell ionization, e.g., $5p^{-1}$ ionization of Xe^{5+} with a ionization energy at 67 eV or $5s^{-1}$ ionization of Xe^{4+} with a ionization energy at 69 eV [68] could produce photoelectrons with relevant kinetic energies but the two-photon cross sections for these sub-shells are expected to be much smaller than for the 4d case, as ionization from these subshells is not resonantly enhanced. In addition, it is noted that, for atomic Xe, there may be a contribution from $4p^{-1}$ Auger processes [153] to the low energy wing of the line in Fig. 3.7 at 118eV. However, we do not have signatures of direct two-photon $4p^{-1}$ ionization, i.e., photoelectrons in the 40 to 45 eV range even at the highest FEL intensities. Thus, one may conclude that the 118eV feature in Fig. 3.7 is mainly due to the two-photon $4d^{-1}$ ionization process which might be resonantly enhanced by the giant resonance of Xe at 93 eV photon energy.

Calculations performed by Hugo van der Hart of Queens University, Belfast, show that at the estimated mean irradiance levels (in the focus) of several about 10^{15} - 10^{16} Wcm^{-2}, the two-photon emission of a 4d electron via an ϵf state accounts for at least 0.5 % of the total photoionization rate. The experimental ratio is,

however, smaller due to our large interaction volume and the considerable detection of one-photon emissions from outside the focus, as in reality, the entrance slit of the spectrometer (on the order of 4 mm long) can't discriminate between those electrons produced at the focus and those outside the focus.

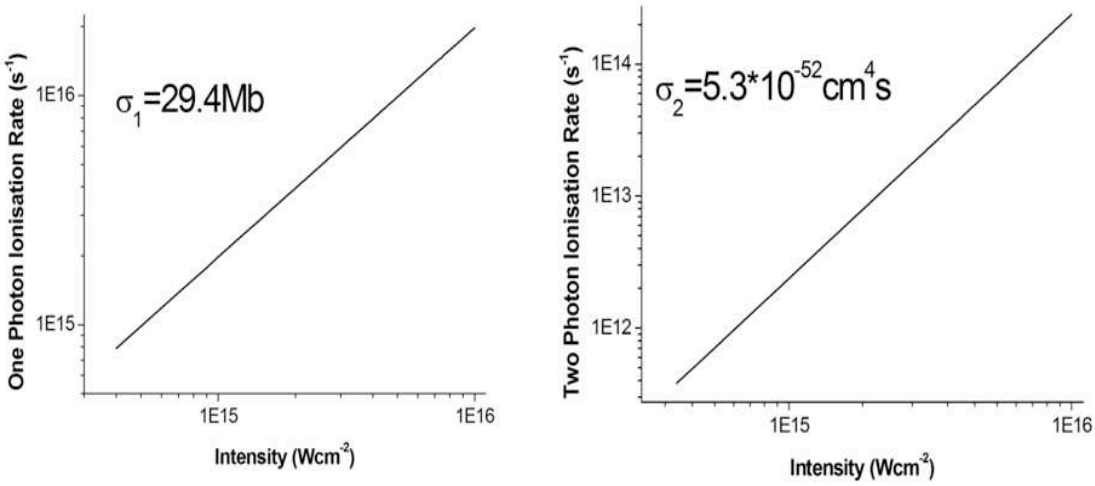

Figure 3.10: One- and Two-photon ionization rates for 4d direct ejection in Xe at a photon energy of 93 eV. Note that the two photon ionization rate is 1% of the one photon rate at 10^{16} Wcm^{-2}. Calculated by H.W. van der Hart.

According to his calculations, the two-photon 4d^{-1} ionization process favors emission of g electrons. Since the absorption of the first photon is theoretically confirmed to be enhanced by the 4d giant resonance, the two-photon 4d^{-1} ionization process proceeds via a sequence of the form: 4d-ϵf-ϵg. Due to the first nd-ϵf step, this scheme represents a resonant process. Due to the continuum character of the intermediate ϵf electron state, it resembles, however, direct rather than sequential two-photon ionization (a sequential scheme would imply two photon absorption via a bound state). The observation of this so-called above threshold ionization (ATI) process, thus, demonstrates that inner-shell ionization may play a role in nonlinear multi-photon processes in the EUV. The large one-photon ionization cross section offered by the 4d-ϵf giant resonance, leads to an enhanced cross section for two-photon ATI. In Fig. 3.10, one and two photon ionization rates have been extracted from the cross sections calculated by Dr. van der Hart. For the peak intensities obtained in the present experiment (10^{16} Wcm^{-2}), one photon ionization of a 4d electron is by far the dominant ionization mechanism. However, it is also apparent that by extrapolation of the curves that the two photon rate will overtake the one photon rate at about 10^{19} Wcm^{-2} to become the main ionization process. To put this figure in perspective, laser light at a photon energy of 100 eV in pulse

energies on the order of 100 μJ, delivered in 1 fs focused to a 1μm diameter spot size will result in intensities over 3×10^{18} Wcm^{-2}.

In conclusion, we have studied the two-photon 4d inner-shell ionization of Xe in a focused EUV beam at FLASH by electron spectroscopy. The corresponding photoelectron line in Fig. 3.7 represents the first detection of an so-called above threshold ionization (ATI) two-photon process in an inner electron shell. This work demonstrates the significance of inner-shells and inner-shell resonances in nonlinear multiphoton-matter interaction for experiments at the new EUV and X-ray laser facilities.

3.3 Two- and Three-Photon Ionization of Neon in the Extreme Ultraviolet

The response of Ne to a strong laser field was also investigated at a photon energy of 93eV. Using photoelectron spectrometry, the simultaneous absorption of two extreme-ultraviolet photons by a valence 2p subshell and the inner 2s subshell electrons of neon has been observed. Evidence for two photon ionization of a 2p electron from Ne^+ was also found, along with signatures from sequential three photon ionization via excited Ne and Ne^+ states.

The interpretation of the data is complicated by the presence of a not insignificant amount of lowly charged ions. The structure at 93 eV above the ground state of Ne is dominated by a series of singly excited $2s^1 2p^5 nl$ states [155]. These states are shown in a highly schematic fashion in Fig. 3.11.

3.3.1 Results

For the unfocussed beam and/or for low intensities of the FEL beam, one-photon ionization is the dominant process. Part of the corresponding electron spectrum is shown in Fig. 3.13 with the 2s and 2p photolines centered at kinetic energies of 43 and 72 eV. The $2p^4 nl$ satellites levels of Ne^+ are visible in the kinetic energy region extending from 30 to 40 eV. The discrete satellite features labelled in reference [155] are blended here as a result of the resolution limit of the magnetic bottle spectrometer. In particular, the features labelled as 9 and 10 are most prominent (See Fig.3.12), appearing as a feature at a kinetic energy of approximately 37 eV. There may be unresolved features in this region due also to sequential ionization of the Ne^+ ion, the lowest threshold of which is 40.9 eV.

The spectrum shown in Fig. 3.13 comprises an average at 100 single shots of the lowest laser pulse intensity in order to minimise the effects of saturation (the 2p

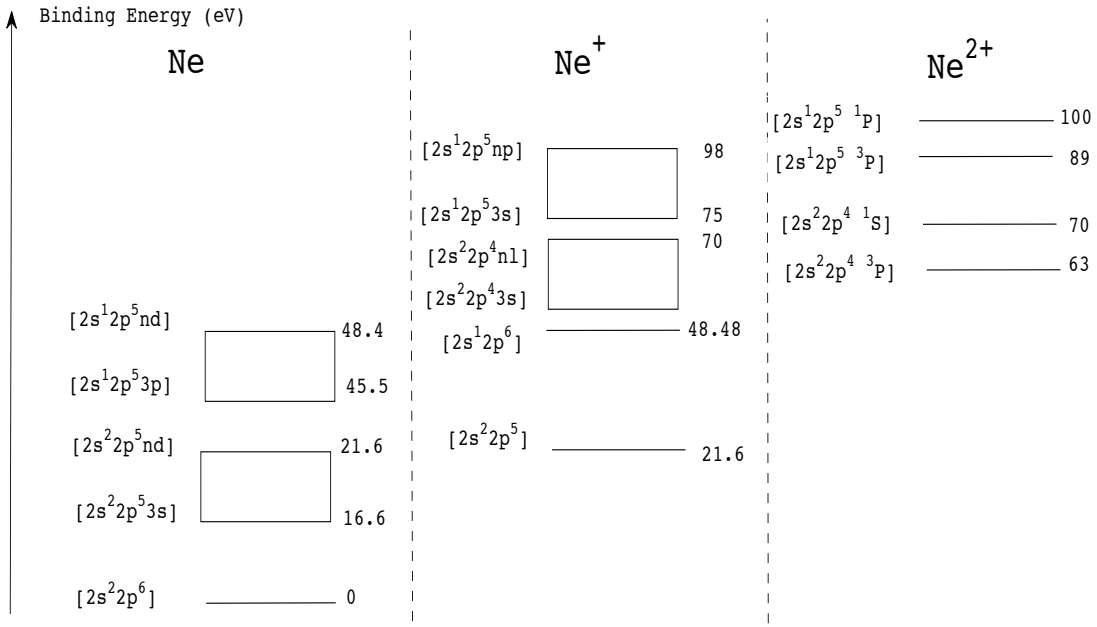

Figure 3.11: Energy level scheme for Ne, Ne^{+} and Ne^{2+}. Data taken from NIST [154].

photoelectron line saturates the detector rapidly) and also to maximise energy resolution. A linewidth of 1.5eV was obtained for the 2s photoelectron line, which is the narrowest obtained for the experimental system. This width is almost certainly the result of the bandwidth of the FEL, as the electron spectrometer has a resolution of 5% of the drift energy of the photoelectrons. A 50 eV photoelectron with a drift energy in the flight tube (after passing the retardation field) of 10 eV should in principle have a linewidth 0.5eV. This spectrum serves to confirm the validity of the TOF calibration, and in addition, the relative intensity of the $2p^4 3p\ ^2P$ and $2s2p^6\ ^2S$ photoelectron lines of 13.8% (13.4% [155]) indicate that the detection efficiency of the MCP is correctly accounted for. The feature lying at 33 eV is probably another satellite, most likely corresponding to the blend of features labelled 19 and 20 in Fig.3.12.

In electron spectra recorded using the focused beam (achieving intensities on the order of 10^{16} Wcm^{-2}), additional broad and asymmetric lines appear as shown in Fig. 3.14. As in [156], we set a high retarding field of -90 V at the entrance to the TOF so that photoelectrons due to one-photon processes were rejected. Hence electron signals obtained are due solely to multiphoton processes. Spectra were recorded with and without Ne gas in the chamber to allow the determination of the background contribution of ionization from residual gas and of scattered light.

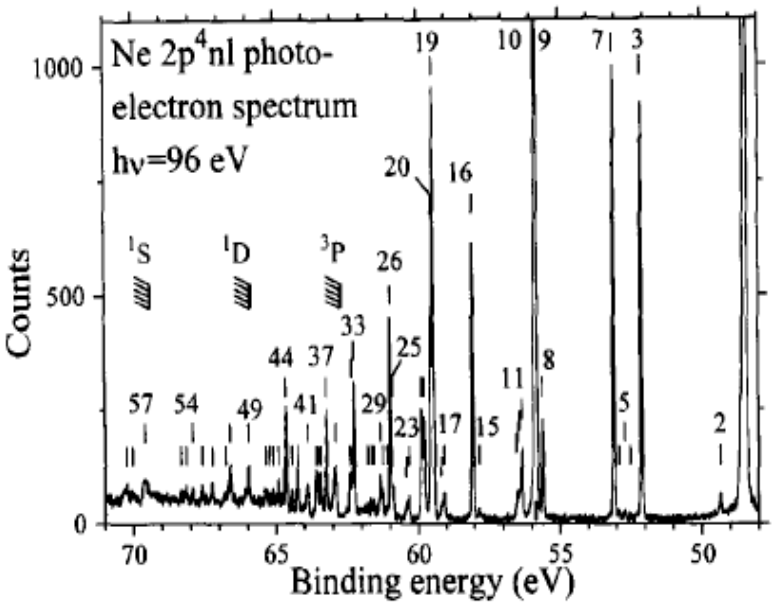

Figure 3.12: The photoelectron spectrum of the Ne $2p^4nl$ satellites, produced by excitation by 96 eV photons [155]. As a guide, the line labelled 19 is 4.4% as intense as the $2s^{-1}$ photoelectron line (off-screen).

In addition, the spectra recorded when the spherical mirror was blocked show only a very small contribution from the second harmonic light of the FEL radiation.

3.3.2 Discussion

The following labels are assigned to the main structures in Fig. 3.14: The broad structure centered at 163 eV is a result of direct two photon ionization of the 2p electron from the Ne atom (labelled 'd' in Fig. 3.14). The energy range for such an event are as follows ($2 \times (93 \pm 1)$ - 21.6 = 164 ± 2). Similarly, the feature lying in the energy range around 140 eV is due to two photon ionization of the inner 2s electron, as given by ($2 \times (93 \pm 1)$ - 48.48 = 138 ± 2). This peak is labelled 'b' in Fig. 3.14. The assignment of the features 'a', 'c' and 'e' are not obvious, so we infer the following based on their relative amplitudes and kinetic energies.

For the remaining peaks, we first of all establish that by using a mirror to achieve especially high irradiance, the laser field of the FEL is now interacting with more complex, ionized target. The following accessible thresholds will ionize Ne^+ leaving it in a Ne^{2+} configuration: 40.96 eV, 41.04 eV and 41.08 eV ($2s^22p^4$ $^3P_{2,1,0}$) respectively, 44.17 eV ($2s^22p^4$ $^1D_2$) and 47.85 eV ($2s^22p^4$ $^1S_0$). Two photon ionization out of Ne^+ yielding these Ne^{2+} configurations would yield a series of photoelectron lines at kinetic energies of 138 eV to 145 eV, resulting in a contribu-

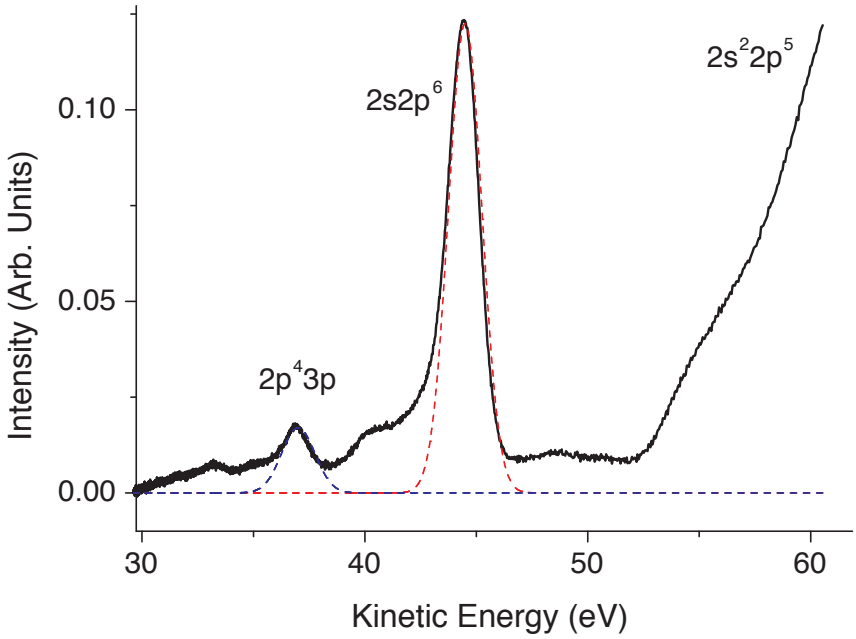

Figure 3.13: Electron spectrum produced by the interaction of FLASH operating at the photon energy of (93 $\pm$ 1) eV with a Ne gas target. The data were obtained at the lowest irradiance used in the experiment, of the order of 10^{10} Wcm^{-2}. The peak labels indicate the configuration of the Ne^+ ion after ionization i.e. $2s2p^6$ refers to direct emission of a 2s electron.

tion to feature 'c'. This is an example of sequential three photon double ionization, where the first photon is used to produce the Ne^+ ground state. Whilst it is feasible that such a mechanism could generate the features at 'b' *and* 'c', this would require the population of Ne^+ in the target to be comparable to that of neutral Ne. The structure below 130 eV ('a') is tentatively assigned as two photon ionization of the excited $2p^4nl$ states of Ne^+, leaving behind a Ne^{2+} state in the ground configuration. Finally, the weak feature labelled 'e' is produced via two photon ionization of an excited Ne^+ $2s^22p^4nl$ state, producing a Ne^{2+} ion in the ground configuration. These ionization mechanisms are illustrated in Fig. 3.15.

It is of course possible that the high kinetic energy photoelectron features present here originate from ionization processes from lowly charged ions. The ionization threshold for a 2s electron in the Ne^+ target is approximately 66.2eV. However, two photon ionization would results in a free electron with an energy of less than 120eV. L-shell ionization from higher charge states i.e. from 2p or 2s subshells in Ne^{2+} might also yield electrons around the 110-120 eV kinetic energy region. With increasing ion stage though, electrons in the L-shell have increasingly higher and

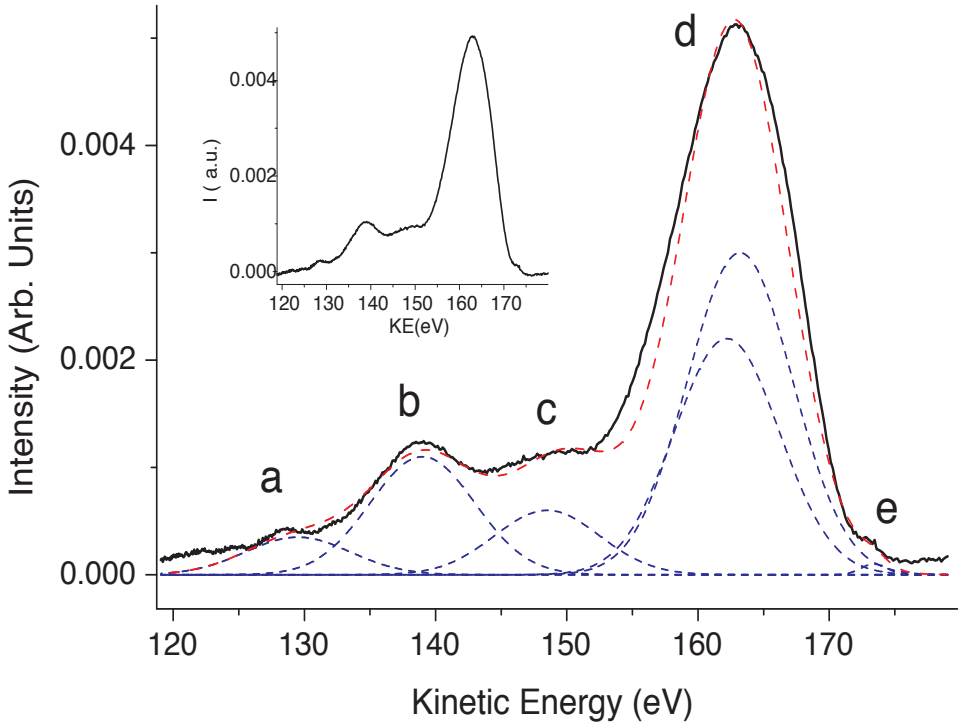

Figure 3.14: Electron spectra recorded at the highest FLASH irradiance of about 10^{16} Wcm^{-2} in the focus. The peaks 'a' to 'e' are explained and discussed in the main text.

higher binding energies, so this alternative pathway is ruled out. The multi-photon nature of the features can be inferred in a semi-quantitative fashion based on theoretical predictions. Examining closely the 2s and 2p photoelectron peaks, it is clear that the ratio of the one and two photon generated features are different. The ratio 2s/2p in the one photon case is the about 10%, as expected from the literature [157]. The two photon ratio differs drastically however, with values 2s/2p = 21% in the experiment compared to a prediction of 42% from theory.. The disparity between theory and experiment is to be somewhat expected given the complexity of the numerical problem, coupled with uncertainty regarding the multimode nature of the laser (N photon ionization is theoretically more efficient by a factor of $N!$ for totally incoherent light source i.e. many modes, than for a single mode, purely coherent laser [127]) and its pulse profile (that is, does the atom experience a laser pulse with a Gaussian-like energy distribution, or can a square pulse approximation be used?). However, the ratio does confirm, at higher photon energies (and indeed, for multiphoton processes) the increased 2s photoionization probability. It is clear from [157] that for increasing photon energies, the 2s partial cross section rapidly

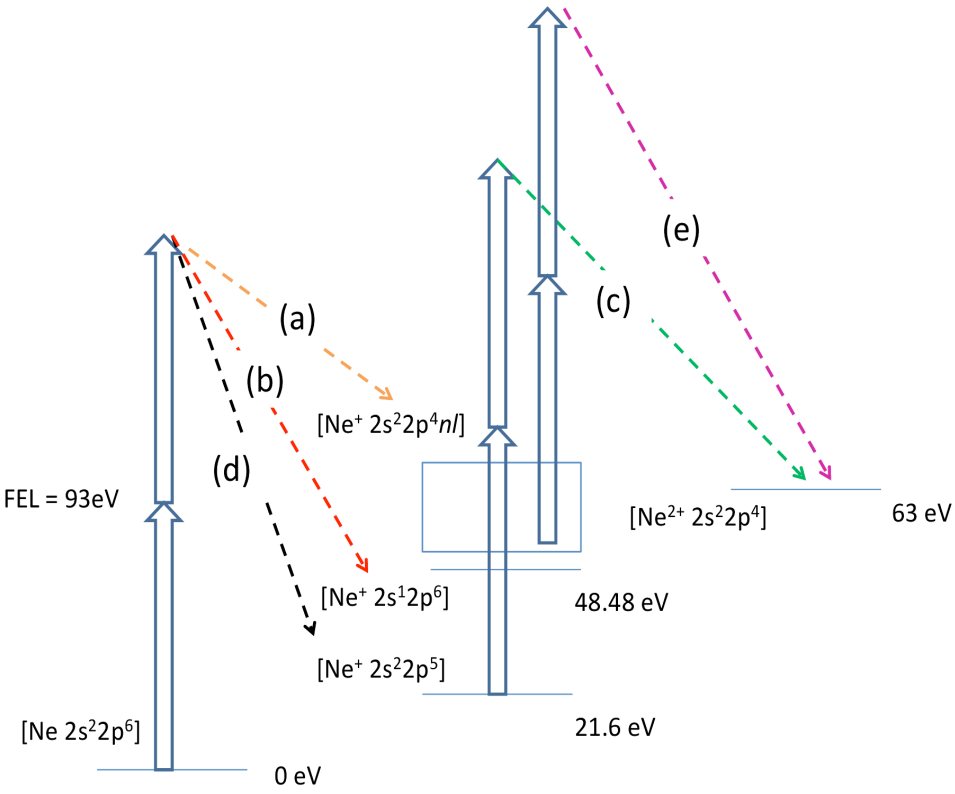

Figure 3.15: Schematic energy level diagram illustrating the variey of ionization pathways that make up Fig. 3.14. Labels 'a'-'e' correspond to those in Fig. 3.14. 'a' - orange, two photon ionization of ground state Ne leaving behind an excited Ne^+ state; 'b' - red, two photon ionization of a 2s electron from neutral Ne; 'c' - green, two photon ionization of a 2p electron from Ne^+ to produce ground state Ne^{2+}; 'd' - black, two photon ionization of a 2p electron from neutal Ne; 'e' - purple, two photon ionization of an excited Ne^+ state leaving behind a Ne^{2+} core in the ground configuration

overtakes the corresponding 2p value.

3.4 Chapter Summary

New insights have been gained into the field of non linear optical processes. Multiphoton ionization spectra of xenon and neon have been presented. The first observation of an inner shell, multiphoton ionization event has been made resulting from the 4d [156] and 5s subshells in Xe, and the 2s subshell in Ne. In addition the identification of numerous other ionization mechanisms has been made. As far as this author is aware, they are the first observations of such ionization pathways. The observations have been made possible by the ultrahigh intensity XUV radiation provided at FLASH. With the aid of state-of-the-art computational results

from H. van der Hart (Queen's University, Belfast), it is clear that multiphoton ionization of inner shell electrons can contribute to the overall ionization rate for atoms in intense XUV fields. The work demonstrates the significance of inner shells and inner-shell resonances in nonlinear multiphoton-matter interaction for experiments at the new EUV and X-ray laser facilities.

A additional result, pertaining to inner shell ionization in Xe at a photon energy of 46 eV can be found in Appendix A.

Chapter 4

Resonant Two Photon Inner Shell Excitation in Kr

4.1 Introduction

Two-photon excitation of a one-photon forbidden Auger resonance has been observed and investigated using the intense extreme ultraviolet radiation from the Free Electron Laser in Hamburg. At a wavelength of 26.9 nm (46 eV) two photons promoted a 3d core electron in a neutral Kr atom to an unoccupied outer shell, in this case the 4d orbital. This was made possible only by the absorption of two photons, each carrying half of the resonance energy. As this transition (nd→nd) requires two units of angular momentum, it is impossible to excite it with just a single photon. The inner shell hole is filled by an outer shell electron via a non-radiative transition, with the excess energy being transferred to another outer-shell electron. This electron now has enough energy to become unbound and enter the continuum in a process known as Auger decay. As the first step is resonant, the whole process is referred to as Resonant Auger Decay. Here, results on the pathway Kr($3d^{10}$) + $2h\nu \rightarrow$ Kr* ($3d^{9}_{5/2}4d$) - Kr^{+} + ϵl. In addition, above threshold ionization (ATI) of the outer 4p and 4s shells of Kr and Kr^{+} was observed

4.1.1 Auger Spectra by Photon and Electron Impact

The Auger spectrum of Kr has been previously studied in some detail. Using the electron impact technique, the first detailed interpretation of the Auger spectra of Kr ($L_{2,3}MM$and$M_{4,5}$NN) and Xe ($M_{4,5}$NN and $N_{4,5}$OO) was published by the group of Werne *et al* [158] (Fig. 4.1). Earlier attempts had been hampered by limited energy resolution [159].

The spectra were reinvestigated by the group of Ohtani *et al* [49], this time how-

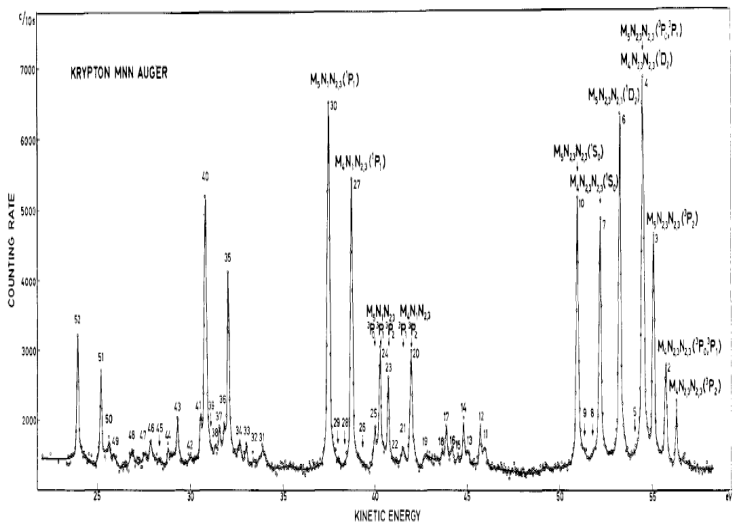

Figure 4.1: A high resolution Kr $M_{45}NN$ Auger electron spectrum as presented in [158]. Numerous satellite and shake-up lines have been identified with the help of relativistic calculations utilising Hartee-Fock-Slater type electron orbitals in order to calculate energy levels.

ever at a lower impact energy closer to the M shell ionization threshold. This ensured that ionized electrons were relatively slow, and resulted in a greater degree of electron correlation and post-collision interaction (PCI). A shift in the Auger electron line energies was observed along with a corresponding asymmetric line broadening. Using a synchrotron source (i.e. photon impact), Schmidt *et al* [160] examined closely the role of PCI for threshold N-shell ionization of Xe, first looking at a single isolated Auger peak ($N_5O_{2,3}O_{2,3}$ $^1S_0$) and subsequently the whole $N_{4,5}O_{2,3}O_{2,3}$ Auger spectrum [161]. In 1976, the first results appeared in which Auger decay via a resonant first step was investigated. In [162], the 3d→5p and 4d→6p transitions of Kr and Xe respectively were excited with the use of bright synchrotron radiation. It was noted that the resultant spectator Auger decay spectrum was shifted somewhat due to the increase in binding energy felt by the 6p (Xe) and 5p (Kr) subshells as a result of the inner shell vacancies created in the process and consequent decrease in screening. This was followed up in the 1986 work of Aksela *et al* [163] and [164], in which detailed comparisons of line intensities and relaxation mechanisms were made with theory.

A study of the angular distribution of the Auger decay features of a number of atoms (Ar, Kr, Xe) was initiated in 1988 by the group of Carlson *et al* [166, 167] who used a resonant first step and later again in [168] by the group of Kammerling. The unusual degree of angular anisotropy attracted much attention from theory (see [169] for an early work, and references therein), from which it was deduced that the angular distribution was governed primarily by two processes - the de-

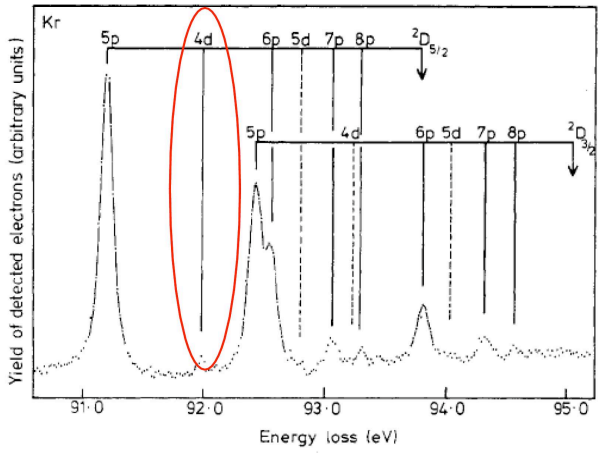

.]Energy-loss spectrum of atomic krypton obtained by electron impact. Here, the $3d_{5/2}$ and $3d_{1/2}$ core electrons have been promoted into empty valence shells, including the optically forbidden 4d orbital [165].

gree of alignment of the target atom, and the anisotropy of the individual Auger decay pathways. This group also presented high photon and electron energy resolution measurements of the angular anisotropy of a number of individual Auger decay mechanisms via a resonant excitation, along with a comprehensive comparison with multiconfiguration Dirac-Fock (MCDF) calculations [170].

Electron energy loss spectroscopy (EELS) is used to obtain excitation spectra, and is useful for identifying available excitation pathways. By employing high-resolution EELS, King *et al* [165] identified an optically forbidden series of the form 'md→nd' and extracted lifetimes for a range of rare gases. A sample electron-loss spectrum is reproduced in Fig. 4.1.1. Most recently, the subject of 3d inner shell ionization has been investigated by the group of Yuan *et al* in [171] using an electron energy loss spectroscopy (EELS) technique similar to [165] to investigate and identify some additional optically forbidden transitions, as well as extracting a value for the lifetimes of a range of levels.

4.1.2 From Single to Multiphoton Processes

Phenomena such as multiphoton multiple ionization, above threshold ionization (ATI), and high order harmonic generation span the broad range of strong field physics that has until recently been restricted to interactions with infrared and optical radiation, as detailed in e.g. [172, 173, 174]. As a result of the low photon energy for optical lasers, only the outermost electrons are removed and multiple ion-

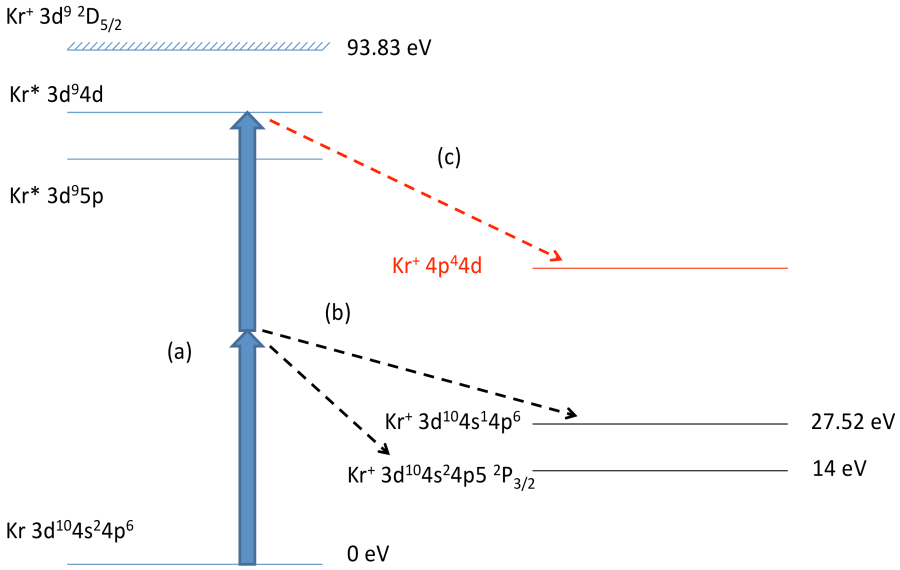

Figure 4.3: Energy level diagram and excitation scheme for atomic Kr. (a) Excitation by 46 eV FEL photons (b) Scheme for direct one photon ionization. One photon is enough to cause $4s^{-1}$ and $4p^{-1}$ ionization. (c) Resonant 3d-4d step and subsequent Auger decay scheme

ization is obtained via successive stripping of the outer subshell. In contrast, short-wavelength radiation couples predominantly to electrons in deeper, more strongly bound shells, producing corehole states, which decay primarily by ultrafast Auger decay. The opportunity to study the underlying multiphoton dynamics arises only now with the availability of free electron lasers (FELs) in the extreme ultraviolet (XUV) to hard-x-ray wavelength regime [3, 175, 176]. As mentioned in the previous chapter, the investigation of nonlinear interactions using FELs started recently and has already revealed several new phenomena; for example, the formation of very high charged states [29, 146] and two-photon double ionization [177, 178], both of which uniquely require high intensity XUV radiation.

A unique insight into the interaction between matter and strong XUV fields is given by resonant two-photon inner-shell processes. Firstly, two-photon processes enable the study of a class of resonances which are inaccessible in a single-photon process from the ground state. Secondly, inner-shell resonances are characterized by an increase (compared to the non-resonant case) of the photoionization cross section - so-called 'photoionization maxima'. The lifetime of a core hole of the order of several femtoseconds is determined by Auger processes, and the excitation in

strong XUV fields of similar durations will inevitably result in competition between sequential ionization and Auger decay.

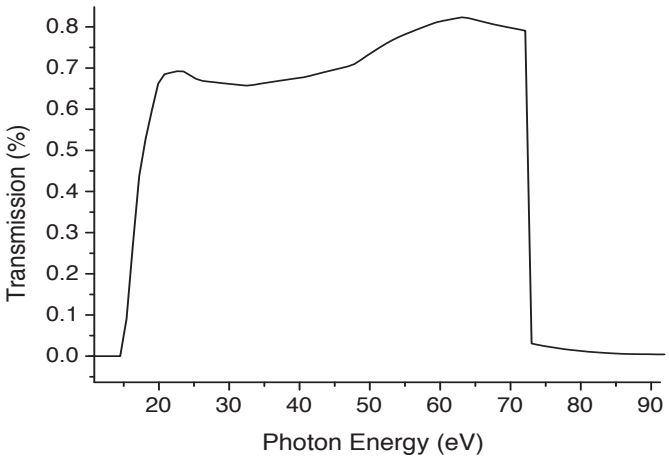

Figure 4.4: The transmission curve for a 100nm thick Al filter, coated with a thin layer of Al_2O_3. Whilst attenuating the fundamental mode of the 46 eV FEL by approximately 30%, importantly it completely blocks the second harmonic at 92 eV.

4.2 Experimental Setup

Using a setup similar to that described for Xe two photon non-resonant ionization at 93 eV, but with the multi-layer mirror switched to one that reflects at 46.1 eV, an experiment was carried out in order to observe a two photon inner shell excitation in Kr, specifically the $3d^{10}(4s^24p^6) \rightarrow 3d^9(4s^24p^6)4d$ resonance. Using photoelectron spectroscopy, a signature of this process was observed, specifically Auger decay of the neutral Kr $3d^94d$ excited state leaving the Kr^+ ion in the Kr^+ $4s^24p^44d$ excited state. The production of this state results from the filling of the 3d vacancy by a 4p electron, and subsequent ionization of another 4p electron. The excited 4d electron remains excited and does not partake in this decay, so the overall process is known as spectator Auger decay, and the pathway is illustrated in Fig. 4.3.

The experiments were performed on beam line BL2 at FLASH using an experimental setup for electron spectroscopy similar to that described earlier in Ch.2. The FEL was operated in single-bunch mode at a 5 Hz repetition rate and a fundamental wavelength of 26.9 nm (46 eV) with a mean pulse energy of 12 μJ as measured online for each pulse using a gas-monitor detector [101]. In this wavelength region the temporal width of the pulses is of the order of 30 fs [179]. The FEL beam was focussed to a diameter of about 5μm in the acceptance volume of a magnetic

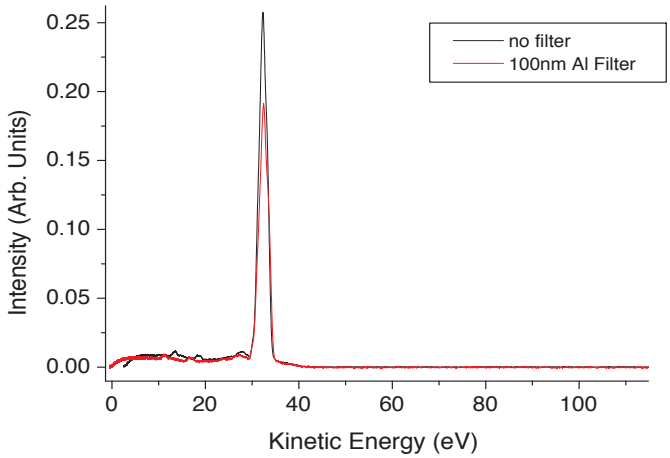

Figure 4.5: Photoelectron spectra taken with the unfocused FEL beam only. The one photon $4p^{-1}$ photoelectron line intensity is reduced to 72% of its initial value with the introduction of a 100 nm aluminium filter. It is clear from this spectrum that there is no significant presence of the the second harmonic, which would result in weak photoelectron lines in the higher kinetic energy regions.

bottle electron spectrometer (MBES). Focusing was obtained by a spherical Mo/Si multilayer mirror (reflectivity of about 40%) mounted at the rear of the vacuum chamber. By introducing a small angle (5°) between incoming (unfocused) and reflected beams, only the focused beam interacted with the gas target. Taking into account the reflectivity of the mirror, an intensity of more than 5×10^{14} Wcm^2 was obtained at the focus. The spectral bandwidth of the FEL pulses was measured to about 0.25 nm (0.43 eV) and was therefore larger than the natural width of the Kr* $3d^{-1}$ hole state (about 120 meV). As a result of the fluctuation of the spectral profile, a strong FEL pulse does not always lead to a strong resonant excitation. For this reason, the electron spectra were recorded by averaging over many FEL pulses and normalized to the average intensity. The base pressure in the chamber was below 10^{-8} mbar and experiments were carried out with a Kr gas target pressure of 3×10^{-7} mbar.

A range of filters is available for use at the beamline designed to selectively attenuate either the fundamental or second harmonic of the incoming FEL beam. For the purpose of this experiment, a 100 nm aluminium filter was used in order to pass the fundamental (at reduced transmission) and to completely block the second harmonic. This was the primary method of discerning those signals arising from two photon processes, and those from one photon second harmonic ionization. The transmission curve of the filter is displayed in Fig. 4.4. To be specific, it is the curve for a 100 nm Al filter coated with a 2 nm Al_2O_3 layer due to oxidation over time.

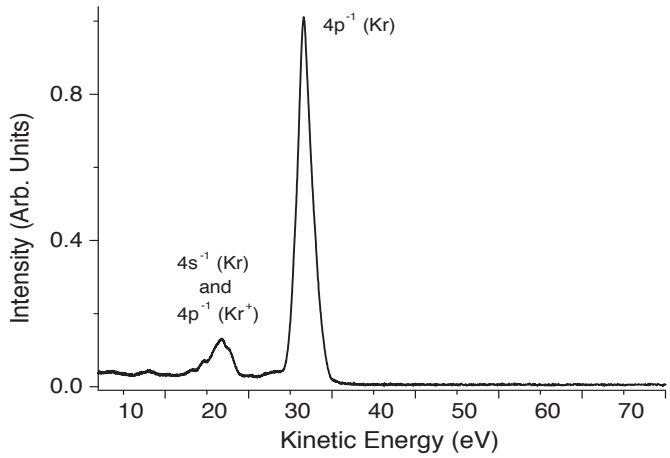

Figure 4.6: Electron spectrum produced by the interaction of FLASH operating at a photon energy of 46 eV with a Kr gas target. The data was obtained at the lowest irradiance used in the experiment, of the order of 10^{10}Wcm^{-2} in order to prevent saturation of the signal. The spectrum is dominated by the one-photon ionization of the 4p subshell from atomic Kr, and there is also a small contribution from 4p ionization from Kr^+ and 4s ionization from neutral.

A sample photoelectron spectrum is displayed in Fig. 4.5. The spectrum consists of a peak at 32 eV due to single photon ionization of a 4p electron in Kr from a very dilute gas target. The pressure in the chamber for this measurment was maintained at only 8.3 $\times$ 10^{-8} mbar, in order to be sure that the line was not saturated. On insertion of the filter into the path of the beam, the intensity of the photoelectron signal was attenuated to 72% of its original value, in line with the Al filter transmission of approximately the same value.

4.3 Results

Fig. 4.6 shows a typical photoelectron spectrum of atomic Kr recorded under the above conditions. This spectrum is dominated by the strong photoline at 32 eV kinetic energy due to single-photon ionization of the 4p electron leading to the Kr^+4p^5 final electronic state. The two spin-orbit components $^2P_{3/2}$ and $^2P_{1/2}$, being separated by only 0.66 eV, are not resolved in the present experiment. The small feature at about 20 eV arises from sequential two photon ionization of a second 4p electron from the Kr^+ion, as well as from a contribution from ionization of the 4s shell. The cross section of Kr(4s) ionization at 46 eV is more than 2 orders of magnitude smaller than that of Kr^+(4p), and, therefore, most of the intensity at 20 eV can be attributed to the ionization of the Kr^+ ion. Calculations by P. Lambropoulos

Table 4.1: Comparison of experimental values obtained Fig.4.7 with expected values from NIST [154]. The binding energies are displayed here to make comparison with NIST easier.

Level		E_{exp} (eV)	E_{NIST} (eV)
$Kr^{+}_{3/2} \rightarrow Kr^{2+}4s24p4$	^3P	25.2	24.35
	^1D	26.6	26.2
	^1S	27.6	28.4
$Kr^{+}_{1/2} \rightarrow Kr^{2+}4s24p4$	^3P	25.9	25.01
	^1D	27.2	26.81
	^1S	27.9	29.11

[180] of the relative abundance of the Kr^+ ion as a function of laser intensity indicate that at even moderate intensities of 5×10^{13} Wcm^{-2}, the ratio of Kr neutral to Kr^+ is almost equal.

Spectra recorded with increased spectral resolution show the three components, namely ^{1}S, ^{1}D, and ^{3}P of the final Kr^{2+} 4p^4 electronic configuration, as seen in Fig. 4.7. The uncertainty in the energy calibration, retardation voltage and even

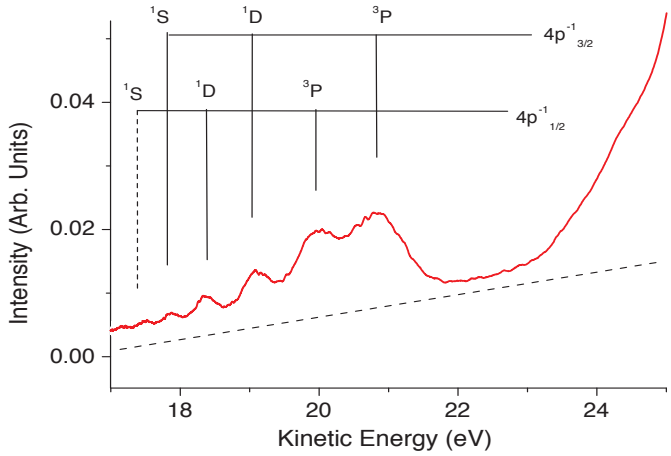

Figure 4.7: A high resolution photoelectron spectrum taken at a photon energy of 46 eV. The multi-featured structure and its component are tentatively assigned labels corresponding to 4p^{-1} ionization of Kr^+, producing a number of energetically different Kr^{2+} states.

photon energy make a completely definitive assignment far from certain, so the multi-featured structure and its components are tentatively assigned labels corresponding to 4p^{-1} ionization of Kr^+, producing a number of energetically different Kr^{2+} states. The data is tabulated for clarity in Table 4.1 along with the known values. The spectrum was obtained by sorting 1000 single shot spectra according

to the corresponding pulse energies, and, in this case, averaging the 100 spectra resulting from the most intense laser pulses.

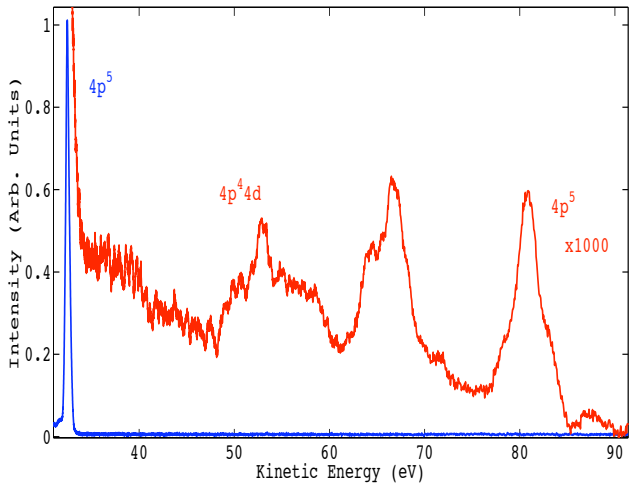

Figure 4.8: Electron spectrum of atomic Kr upon excitation by intense FEL radiation of 46 eV photon energy recorded by integrating the signal over 500 FEL pulses. The peak at 80 eV is due to two photon 4p ionization of neutral Kr. The structure centered at 65 eV is due to two photon 4p ionization of Kr^+. Finally, the structure in the region 50-60 eV is a result of the $3d^9 4d \rightarrow 4p^4 4d$ Auger decay.

In the region of high kinetic energies ($\geq$46 eV), where electrons are released by two-photon ionization processes, very small structures are observed, visible only after the intensity scale has been magnified by 3 orders of magnitude. The line at the highest kinetic energy (78 eV) results from two-photon ionization of the Kr(4p) shell, which is an ATI process. This simultaneous absorption of two photons by the 4p electron is, in accordance with theoretical estimates, about 500 times smaller than the corresponding one-photon absorption at FEL intensities of 5×10^{14} Wcm^2. The broad structure between 50 and 60 eV is attributed to the resonant Auger decay $Kr^* 3d^9 4s^2 4p^6 4d \rightarrow Kr^+ 3d^{10} 4s^2 4p^4 4d\ ^{2,4}L_J$. Only very few of these Kr^+ multiplet lines have been observed in the past, as small satellites in conventional photoelectron spectroscopy experiments [155], and it is, in that case, their resonantly enhanced intensity which allows for a detailed investigation of the multiplet structure. On the basis of energy considerations, the structure at 65 eV kinetic energy is assigned to the 4p ATI of the Kr^+ ion (See Fig. 4.8).

To exclude any influence of the second harmonic of the FEL (typically of the order of 0.1% - 0.5% of the fundamental beam energy [106]), complementary measurements were performed. A 100 nm Al filter was introduced in the path of the FEL, which reduced the intensity of the FEL at the fundamental wavelength (26.9 nm) to 70% and of the second order harmonic signal (13.45 nm) to 5%. The electron

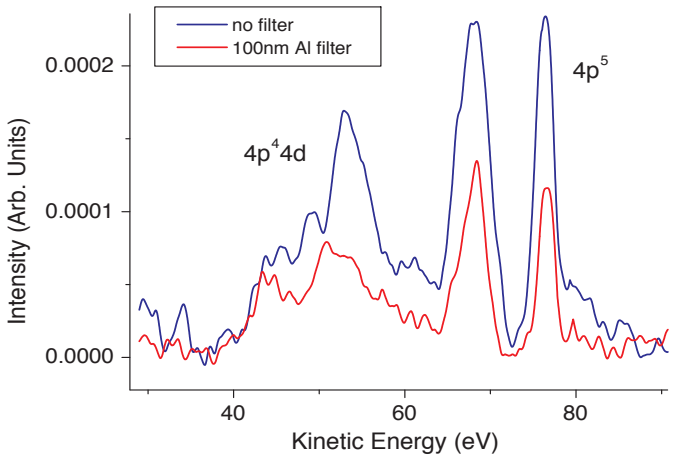

Figure 4.9: Electron spectra illustrating clearly the attenuation due to the insertion of an Al filter. The filter attenuates a one photon signal to 72% of its initial value. Therefore, a two photon signal should be attenuated to approximately $(0.72)^2$-52% of the unattenuated signal.

signal dropped to 53%, indicating that contributions from the second harmonics were negligibly small. This attenuation is highlighted in Fig. 4.9. In addition, the nearly quadratic dependence of the electron signal on the intensity of the incoming FEL light, i.e., $(0.7)^2 \approx 0.5$, is a clear signature of a two-photon process.

As further evidence, the structure below 60 eV almost disappeared when the wavelength of the FEL was slightly detuned to 27.8 nm (44.7 eV), i.e., out of resonance for the two-photon process. As can be seen in Fig.4.10, the lines in this spectrum are shifted slightly to lower kinetic energies as a result of the lower photon energy. Whilst the features at 78 and 65 eV are attenuated somewhat, the Auger feature below 60 eV is attenuated, confirming its dependence on the initial resonant exitation step.

The photoelectron spectrum resulting from the Auger decay has been computed by Dr. Stefan Fritzsche. The experimental and theoretical results are compared in Fig.4.11. The strength of the two photon 3d-4d coupling has been evaluated using the GRASP Dirac-Fock code [181]. The subsequent Auger decay rates were computed for all available energy levels using the RATIP suite of codes [182]. The calculated overall intensity for the two-photon processes corresponds well to the experimental values. Theoretically the two-photon processes are calculated to be about 10^3 times smaller than the one-photon processes at intensities on the order of 10^{14} Wcm^{-2}. Furthermore, the intensity ratios of most peaks, especially between the 4p line and the resonant Auger lines, is well reproduced. However, the kinetic energies of the Auger lines are 2 eV higher than the experimental values. The dif-

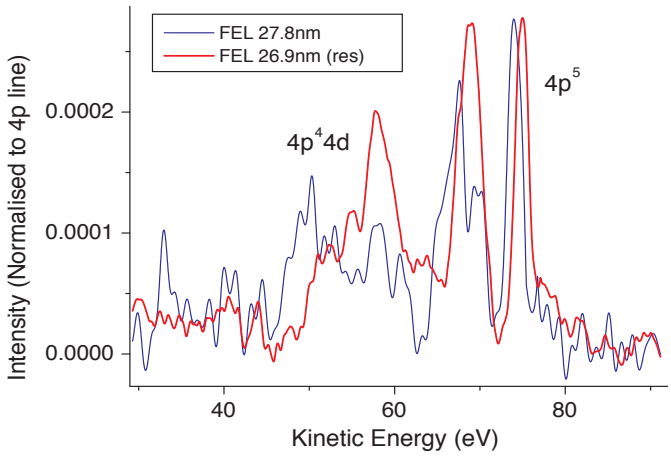

Figure 4.10: Photoelectron spectra for two different FEL photon energies - 26.9 nm (46.1eV) and 27.8 nm (44.7 eV). The spectrum taken at 27.8 nm has been normalised so that the 4p line due to two photon ionization is of equal intensity.

ference lies within experimental uncertainty though, and so the discrepancy could be due to approximations in the calculations, experimental error, or indeed both.

4.4 Chapter Summary

The interaction of intense short wavelength radiation with atoms has attracted some experimental and considerable theoretical interest as the need for further understanding of fundamental nonlinear optics continues to increase. In this chapter, an observation was made of an atomic two photon inner shell excitation via its resonant Auger decay spectrum [180]. Owing to the high intensity of the FEL pulse necessary for the observation of a specific nonlinear process, other processes such as non-resonant two photon 4p ionization from both the neutral atom and the ion, have been detected in the photoelectron spectra. The kinetic energy and relative intensities of the photoelectron lines has been reproduced well by a theoretical model. It is hoped that the strength of the transitions in this case can serve as a point of calibration for future experiments in atoms and matter in general.

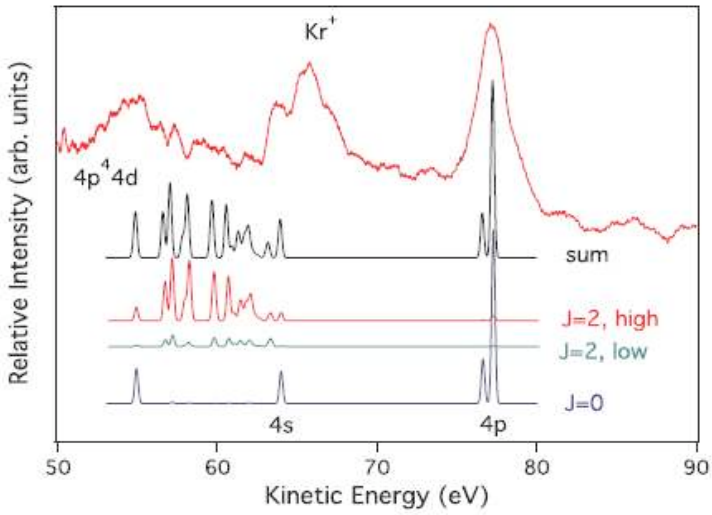

Figure 4.11: Experimental and theoretically generated electron spectrum of atomic Kr. The different excitation pathways are taken into account (i.e. J=0,2).

Chapter 5

Two-Colour Above-Threshold Ionization of Singly Charged Ne

5.1 Introduction

The results presented in this chapter are based primarily on the ionization of a gaseous neon target by combining extreme ultraviolet (XUV) radiation from the Free Electron Laser in Hamburg with an intense synchronized optical laser. The dependence of the photoelectron spectrum for the electrons ejected from singly-charged neon (Ne^+) on the relative polarization of the XUV and optical laser fields was investigated. It was found that it exhibited a strong dependence on the degree of alignment of the planes of polarization of the incoming laser fields and on the term structure of the residual doubly-charged ion. A quantitative analysis was undertaken with the aid of perturbation theory in order to reproduce the magnitude of these low kinetic energy electrons as a function of the relative field polarization directions. It is concluded that the variation of the photoelectron spectrum with the angular deviation of XUV and optical field directions is mainly related to the different responses of the magnetic substates of the ejected electrons in their interaction with the laser field.

It is well established that an electron promoted into the continuum in the presence of an intense optical dressing field may exchange photons with the optical field resulting in a gain or loss of kinetic energy equal to $\pm n h\nu$, where n is an integer and $h\nu$ the photon energy. The electron is said to have undergone transitions between two free states in the continuum. In a typical two-colour experiment, where an optical laser with an average intensity (10^{12} Wcm^{-2}), is overlapped in space and time with a beam of EUV photons from FLASH, the photoelectron spectrum consists of a main photoelectron peak, associated with the one-photon (EUV) ion-

ization event accompanied by sidebands, positioned either side of the main line. This phenomenon has been investigated recently in detail in, for example, [112], and in addition, has been the subject of a number of reviews [183, 184]. The effect of the optical laser can be summarised as follows: The sidebands confirm that the photoelectron is exchanging photons with the optical dressing field, and is gaining or losing energy in increments of $\hbar\omega_{IR}$. In addition, there may be a slight change in the kinetic energies of the peaks due to the ponderomotive shift (on the order of 0.05 eV for a dressing field of 10^{12} Wcm^{-2}). This last point is discussed in [185], where the relative shift in kinetic energy was measured as a function of dressing laser pulse energy. Finally, in the case of ultrashort optical dressing pulses (that is, comparable or shorter than to the EUV pulse duration) the features in the photoelectron spectrum may become broadened due to the fact that the intensity of the dressing field is not constant during the EUV field.

For the specific case of a singly charged neon ion, the intensity of the photoelectron sidebands will depend on the ratio of the amplitudes of the outgoing electrons, the analysis of which is complicated by the presence of a Ne^+ core in a variety of energy (i.e. angular momentum) configurations. With the aid of a theoretical model [186] a comparison is made with the experimental data, focussing on the dependence of the sideband intensity on the angular deviation between the polarization planes of the EUV and optical fields. It is hoped this will help to reveal, at least partially, the relative contribution that these ejected electrons make to the overall intensity of the sideband.

In Fano [187], the tendency of an electron to preferentially make a transition of the form $l \rightarrow l+1$ was discussed. Essentially, transitions involving an increase of the angular momentum are strongly favoured. For example, a 'p' electron, in principle, on absorption of a photon, has a higher chance of being promoted to a 'd' state than to an 's' state i.e. the cross section is dominated by the contribution by of 'd' waves. In the following sections, this propensity of the electrons to favour one angular momentum transition channel over another will be investigated.

5.1.1 FELs and Multiphoton Ionization

With the advent of higher intensity and higher photon energy light sources, the field of light-matter interaction is revealing new insights into the structure and dynamics of the atom. This work, carried out at the Free Electron Laser in Hamburg (FLASH) [3], is focused on improving the understanding of the photoelectric effect in intense electromagnetic fields. Unique to FLASH is its unprecedented XUV flux, monochromaticity and intensity in the 6 - 60 nm wavelength band, leading to interesting and often surprising multiphoton processes in the short wavelength laser

regime [188, 189, 190].

Single colour multiphoton experiments on dilute samples with ultralow photoionization cross sections [191], few photon processes in few electron systems [178], and two colour pump-probe experiments on a femtosecond time scale [192] are all made possible with the advent of ultrafast XUV [3, 193] and X-ray FELs [176, 194]. Two-photon double ionization (TPDI) of valence shell electrons via a sequential pathway has been made possible, as previously observed in He and Ne [195], and via a nonsequential scheme as in [196]. More recently, three photon ionization via a resonant second step was reported for Ar [197]. In addition, one colour experiments on non-linear interactions have been carried out using XUV radiation from high harmonic generation or HHG sources, in which doubly charged Helium was observed as a result of sequential two photon ionization [143, 142].

In complementary studies, two colour multiphoton experiments have been underway for many years, in which the XUV HHG field is combined with a second, IR field. In this class of experiment, electrons ionized by the XUV laser are born directly into the second IR field and undergo 'free-free' transitions, that is, they absorb and emit additional photons in the continuum [198, 199]. It was found that the strength and nature of these free-free transitions is critically dependent on the temporal separation [185] and relative polarization of the two laser fields [200, 201]. Recently, the angularly resolved above threshold ionization spectra of Ar [202] and He [203] were investigated using a velocity map imaging (VMI) technique, and expressions for the two photon ionization anisotropy and cross sections were derived.

However, contributions to the ATI processes must take into account the fact that the harmonics are phase related, as are the corresponding photoelectron waves. As these waves are mixed with the original optical laser field one must account not just only the stimulated emission/absorption process but also for the role played by the coherence between the electron waves and the dressing field which give rise to the harmonic 'parents' of the electron waves. Unravelling the interference effects from the experimental data is very complex and nigh impossible in some cases. However, the monochromaticity of the FLASH laser-like radiation allowed these studies to be carried out in an entirely interference free regime [204], essentially enabling scrutiny of any two-colour multiphoton ionization channel without additional overlapping contributions from neighboring harmonics. Furthermore, the observed sideband structures represent an important testing ground for the fundamental theory of photon-atom interactions, since they are the direct signatures of the combined action of the XUV and optical fields. Theoretical studies have established that the sideband intensity depends on the kinetic energy of the liberated electron as well as on the strength and polarization state of the optical laser field

[205]. Fitting theoretical profiles to the measured sideband signals should yield the main parameters which govern the photon-atom interaction in this regime. For example, changing the polarization state of either of the radiation beams gives rise to dichroic effects in the photoelectron spectrum. It therefore opens up the possibility to control the relative contributions of photoionization channels with different angular momenta.

In [204], the polarization dependence of two-colour above threshold ionization in helium was studied. In this experiment an electron from the 1s subshell of helium was promoted into the continuum where it was subject to the IR dressing field with which it could exchange photons. The relative angle between the polarization planes of the FEL and optical lasers was varied, and the sideband intensity was tracked as a function of said angle, as can be seen in Fig. 5.1. It was found that the electron emission was very sensitive to this angle, and a notable modulation in the main features of the photoelectron spectra was observed. The resultant sideband intensity (in the case of a relatively low optical laser field) is directly related to the ratio of the 's' and 'd' waves i.e. it constitutes a measure of how likely a 'p' state becomes an 's' or a 'd' state following absorption of an additional photon.

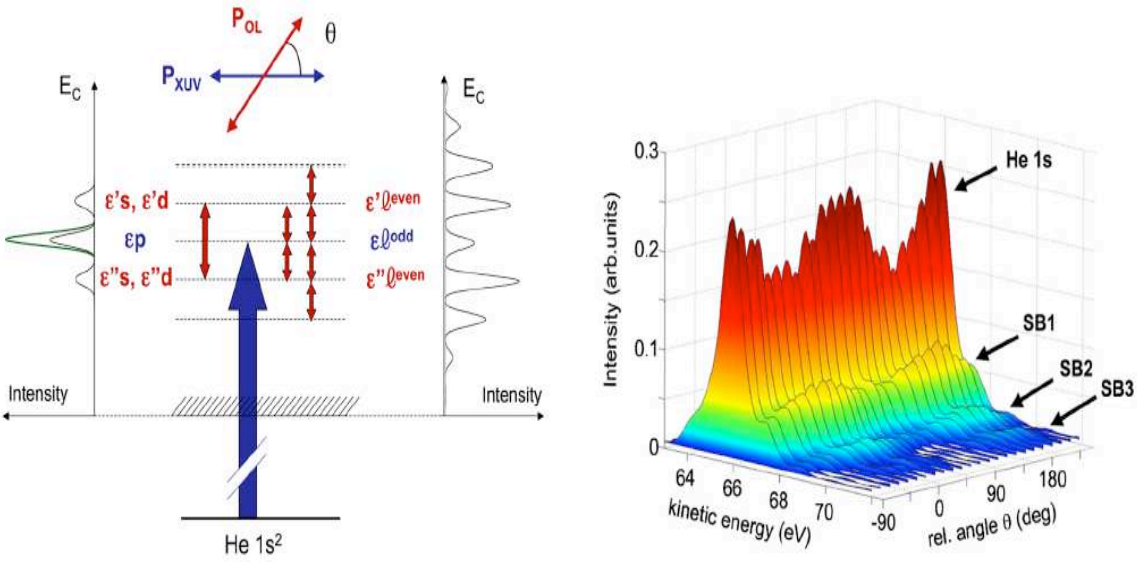

Figure 5.1: Scheme of the two-colour above threshold ionization in He atoms and resultant photoelectron lines. The optical laser dressing field intensity is estimated to be 6×10^{11}Wcm^2. In this case, the FEL was operated at a photon energy of 90.5 eV. Spectra are presented for different relative orientations θ between the linear polarization vectors of the FEL and the 800 nm laser [204].

5.2 Experiment

Operating at wavelengths of 26.9 nm (46.1 eV) and 800 nm (1.55 eV) respectively, the two linearly polarized laser beams were introduced into the vacuum chamber collinearly. The photoelectron spectrometry setup has been described in detail previously (Chapter 2.3 and [100]). The FEL was operated in single bunch mode with a pulse duration 10-20 fs at a pulse energy of approximately 15 μJ, whilst the IR beam for synchronisation purposes was operated at 3 ps pulse width at mJ pulse energies. For beam diameters of 30 μm (FEL) and 50 μm (IR), upper intensity limits of 10^{11} Wcm^{-2} and 10^{13} Wcm^{-2} for the IR and FEL fields respectively were achieved. A gas jet nozzle was positioned in the path of the two beams at the entrance aperture to our time-of-flight spectrometer. The optimum gas pressure, that is, that pressure which results in the maximum signal before space charge effects [103] begin to dominate, was 1.5×10^{-7} mbar. This compares to a base pressure in the chamber of approximately 10^{-8} mbar. The angle of polarization of the IR beam was rotatable relative to that of the FEL beam using a half-wave plate. By employing a magnetic bottle type electron spectrometer, we obtained excellent single-shot collection efficiency at the expense of angular resolution. Single-shot spectra were recorded with the aid of a digital oscilloscope. The resolution of the electron spectrometer was approximately 5% of the electron kinetic energy, and also by the bandwidth of the FEL, estimated at 1%.

5.3 Results

Ionization of neutral neon by the FEL at 46 eV provides the primary Ne^+ target, as illustrated in the Fig. 5.2. The availability of the Ne^+ ground state opens up the possibility of exploring the polarization dependence of ATI in an ion species, and also for electrons that have relatively low kinetic energy (i.e. less than 1 eV). It is of course important to note that photoelectron spectroscopy has indeed been used as a tool to investigate ionic species in the past, see for example [206, 207, 208, 209], however previous studies have been limited somewhat by the low achievable ionic target densities. It is at these low kinetic energies that the analysis of the outgoing electron waves using the Soft Photon Approximation is no longer trivial [205], as the photon energy of the secondary laser field is now comparable to, as opposed to far less than, the kinetic energy of the photoelectron. In a second step Ne^+ is ionized producing Ne^{2+} (with an electron configuration of $2p^4$, giving rise to terms $^1D_2$ and $^3P_{2,1,0}$). Each corresponding photoelectron carries a kinetic energy characteristic of the corresponding binding energies. As the ^3P states lie lowest in Ne^{2+} they give rise to electrons with the highest kinetic energy, and vice versa, for

the ^{1}S, as can be seen in Fig. 5.3. The spectra of Fig. 5.3 therefore are dominated by two photoelectron lines, corresponding to ionization of Ne^+ ^{1}D, binding energy 44.2 eV, and ^{3}P with a binding energy of 41 eV.

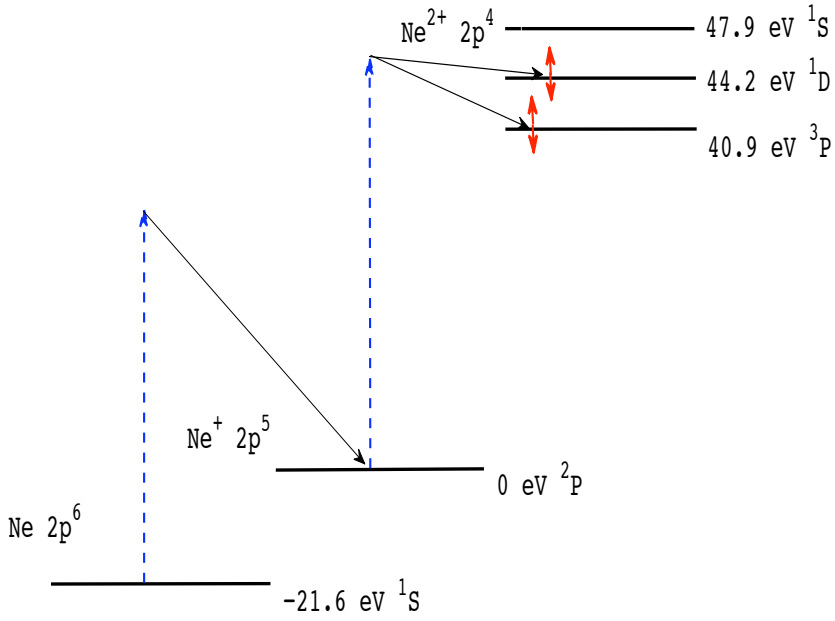

Figure 5.2: Schematic binding energy level diagram illustrating a sequential two photon double ionization (TPDI) scheme in Ne for an FEL photon energy of 46 eV and IR laser energy of 1.55 eV. This scheme illustrates an indirect, sequential pathway, as distinct from a direct process, in which two photons eject two highly correlated electrons in one step producing Ne^{2+} [210, 195]

When the optical laser field overlaps the FEL field, the photoelectrons are born into an intense dressing field with which they exchange photons, resulting in so-called 'sidebands'. Since they are dressed by a single laser field, they are coherently coupled and therefore each of the dressed free electron waves are phase related. However, these outgoing electrons see different ionic cores and hence different coulombic potentials. As mentioned above, these induced sideband signals are the results of two or more photon processes (i.e. ionization by the initial XUV pulse, followed by above-threshold ionization by the overlapped IR field), and so these signals are composed of multiple outgoing electron partial waves, the ratio of which is determined by electronic dipole selection rules. In the case of a photoionized 'p' electron undergoing stimulated emission and absorption by a second linearly polarized electric field, the allowed transitions are denoted by $\Delta l = \pm 1$ and $\Delta m_l = 0$ for parallel fields, and $\Delta m_l = \pm 1$ for perpendicular orientation.

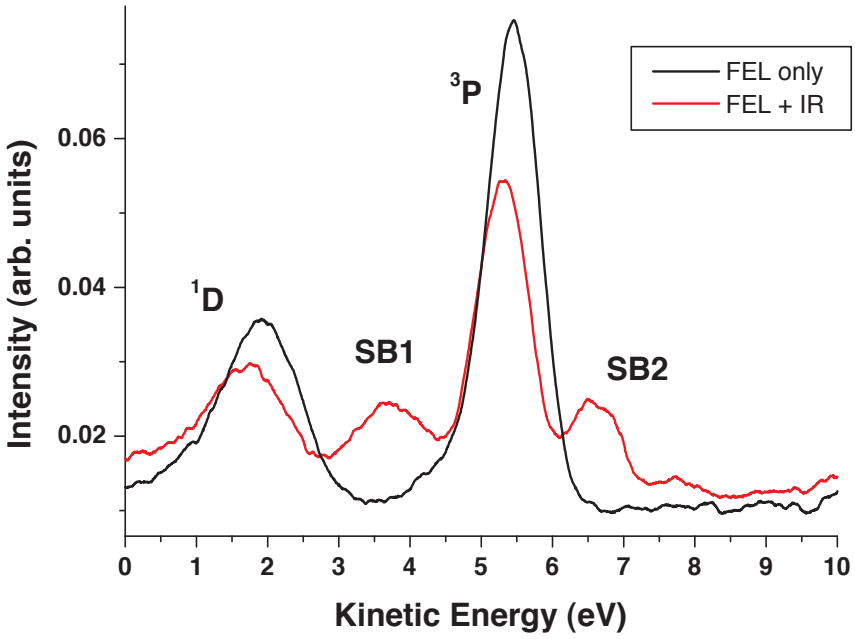

Figure 5.3: Sample photoelecton spectra showing evidence of TPDI (black) and those additional features induced by the IR laser field (red) The sidebands are separated from the main photoelectron lines by 1.5 eV, i.e. the energy of the dressing laser field. The sideband signal contains a small contribution from the one colour (XUV) photoionization lines as a result of the 'wings' either side of the lines. The overall number of electrons in the main photoline and the sidebands remains constant throughout. The IR laser is plane polarized and aligned parallel to that of the FEL to ensure maximum photoelectron energy redistribution.

In Fig. 5.4 and Fig. 5.5, a series of experimental and theoretically generated spectra are shown in which the relative polarization of the IR laser was rotated through 180°. It is clear that the electron emission is very sensitive to this angle, and a notable modulation of the signal intensity is observed. The sidebands are strongest when both the polarisation states of the IR and FEL are parallel, and weakest for perpendicular alignment. Labels are assigned to the peaks as illustrated in Fig. 5.3. The peaks at kinetic energies of 2eV and 5eV we designate as photoelectrons from the Ne^+ target resulting in a Ne^{2+} core in a ^{1}D and ^{3}P configuration, respectively. The feature at 6.5 eV and small feature just below 8 eV are ATI sidebands resulting predominantly from one and two photon absorption respectively. The feature at 3.5 eV is a blend of a low energy sideband from the ^{3}P electron and a high energy sideband from the ^{1}D electron. In order to map the angular anisotropy of the photoelectrons and to determine the contribution each possible pathway makes to the photoelectron spectrum, the amplitude of the sidebands as a function of the

angular deviation between the XUV and IR laser fields was examined closely. This analysis allows one to scrutinise in detail the underlying ionization dynamics of two colour multiphoton ionization by employing a detailed theoretical model.

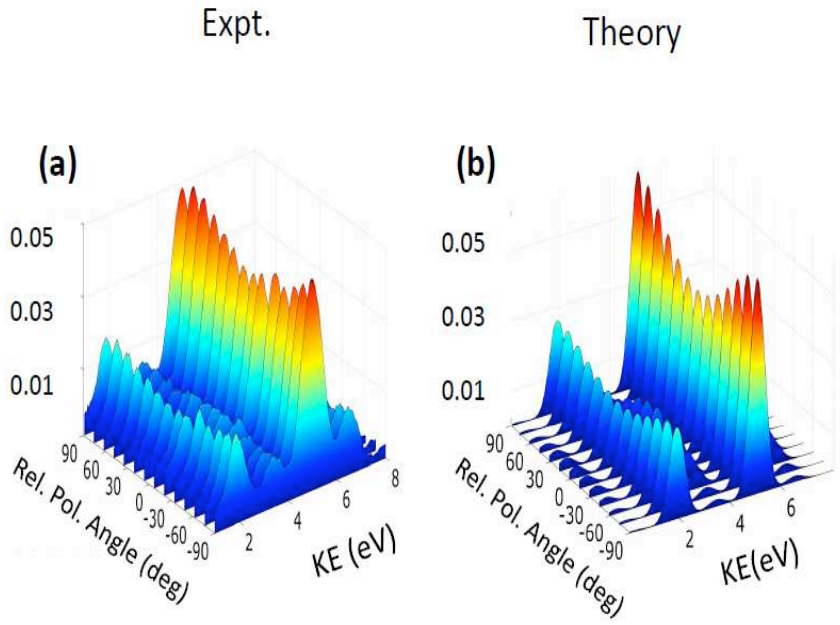

Figure 5.4: Recorded experimental and theoretically generated photoelectron spectra displayed as a function of polarization angle. The intensity of the IR dressing field is estimated at 1×10^{11} Wcm^{-2}. Complete experimental (a) and theoretical (b) spectra of two colour ionization of Ne^{+}.

5.4 Theoretical Framework

A brand new theoretical model was written by Dr. Lampros Nikolopoulos, Dublin City University, for the purpose of interpreting the results presented in this chapter. The full framework is to be published in the near future, but for now a brief summary of the approach, in which the most salient details and equations employed by this author in the course of the analysis is given.

To recap briefly, in this section what is under investigation are the processes involved in the ionization of the Ne atomic system in its ground state $|g; J_g M_{J_g}; L_g S_g\rangle = |(1s)^2 2s^2 2p^6\, {}^1S_0\rangle$ in the presence of two linearly polarized fields along different axes (polarization angle θ_p), with central frequencies $\omega_F = 46.1$ eV and $\omega_L = 1.55$ eV (as shown schematically in Fig. 5.2). The pulse duration (FWHM) of the two fields is about 20 fs for the FEL and 3 ps for the laser field (labelled IR in the figure). The intensity of the IR field is sufficiently low so that the neon is ionized exclusively by the FEL field, by promoting one bound electron from the valence shell

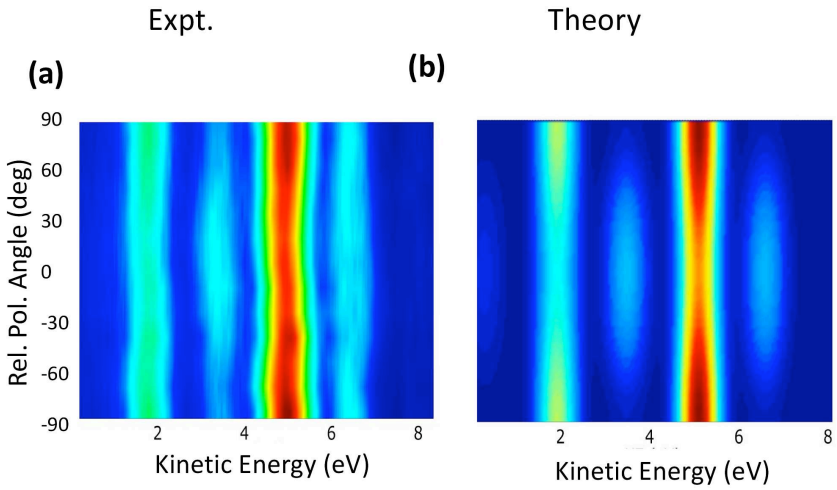

Figure 5.5: Fig.5.4 reproduced again, this time rendered in 2D for clarity. Experimental (a) and theoretical (b). The false colour scheme is identical to that in Fig. 5.4.

$(2p)$ to a continuum state and the residual ion is left in its ground configuration $|i; J_i M_i; L_i S_i\rangle = |1s^2 2s^2 2p^5; ^2P^o_{j_i}; M_{J_i}\rangle$ with $J_i = 1/2, 3/2$. The ionization potential is $\epsilon_i - \epsilon_g = 21.564$ eV. The spin-orbit (SO) splitting between the two ground ionic states is given by $\Delta E_{SO} = 0.0967$ eV. The production of singly-charged ions is followed by the ionization of Ne^+ ions leading to the ejection of yet another electron from the valence shell. Again the dominant channel for Ne^+ ionization is the absorption of an extra FEL photon. The doubly ionized Ne^{2+} states and the dominant ionization pathways are determined by energy and angular momentum conservation arguments and consist of the four ionic states $|f; J_f, M_f; L_f, S_f\rangle = |1s^2 2s^2 2p^4; ^1D_0\rangle, |1s^2 2s^2 2p^4; ^3P_{0,1,2}\rangle$ plus an extra electron in a continuum state. Therefore, the final states of interest will consist of two continuum electrons, ejected sequentially from the valence shell $(2p)$ of the neutral and singly charged neon, and the ground states of the doubly charged neon ion. The two continuum electrons are evolving in the presence of a relatively short duration FEL field (of the order of 10 to 20 femtoseconds) and a relatively long laser field (on the order of picoseconds). Thus, given the experimental measurements the important consideration is the interaction of these (continuum) electrons with laser field. The IR laser essentially plays the role of a 'probe field' with the task of investigating the response of that particular electron to the polarization state of the laser.

The formal treatment of double ejection from a multielectron atomic system is rather intricate as it involves a number of intertwined effects [211]. The double

ionization of an atom can proceed via a sequential process, in which successive electrons are removed one after another via separate pathways. The resulting ion can be left in states other than the ground configuration, depending on the branching ratios involved in the relaxation process. However, another mechanism, known as direct double ionization, involves the simultaneous absorption by a correlated pair of electrons of one or more photons. It is difficult to detect signatures of this pathway, however, using conventional photoelectron spectroscopy, as the pair of electrons essentially share the photon energy; hence any signal appears as a continuous background. In addition, for relatively large atoms, the effect of the multielectronic core needs to be taken into account. In the present case the successive, well justified approximations based on the above mentioned experimental conditions, leads to a satisfactory and realistic description of the relevant processes. In addition, due to the relative weakness of the laser field with (compared to the FEL field), the present theory focuses only on the first sidebands disposed on both sides of the main FEL ionization peaks which correspond to the emission/absorption of one single IR photon.

Given the experimental FEL bandwidth (which is greater than the energy difference ΔE_{SO}), the $^2P_{1/2,3/2}$ SO doublet is unresolved, thus allowing the results to be interpreted by considering only LS coupling instead of the conventional $LSJM_J$ intermediate scheme normally employed when the SO interaction must be considered. In addition, due to the large kinetic energy difference between the two sequentially ejected electrons, from Ne and Ne^+ respectively, any correlation between them due to Coloumbic interaction is ignored. In addition, the present theoretical interpretation of the experiment should also involve a summation over all dynamic variables of the electron ejected from the neutral since the experiment detects only the electron ejected from the Ne^+.

By taking into consideration the above mentioned approximations, a set of differential equations (TDSEs) written in terms of amplitudes $u_c(t)$ and $u_f^{(C)}(t)$ is obtained (see Appendix A). In the TDSEs, $|u_c(t)|^2$ and $|u_f^{(C)}(t)|^2$ represent the probability as a function of time of the Ne^{2+} continuum being reached sequentially through the ion stage Ne^+ with the absorption of one FEL photon (main peak) and the absorption/emission of an IR photon (sidebands peaks). The superscript C in the amplitude $u_f^{(C)}$ represents its association with the core states the ion is left in after ejection of the electron. A direct interpretation for the amplitude $u_f^{(C)}(t)$ can be understood from the following: Since the $|u_c(t)|^2$ represents an electron in a continuum state with quantum numbers $\epsilon_c l_c m_c$ in the presence of the core C, then the amplitude $u_f^{(C)}(t)$ describes the probability for the same electron, due to its interaction with the laser field, to change to a continuum state with quantum numbers

$\epsilon_f \sim \epsilon_c \pm \omega_l, l_f = l_c \pm 1, m_f = m_c \pm 1, 0$, in the presence of the same core C. The above interpretation shows that interference effects from electrons ejected from different cores are quantum mechanically impossible and the contribution from different cores should be added incoherently.

The particular geometry of the laser field with respect to the FEL field, expressed here through the dependence on polarization angle θ_p of the dipole matrix element $D_{cf}^{(IR)}(\theta_p)$ involved in the continuum (c)$\rightarrow$ final (f) state transitions and the effective ionization width $\gamma_c^{(IR)}(\theta_p, t)$, has a direct influence on the available magnetic substates involved in the transition. For example when the two fields are in a parallel configuration ($\theta_p = 0^\circ$) only $m_f = m_c$ transitions are allowed and when they are in a perpendicular configuration only ($\theta_p = 90^\circ$) only $m_f = m_c \pm 1$. For any other polarization angle θ_p between 0^o and 90^0 all magnetic substates are available however with transition amplitudes that depend on the actual value of θ_p.

Fortunately, the fact that both the FEL and the IR fields contain a large number of cycles and the peak intensities are within the perturbation theory regime allow the derivation of a semi-analytic expression for the observed photoelectron kinetic energies. The expression depends on the set of salient atomic parameters, namely the relevant dipole matrix elements and potential energies.

By assuming a low intensity laser field, the expression for the first lower and upper sidebands with core $C =^1 D,^3 P$ is approximately given by:

$$\begin{aligned} S_C(\theta_p) &\sim \bar{\gamma}_g^{(FEL)} \sum_{l_f m_f} | \sum_{l_c m_c} \frac{D_{fc}^{(IR)}(\theta_p, t) D_{ci}^{(FEL)}(t)}{(\epsilon - \bar{\epsilon}_f)^2 + \bar{\gamma}_i^{(IR)}(\theta_p)/2} |^2 \\ &\sim A_{\parallel}^{(C)}(\epsilon) \cos^2 \theta_p + A_{\perp}^{(C)}(\epsilon) \sin^2 \theta_p \end{aligned} \tag{5.1}$$

with $\bar{\epsilon}_f$ the positions of the main photoelectron peaks. The term $D_{fc}^{(IR)}(\theta_p, t)$ contains information regarding the transitions induced by the IR laser between final and continuum states as a function of polarization angle and time. The expression $D_{ci}^{(FEL)}(t)$ contains the matrix elements involved in characterising transitions of bound electrons in the ion to the continuum as a function of time, and gives a measure of the relative population of the ionic species throughout the duration of the FEL pulse. The Ne^{2+} $2p^4$ (^{1}S) term is not included as it lies outside the measurement range of interest here. The above formula yields the peaks for the photoelectron spectrum (PES) at positions $\bar{\epsilon}_f = \bar{E}_i + \omega_F \pm \omega_L - \bar{E}_c$, with height and width determined by the quantities $\bar{\gamma}_g^{(FEL)}, \bar{\gamma}_i^{(IR)}(\theta_p)\, A_{\parallel}^{(C)}(\epsilon),\, A_{\perp}^{(C)}(\epsilon)$. The bar above the relevant quantities denotes that the values are evaluated at maximum peak intensity of the relevant fields. The expression for the total photoelectron spectrum is then obtained by a summation over all possible configurations of the continuum

and final states.

The terms $A_{\parallel}$ and $A_{\perp}$ contain the two photon transition matrix elements and their respective contributions to the total intensity to the individual photoelectron peaks. For a given core (either ^{3}P or ^{1}D), the value of A contains the contribution made to the photoelectron spectrum by all allowed two photon transitions, starting from an initial ground state, through the continuum state to a final state. Starting from a Ne^+ configuration, the allowed angular momenta of the outgoing electron is d or s, and by conventional selection rules the continuum electron have p or f symmetry. A sample expression, derived by Dr. Nikolopoulos, gives the relative strength of the sidebands for polarization angles $\theta_p = 0^0$ and $\theta_p = 90^o$ as:

$$\Delta S_C = A_{\parallel}^{(C)} - A_{\perp}^{(C)} \sim 25|A_{DF}^{(C)}|^2 + 7|A_{DP}^{(C)}|^2 + |5A_{SP}^{(C)} + 2A_{DP}^{(C)}|^2 > 0 \qquad (5.2)$$

where $A_{DF}^{(C)}, A_{DP}^{(C)}$ and $A_{SP}^{(C)}$ are the two-photon radial matrix elements from the singly charged ion Ne^+ to the final continuum sideband (SB) states associated with the C core.

5.5 Discussion

Solution of the time-dependent Schrodinger Equation (TDSE) results in good agreement with experiment. A complete framework in which a two colour, three photon ionization pathway leads to the production of multiple sidebands is presented. However, it was found that the modulation of the amplitude of the sidebands as a function of relative polarization angle can be adequately described by a two colour, two photon process i.e. one XUV photon to ionize the Ne^+ target, and, in this case, one additional photon to create a sideband. Examining closely the relative amplitudes of the sideband peaks as a function of polarization angle provides a potentially rich vein of insights into the underlying ionization processes. A semi-quantitative analysis of the partial wave contributions can be extracted from the plots given in Fig. 5.6. In this figure, the sideband yield is plotted as a function of the relative polarization angle displaying a clear, systematic variation. The plots for the sidebands have been normalised by making the theoretical and experimental signals at parallel polarization are equal.

As mentioned above (see Eqn. 5.1 and subsequent simplification), the amplitude of the sidebands as a function of polarization angle can be described by an expression of the form $\sigma(\theta) \propto A_{\parallel}\cos^2(\theta) + A_{\perp}\sin^2(\theta)$ in which $A_{\parallel}$ and $A_{\perp}$ are factors containing all partial wave contributions, and are proportional to the square of the respective *two photon* transition matrix elements. Some selected scenarios

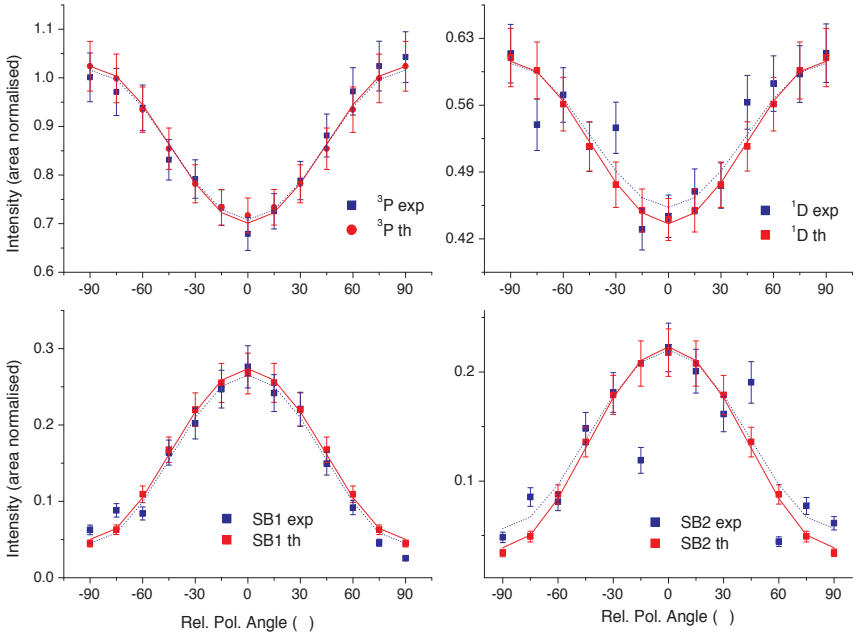

Figure 5.6: Variation of the amplitude of the photoelectron features as a function of the relative angle between the linear polarization vectors of the two laser fields. The experimental spectra have been normalized to the theory. The solid lines denote theoretical fits using the TDSE with 0° indicating parallel polarization (maximum attenuation of mainlines, maximum sideband signal), and ±90° denoting perpendicular alignment.

will be discussed in detail, but first the general trends are examined. The plots in Fig. 5.6 have been fitted with the general expression previously mentioned. The exact underlying ionization mechanisms are not so easy to extract directly from these kinetic energy spectra, but the relative contribution made to the sideband intensity by the parallel and perpendicular components can be extracted. On closer inspection of the second sideband, SB2 (bottom-right quadrant), it is straight forward to obtain the ratio $A_{\parallel}$ / $A_{\perp}$ 4.6_{exp} (6.4_{th}), along with values $A_{\parallel}$ - $A_{\perp}$ (which is proportional to the sum of all partial wave contributions) of 0.172_{exp} (0.186_{th}).

An additional value is given in the last entry of the Table 5.1 and Table 5.2. At an angle of 45°, the sideband consists of a mixture of parallel and perpendicular contributions. The electron yield is proportional to $\frac{1}{2}$ ($A_{\parallel}$ + $A_{\perp}$) . For SB1 value is obtained of 0.148_{exp} (0.137_{th}).

Examining the lineout of SB1 (bottom-left quadrant), which contains contributions from both photoelectron lines (and hence the outgoing electron experiences two separate ionic cores), parameters are obtained resulting in a ratio ($A_{\parallel}^{^1D}$ + $A_{\parallel}^{^3P}$) / ($A_{\perp}^{^1D}$ + $A_{\perp}^{^3P}$) of 4.4_{exp} (5.5_{th}) respectively. Furthermore, the values $A_{\parallel}$ - $A_{\perp}$ can be

Table 5.1: Compilation of parameters obtained from peak labelled SB2.

SB2		
	Exp	Theory
$A_{\parallel} - A_{\perp}$	.172	.186
$A_{\parallel}$ / $A_{\perp}$	4.6	6.4
$\frac{1}{2}$ ($A_{\parallel}$ + $A_{\perp}$)	.148	.137

Table 5.2: Compilation of obtained parameters from peak labelled SB1.

SB1		
	Exp	Theory
($A_{\parallel}^{1D}$ + $A_{\parallel}^{3P}$)- ($A_{\perp}^{1D}$ + $A_{\perp}^{3P}$)	.211	.224
$A_{\parallel}^{1D} + A_{\parallel}^{3P}/A_{\perp}^{1D} + A_{\perp}^{3P}$	4.4	5.5
$\frac{1}{2}$ ($A_{\parallel}^{1D}$ + $A_{\parallel}^{3P}$ + $A_{\perp}^{1D}$ + $A_{\perp}^{3P}$)	.164	.168

extracted, giving values of 0.221_{exp} (0.224_{th}). It can be deduced from the values of ($A_{\parallel}$ - $A_{\perp}$) that the makeup of SB1 and SB2, that is, the total signal as a result of all ϵs-ϵp, ϵd-ϵp and ϵd-ϵf waves, are fundamentally different.

A similar value for the cross section at an angle of 45° can be derived for SB1, however the expression is complicated somewhat by the contribution to the intensity by the two ionic cores. The electron yield at this angle is proportional to $\frac{1}{2}$ ($A_{\parallel}^{1D}$ + $A_{\parallel}^{3P}$ + $A_{\perp}^{1D}$ + $A_{\perp}^{3P}$) and is valued at 0.164_{exp} (0.168_{th}).

5.6 Conclusions

The response of Ne^{+} to intense XUV pulses at an energy of 46 eV has been investigated by photoelectron spectroscopy. Clear evidence of sequential two photon double ionization and subsequent above threshold ionization has been found. In addition, the relative intensities of the two-colour photoelectron lines as a function of the relative angle between the initial and dressing laser fields have been investigated. The monochromaticity of the XUV radiation from FLASH enabled the study of the ATI process free from disturbing interference processes. Good overall agreement is found between experiment and theoretical results, giving confidence that future studies can reveal yet more internal dynamics.

Similar to the 1s ionization of He, the intensities of the 2p lines of Ne and the corresponding sidebands depend strongly on the relative orientation between the linear polarization vectors of the ionizing FLASH radiation and of the NIR dressing field. Since the dressing field simply redistributes the photoelectrons among the photolines and the sidebands, both main photolines and sideband curves are

characterized by oscillations that are out of phase by 90°, i.e. minima in the sideband intensity correspond to maxima in the photoline intensity and vice versa. The amplitude of the intensity variation is determined by the relative partial cross sections in the two-photon ionization process. The measured polarization dependence of the sidebands arising from the sequential TPDI should therefore provide additional and complementary information on the angular distribution of the TDPI.

Further studies in the future will be aided by light sources that are increasingly tunable and whose parameters are readily changed. XUV laser systems in which the pulse width, wavelength and polarization are adjustable, in combination with a sufficiently intense optical laser, will allow the investigation of ionization and resonances excitation process that until now have been inaccessible in one photon experiments. The relative strengths and various relaxation pathways of such transitions is largely unknown, at least for those originating from inner shells. Moreover, the wavelength of both photon beams can be chosen to coincide with a doubly resonant excitation. The underlying physics for such doubly optically resonant processes can be found in such papers as [212, 213, 214], but only one experiment has been performed up to now [215].

Chapter 6

Summary

6.1 Summary of Thesis

The work presented in this thesis can be broadly labelled as an investigation of EUV light-matter interactions using photoelectron spectroscopy. The results can be further classified into two main categories. The first concernced the interaction of a tightly focused, ultrahigh intensity FEL beam with rare gas targets through the use of multilayer mirrors. The high energy EUV photons, coupled with the unprecendented photon flux facilitated multiphoton absorption by inner shell electrons in Xenon, Neon and Krypton. The second class of experiment saw the introduction of a second, IR laser and is mainly concerned with two colour ionization of a rare gas atom, in this case Neon. It is hoped that results presented contribute in some way toward understanding the physical interactions that take place in EUV conditions.

Chapter 3 was primarily concerned with the observation of multiphoton induced inner shell ionization events. In Xe, a signal was detected that was attributed to two photon ionization of a 4d electron. The relative one and two photon 4d partial cross sections were estimated experimentally and theoretically. A signal believed to be the result of two photon ionization of an inner valence 5s electron was identified on the basis of kinetic energy considerations, however further work is required to refine the signal. This may be permitted in the near future as it would be of much interest to the community to see the relative yield of the two photon 5s and 5p lines in comparison to the well known one photon yield. Chapter 3 also presented results for a neon target. In this case, signatures arising from direct, two photon ionization of a 2p and, interestingly, 2s electron were identified. Preliminary work on the interpretation of these signals has shown the rather drastic change in the ratio of 2s and 2p ionization yields for one and two photon ionization, as predicted by theory [216].

Results were presented in Chapter 4 in which, at a photon energy of 46 eV (26.9

nm), an inner 3d electron of Kr was promoted to a 4d orbital via a non-sequential two photon excitation pathway, creating a state that decays via an Auger transition. A signal resulting from the decay event was detected by electron spectroscopy, along with a number of other multiphoton processes, including two photon ionization of a 4p electron from both neutral and singly ionized Kr. As is Chapter 3, one of the key components of the experimental setup was a custom made multilayer mirror. By further focusing the incoming FEL beam, the unprecedented ultrahigh intensities required to drive an multiphoton inner shell transition were finally obtained. The result is a natural follow on from the first experiment in 1978, in which single photon, resonantly enhanced Auger decay in Kr and Xe were first studied with bright synchrotron radiation [162].

Finally, in Chapter 5, results were presented of a two-colour, above threshold photoionization experiment, in which an IR laser was synchronised to an FEL beam. This results in a modification of the one-photon (EUV only) photoelectron spectrum by the addition of sidebands positioned either side of the one-photon peak. By studying carefully the sidebands, the result of continuum-continuum transitions induced by the IR laser, it is possible to extract some of the parameters governing the photon-atom interaction. Unlike previous works, in which two-colour ionization of neutral atoms was studied [204, 217, 218], ATI of an ionic target was investigated here. With a Ne^+ $2p^5$ ion target, a greater number of ionization pathways exist (i.e. ionization leaving Ne^{2+} in 1D and 3P final states) in which the conditions $\Delta l = \pm 1$ and $\Delta m_l = 0$ are satisfied, leading to richer photoelectron spectra.

6.2 Future Directions

An interesting direction for future experiments may be in investigating double core hole states of atoms. Already in Chapters 3 and 4, results were presented in which single inner shell vacancies were created in Xe and Kr. Preliminary investigations by this author have resulted in what are believed to be signatures of double inner shell electron ejection. In the presence of this second 4d hole, the $N_{4,5}O_{2,3}O_{2,3}$ Auger lines may shift to slightly higher kinetic energies by an amount on the order of a few eV according to the (Z+1) model [219]. However, this three-electron correlation process is of higher order and should be of considerably lower probability.

The use of FELs in photoionization studies is still a relatively young field, and it is hoped that this work goes some way to making a contribution to it.

Appendix A

Two Photon Inner Shell Ionization of Xe at 46 eV

This short addition to the appendix serves to present an additional result to those already presented in Chapter 3. In a follow up experiment, a signal arising from the two photon ionization by ejection of an inner 5s electron was also recorded and is presented here, with a deeper interpretation of the spectrum the topic of a future work. The spectrum displayed in Fig.6.1 was taken at a photon energy of 46 eV. The

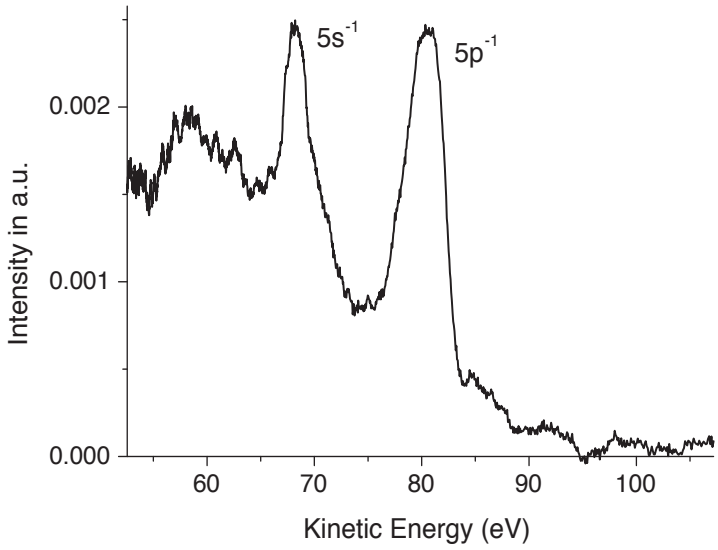

Figure 6.1: Photoelectron spectrum recorded at an FEL photon energy of 46 eV. The predominant peaks are due to two photon ionization of 5p and inner shell 5s electrons, respectively.

peaks are assigned labels only on the basis of kinetic energy considerations. Further work is required at a future beamtime to refine the signal as there is a significant background contribution. At present, it is not possible to extract the ratio of the 5s and 5p peaks, nor is it possible to confirm their intensity dependence.

Appendix B

Derivation of the TDSEs

The short appendix is written as an accompaniment to the theoretical model outlined in Chapter 5. The work is the basis of a future publication, and the text presented here was written almost entirely by Dr. Lampros Nikolopoulos. It is reproduced here with permission.

To start with, the initial state of the system $|g\rangle$ is defined as the Ne ground state $|g\rangle = |1s^2 2s^2 2p^6\, {}^1S_0\rangle$ in the presence of FEL and IR laser fields. The other states involved in the process are the singly charged Ne^+ ground state (including the ejected electron with asymptotic momentum $\mathbf{k}_i$, $|1s^2 2s^2 2p^5, {}^2P; \mathbf{k}_i m_{s_i}\rangle$) and the doubly charged Ne^{2+} ion with an associated electron ejected with asymptotic momenta $\mathbf{k}_i, \mathbf{k}_f$ and spins $m_{s_i} m_{s_f}$, respectively. These states are denoted as $|1s^2 2s^2 2p^4, {}^{S_c}L_c; \mathbf{k}_f m_{s_f}; \mathbf{k}_i m_s$ and $|1s^2 2s^2 2p^4, {}^{S_c}L_c; \mathbf{k}_f m_{s_f}; \mathbf{k}_i m_{s_i}\rangle$, where ${}^{S_c}L_c = {}^1D, {}^3P$ the spin and angular momenta of the doubly ionized Ne^{2+}ions.

Thus the time-dependent state vector of the wavefunction is

$$|\psi(t)\rangle = U_g(t)|g\rangle + U_{i,k_i}(t)\,|i;k_i\rangle + \sum_c \int dk_c U_{c,k_c k_i,}(t)\,|c;k_c k_i\rangle$$

$$+ \textstyle\sum_c \int dk_f U_{c,k_f,k_i}(t)\,|f;k_f k_i\rangle, \tag{6.1}$$

The quantities of interest here are the amplitudes $U_x(t),\ \ x = (c,k_c), (c,k_f)$, the calculation of which gives the complete information of the final state of the system. The Hamiltonian for the system is defined as $H = H_0 + D^{(F)} + D^{(L)}(\theta_p)$ with H_0 the field-free Hamiltonian of Ne. The time-dependent wavefunction $|\psi(t)\rangle$ is defined by the corresponding TDSE $(i\partial/\partial t - H)|\psi(t)\rangle = 0$. Through well-established techniques, the details of which will not presented here, we can obtain the differential equations obeyed by the time-dependent amplitudes $U_{c,k_c}(t)$ and $U_{c,k_f}(t)$ [211]. Since the desired spectrum is the angle-integrated photoelectron energy spectrum (PES) of the singly ionized Ne^+, one must integrate over all variables of the elec-

tron ejected from the ionization of the neutral Ne and all angular variables of the electron ejected from the singly charged ion Ne^+.

By taking into consideration the above mentioned approximations one ends up with differential equations in terms of amplitudes $u_c(t)$ and $u_f^{(C)}(t)$. In the present case, where two doubly ionized residual ions ($Ne^{2+1}D,^3P$) can be reached in the second step of the sequential path the amplitude equations are as follows:

$$
\begin{aligned}
i\dot{u}_g(t) &= (\bar{E}_g - i\frac{\gamma_g^{(F)}(t)}{2})\, u_g(t), \\
i\dot{u}_i(t) &= (\bar{E}_i - i\frac{\gamma_i^{(F)}(t)}{2})\, u_i(t) + D_{ig}^{(F)}(t)\, u_g(t), \\
i\dot{u}_c(t) &= (\bar{E}_c - i\frac{\gamma_c^{(L)}(\theta_p,t)}{2})\, u_c(t) + D_{ci}^{(F)}(t)\, u_i(t)
\end{aligned}
$$

$$
i\dot{u}_f^{(c)}(t) = \bar{E}_f\, u_f^{(c)}(t) + D_{fc}^{(L)}(\theta_p,t)\, u_c(t) \tag{6.2}
$$

with $D^{(F)}(t) = -\mathbf{E}_F(t)\cdot\mathbf{r}$, $D^{(L)}(\theta_p,t) = -\mathbf{E_L}(t)\cdot\mathbf{r}$ the electric dipole operators for the FEL and IR fields, respectively. The indices c, f should be understood as $|c\rangle = |C;\epsilon_c l_c m_{l_c}\rangle$ and $|f\rangle = |C;\epsilon_f l_f m_{l_f}\rangle$, where $|C\rangle = |L_c S_c M_{L_c} M_{S_c}\rangle$ refers to the magnetic and spin quantum numbers of the doubly ionized core states and $|\epsilon_k l_k m_{l_k}\rangle,\ k = c, f$ being the energy and angular quantum numbers of the ejected electron from the singly charged ion Ne^+. Hence we describe, as required, the physical situation of electrons being ejected with quantum numbers ϵ_c, l_c, m_{l_c} and ϵ_f, l_f, m_{l_f} respectively with the remaining ions in the states $C = {}^1$D, ^{3}P. Note that in the present case, based on dipole selection rules the possible one-electron angular quantum numbers values are $l_c = 0, 2$ and $l_f = 1, 3$. The spin quantum number of the electron is assumed fixed, so we suppress it in the formulation. The final results, however, take into account the sum over the spin projection quantum numbers $m_s = \pm 1/2$.

Finally, the detunings are defined as $\bar{E}_c = \epsilon_c + \bar{E}_c - (\bar{E}_i + \omega_F)$ and $\bar{E}_f = \epsilon_f + \bar{E}_c - (\bar{E}_i + \omega_F \pm \omega_L)$ with ϵ_c and ϵ_f being the kinetic energies of the ejected electrons associated with the final continua reached by the sequential path through Ne^+. $\bar{E}_g = E_g + S_g^{(F)}$, $\bar{E}_i = E_i + S_i^{(F)}$ are the ground states energies of the neutral and singly charged Neon, respectively, while $\bar{E}_c = E_c + S_c^{(L)}$. $S_g^{(F)}, S_i^{(F)}$ are the AC-Stark shifts of the ground states due to interaction with the FEL field while $S_c^{(L)}$ is the ponderomotive potential of the ejected electron. The ionization widths $\gamma_g^{(F)}, \gamma_i^{(F)}, \gamma_c^{(L)}$ into the final continua (as labelled by the subscripts) are given by

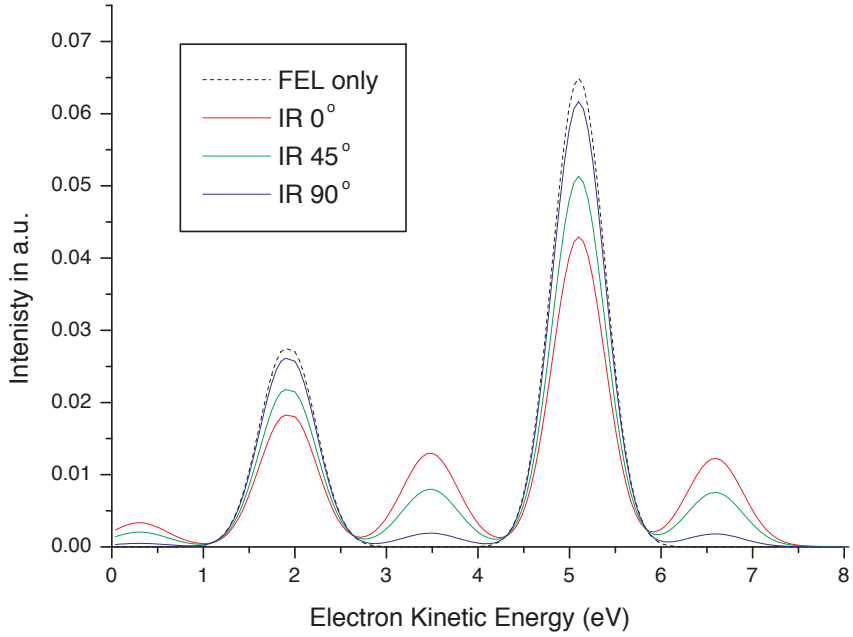

Figure 6.2: Theoretical spectra generated from equations Eq.2 and Eq.3. Shown here are spectra for only a selection of polarisation angles for clarity.

$$
\begin{aligned}
\gamma_g^{(F)}(t) &= 2\pi |D_{gi}^{(F)}(t)|^2 \delta(\epsilon_i = (\bar{E}_g + \omega_F) - \bar{E}_i), \\
\gamma_i^{(F)}(t) &= 2\pi \sum_C \sum_{l_c m_{l_c}} |D_{i;\epsilon_c l_c m_c}^{(F)}(t)|^2 \delta(\epsilon_c = (\bar{E}_i + \omega_F) - \bar{E}_c), \\
\gamma_c^{(L)}(\theta_p, t) &= 2\pi \sum_{l_f m_{l_f}} |D_{\epsilon_c l_c m_{l_c}; \epsilon_f l_f m_{l_f}}^{(L)}(\theta_p, t)|^2 [\delta(\epsilon_f = \epsilon_c + \omega_L) + \delta(\epsilon_f = \epsilon_c - \omega_L)].
\end{aligned}
$$

Solving the above system of equations in time with the appropriate temporal pulse shapes (in this case, Gaussian temporal profiles are used), we can calculate the PES, at the end of the pulse, associated with the various continua. The total PES is then obtained by summing over the final states the electron $|f\rangle$:

$$
S(\theta_p) \sim \sum_C \sum_{l_f m_{l_f}} \left| \sum_{l_c m_{l_c}} u_f^{(c)}(t \to \infty) \right|^2 \tag{6.3}
$$

Some sample spectra are provided in Fig. 1 at only a select few polarisation angles.

Bibliography

[1] J. Andruszkow, B. Aune, V. Ayvazyan, N. Baboi, R. Bakker, V. Balakin, D. Barni, A. Bazhan, M. Bernard, A. Bosotti, J.C. Bourdon, W. Brefeld, R. Brinkmann, S. Buhler, J.-P. Carneiro, M. Castellano, P. Castro, L. Catani, S. Chel, Y. Cho, S. Choroba, E. R. Colby, W. Decking, P. Den Hartog, M. Desmons, M. Dohlus, and D. Edwards. First Observation of Self-Amplified Spontaneous Emission in a Free-Electron Laser at 109 nm Wavelength. *Phys. Rev. Lett.*, 85(18):3825–3829, Oct 2000.

[2] V. Ayvazyan, N. Baboi, I. Bohnet, R. Brinkmann, M. Castellano, P. Castro, L. Catani, S. Choroba, A. Cianchi, M. Dohlus, H. T. Edwards, B. Faatz, A. A. Fateev, J. Feldhaus, K. Flöttmann, A. Gamp, T. Garvey, H. Genz, Ch. Gerth, V. Gretchko, B. Grigoryan, U. Hahn, C. Hessler, K. Honkavaara, M. Hüning, R. Ischebeck, and M. Jablonka. Generation of GW Radiation Pulses from a VUV Free-Electron Laser Operating in the Femtosecond Regime. *Phys. Rev. Lett.*, 88(10):104802, Feb 2002.

[3] W. Ackermann, G. Asova, V. Ayvazyan, A. Azima, N. Baboi, J. Bähr, V. Balandin, B. Beutner, A. Brandt, A. Bolzmann, et al. Operation of a Free-Electron Laser From the Extreme Ultraviolet to the Water Window. *Nature Photonics*, 1(6):336–342, 2007.

[4] R. Pantell, G. Soncini, and H. Puthoff. Stimulated Photon-Electron Scattering. *IEEE Journal of Quantum Electronics*, 4(11):905–907, 1968.

[5] J.M.J. Madey. Stimulated Emission of Bremsstrahlung in a Periodic Magnetic Field. *Journal of Applied Physics*, 42:1906, 1971.

[6] Luis R. Elias, William M. Fairbank, John M. J. Madey, H. Alan Schwettman, and Todd I. Smith. Observation of Stimulated Emission of Radiation by Relativistic Electrons in a Spatially Periodic Transverse Magnetic Field. *Phys. Rev. Lett.*, 36(13):717–720, Mar 1976.

[7] D.A.G. Deacon, L.R. Elias, J.M.J. Madey, G.J. Ramian, H.A. Schwettman, and T.I. Smith. First Operation of a Free-Electron Laser. *Physical Review Letters*, 38(16):892–894, 1977.

[8] N.M. Kroll and W.A. McMullin. Stimulated Emission from Relativistic Electrons Passing Through a Spatially Periodic Transverse Magnetic Field. *Physical Review A*, 17(1):300–308, 1978.

[9] A.M. Kondratenko and E.L. Saldin. Generation of Coherent Radiation by a Relativistic Electron Beam in an Undulator. *Sov. Phys. Dokl.*, 24(12):986, 1979.

[10] A.M. Kondratenko and E.L. Saldin. Generation of Coherent Radiation by a Relativistic Electron Beam in an Undulator. *Part. Accelerators*, 10:207, 1980.

[11] R. Bonifacio, C. Pellegrini, and L.M. Narducci. Collective Instabilities and High-gain Regime in a Free Electron Laser. *Optics Communications*, 50(6):373–378, 1984.

[12] R. Bonifacio, F. Casagrande, and L. De Salvo Souza. Collective Variable Description of a Free-Electron Laser. *Physical Review A*, 33(4):2836–2839, 1986.

[13] Kwang-Je Kim. Three-Dimensional Analysis of Coherent Amplification and Self-Amplified Spontaneous Emission in Free-Electron Lasers. *Phys. Rev. Lett.*, 57(15):1871–1874, Oct 1986.

[14] Y.S. Derbenev, AM Kondratenko, and E.L. Saldin. On the Possibility of Using a Free Electron Laser for Polarization of Electrons in Storage Rings. *Nuclear Instruments and Methods in Physics Research*, 193(3):415–421, 1982.

[15] J.B. Murphy and C. Pellegrini. Free Electron Lasers for the XUV Spectral Region. *Nuclear Instruments and Methods in Physics Research Section A: Accelerators, Spectrometers, Detectors and Associated Equipment*, 237(1-2):159–167, 1985.

[16] C. Pellegrini. A 4 to 0.1 nm FEL Based on the SLAC Linac. *Proceedings of the Workshop on Fourth Generation Light Sources, SSRL-SLAC report*, page 365, 1992.

[17] MJ Hogan, C. Pellegrini, J. Rosenzweig, S. Anderson, P. Frigola, A. Tremaine, C. Fortgang, D.C. Nguyen, R.L. Sheffield, J. Kinross-Wright, et al. Measurements of Gain Larger than 10^5 at 12 μm in a Self-Amplified Spontaneous-Emission Free-Electron Laser. *Physical Review Letters*, 81(22):4867–4870, 1998.

[18] S.V. Milton, E. Gluskin, N.D. Arnold, C. Benson, W. Berg, S.G. Biedron, M. Borland, Y.C. Chae, R.J. Dejus, P.K. Den Hartog, et al. Exponential Gain and Saturation of a Self-Amplified Spontaneous Emission Free-Electron Laser. *Science*, 292(5524):2037, 2001.

[19] A. Tremaine, P. Frigola, A. Murokh, C. Pellegrini, S. Reiche, J. Rosenzweig, M. Babzien, I. Ben-Zvi, E. Johnson, R. Malone, et al. Characterization of an 800 nm SASE FEL at Saturation. *Nuclear Instruments and Methods in Physics Research Section A: Accelerators, Spectrometers, Detectors and Associated Equipment*, 483(1-2):24–28, 2002.

[20] V. Ayvazyan, N. Baboi, I. Bohnet, R. Brinkmann, M. Castellano, P. Castro, L. Catani, S. Choroba, A. Cianchi, M. Dohlus, et al. A New Powerful Source for Coherent VUV Radiation: Demonstration of Exponential Growth and Saturation at the TTF Free-Electron Laser. *The European Physical Journal D-Atomic, Molecular, Optical and Plasma Physics*, 20(1):149–156, 2002.

[21] V. Ayvazyan, N. Baboi, J. Bahr, V. Balandin, B. Beutner, A. Brandt, I. Bohnet, A. Bolzmann, R. Brinkmann, O.I. Brovko, et al. First Operation of a Free-Electron Laser Generating GW Power Radiation at 32 nm Wavelength. *The European Physical Journal D*, 37(2):297–303, 2005.

[22] M. Castellano, V. Verzilov, L. Catani, A. Cianchi, and G. Orlandi. Bunch Length Measurements at TTF Using Coherent Diffraction Radiation. In *Proc. 7th EPAC, Vienna*, page 1699, 2000.

[23] M. Geitz, S. Schreiber, G. Von Walter, D. Sertore, M. Bernard, and B. Leblond. Determination of the Longitudinal Phase Space Distribution produced with TTF Photo Injector. In *Proc. of the 21st Int. Free Electron Laser Conf*, 1999.

[24] F. Stulle. A Bunch Compressor for Small Emittances and High Peak Currents at the VUV Free-Electron Laser. 2004.

[25] M. Dohlus, T. Limberg, and P. Emma. Bunch Compression for Linac-based FELs. *ICFA Beam Dynamics Newsletter*, 38.

[26] W. Decking, G.H. Hoffstätter, and T. Limberg. *Bunch Compressor for the TESLA Linear Collider*. Dt. Elektronen-Synchrotron DESY, MHF-SL Group, 2001.

[27] D.T. Attwood. *Soft X-rays and Extreme Ultraviolet Radiation: Principles and Applications*. Cambridge Univ. Press, 1st Edition, 2000.

[28] K. Tiedtke, A. Azima, N. Bargen, L. Bittner, S. Bonfigt, S. Düsterer, B. Faatz, U. Frühling, M. Gensch, C. Gerth, et al. The Soft X-ray Free-Electron Laser

FLASH at DESY: Beamlines, Diagnostics and End-Stations. *New Journal of Physics*, 11:023029, 2009.

[29] A.A. Sorokin, S.V. Bobashev, T. Feigl, K. Tiedtke, H. Wabnitz, and M. Richter. Photoelectric Effect at Ultrahigh Intensities. *Physical Review Letters*, 99(21):213002, 2007.

[30] J. Feldhaus, J. Arthur, and J.B. Hastings. X-ray Free-Electron Lasers. *Journal of Physics B: Atomic, Molecular and Optical Physics*, 38:S799, 2005.

[31] H. Hertz. Uber Einen Einfluss des Ultravioletten Lichtes auf die Electrische Entladung. *Annalen der Physik*, 31(8):983–1000, 1887.

[32] B. Tsai, T. Baer, and M.L. Horovitz. A Time-of-Flight Detection System for Near Threshold Photoelectron Spectroscopy. *Review of Scientific Instruments*, 45(4):494–498, 1974.

[33] R.Z. Bachrach, F.C. Brown, and S.B.M. Hagstrom. Photoelectron Spectroscopy by Time-of-Flight Technique Using Synchrotron Radiation. *Journal of Vacuum Science and Technology*, 12(1):309–312, 1975.

[34] MG White, R.A. Rosenberg, G. Gabor, E.D. Poliakoff, G. Thornton, S.H. Southworth, and D.A. Shirley. Time-of-flight Photoelectron Spectroscopy of Gases Using Synchrotron Radiation. *Review of Scientific Instruments*, 50(10):1268–1273, 1979.

[35] Edward M. Purcell. The Focusing of Charged Particles by a Spherical Condenser. *Phys. Rev.*, 54(10):818–826, Nov 1938.

[36] W. Mehlhorn. Die Feinstruktur des L-MM-Auger-Elektronenspektrums von Argon und der K-LL-Spektren von Stickstoff, Sauerstoff und Methan. *Zeitschrift für Physik A Hadrons and Nuclei*, 160(3):247–267, 1960.

[37] D.W. Turner and M.I. Al Jobory. Determination of Ionization Potentials by Photoelectron Energy Measurement. *The Journal of Chemical Physics*, 37:3007, 1962.

[38] Manfred O. Krause. Determination of L Binding Energies of Krypton by the Photoelectron Method. *Phys. Rev.*, 140(6A):A1845–A1849, Dec 1965.

[39] D.R. Bates. Calculations of the Cross-Section of Neutral Atoms and Positive and Negative Ions Towards the Absorption of Radiation in the Continuum. *Monthly Notices of the Royal Astronomical Society*, 106:432, 1946.

[40] H.A. Bethe and E.E. Salpeter. Quantum Mechanics of One-and Two-Electron Atoms. 1957.

[41] H.A. Bethe. Handbuch der Physik Vol. 24/1. *Julius Springer, Berlin*, 1933.

[42] J. Cooper and R.N. Zare. Angular Distribution of Photoelectrons. *Journal of Chemical Physics*, 48:942–943, 1968.

[43] VUV and Soft X-Ray Photoionization. *edited by U. Becker and D. A. Shirley*. Plenum Press, First Edition, New York, 1996.

[44] D.R. Hartree. The Calculation of Atomic Structures. Wiley, New York,1957.

[45] P. Pines, D. Nozieres. The Theory of Quantum Liquids, Benjamin, New York, 1966.

[46] M. Ya. Amusia. Atomic Photoeffect, New York: Plenum, 1990.

[47] G.C. King, F.H. Read, and R.C. Bradford. Structure Near Autoionizing Energies in the Excitation of Bound States of Helium, Neon and Argon by Electron Impact. *Journal of Physics B: Atomic and Molecular Physics*, 8:2210, 1975.

[48] R.B. Barker and H.W. Berry. Electron Energy Distributions From Ionizing Collisions of Helium and Neon Ions with Helium. *Physical Review*, 151(1):14–19, 1966.

[49] S. Ohtani, H. Nishimura, H. Suzuki, and K. Wakiya. Auger-Electron Ejections from Xenon $N_{4,5}OO$ and Krypton $M_{4,5}NN$ Processes by Electron Impact near Threshold. *Phys. Rev. Lett.*, 36(15):863–866, Apr 1976.

[50] A.F. Starace and S.T. Manson. Fundamental Aspects of Atomic Photoionization with High-Brightness Light Sources. *VUV and Soft X-Ray Photoionization*, 1996.

[51] D.L. Ederer. Photoionization of the 4d Electrons in Xenon. *Physical Review Letters*, 13(25):760–762, 1964.

[52] B. Sonntag and P. Zimmermann. XUV Spectroscopy of Metal Atoms. *Reports on Progress in Physics*, 55:911, 1992.

[53] V. Schmidt. Photoionization of Atoms Using Synchrotron Radiation. *Reports on Progress in Physics*, 55:1483, 1992.

[54] K. Codling and R. P. Madden. Optically Observed Inner Shell Electron Excitation in Neutral Kr And Xe. *Phys. Rev. Lett.*, 12(4):106–108, Jan 1964.

[55] W.R.S. Garton and J.P. Connerade. Absorption Spectra of Zn I, Cd I, and Hg I in the Vacuum Ultraviolet. *The Astrophysical Journal*, 155:667, 1969.

[56] J.P. Connerade and M.W.D. Mansfield. Structure in the Hg I Absorption Spectrum from 20 to 120 Å Associated with the Excitation of the 4f and 5s Subshells. *Proceedings of the Royal Society of London. Series A, Mathematical and Physical Sciences*, 335(1600):87–96, 1973.

[57] M.W.D. Mansfield and J.P. Connerade. The Absorption Spectrum of Sr I between 40 and 95 Angstrom. *Proceedings of the Royal Society of London. A. Mathematical and Physical Sciences*, 342(1630):421, 1975.

[58] J.P. Connerade, B. Drerup, and M.W.D. Mansfield. Potential Barrier Effects Beyond the 4f Photoionization Thresholds in Pb I. *Proceedings of the Royal Society of London. Series A, Mathematical and Physical Sciences*, 348(1653):235–238, 1976.

[59] J.P. Connerade and M.W.D. Mansfield. Potential Barrier Minimum and Delayed Onset of Continuous Absorption Beyond the 3d Limit in Kr I. *Proceedings of the Royal Society of London. Series A, Mathematical and Physical Sciences*, 343(1634):415–419, 1975.

[60] T.B. Lucatorto and T.J. McIlrath. Efficient Laser Production of a Na^+ Ground-State Plasma Column: Absorption Spectroscopy and Photoionization Measurement of Na^+. *Physical Review Letters*, 37(7):428–431, 1976.

[61] J.M. Bizau, D. Cubaynes, M. Richter, F.J. Wuilleumier, J. Obert, J.C. Putaux, T.J. Morgan, E. Kallne, S. Sorensen, and A. Damany. First Observation of Photoelectron Spectra Emitted in the Photoionization of a Singly Charged Ion Beam with Synchrotron Radiation. *Physical Review Letters*, 67(5):576–579, 1991.

[62] B. Peart and K. Dolder. Measurements of Cross Sections for Inner and Outer-shell Ionization of Rb^+, Cs^+, Ca^+ and Sr^+ ions by electron impact. *Journal of Physics B: Atomic and Molecular Physics*, 8:56, 1975.

[63] I.C. Lyon, B. Peart, J.B. West, and K. Dolder. Measurements of Absolute Cross Sections for the Photoionisation of Ba^+ Ions. *Journal of Physics B: Atomic and Molecular Physics*, 19:4137, 1986.

[64] I.C. Lyon, B. Peart, K. Dolder, and J.B. West. Measurements of Absolute Photoionisation Cross Sections of Ca^+ Ions. *Journal of Physics B: Atomic and Molecular Physics*, 20:1471, 1987.

[65] I.C. Lyon, B. Peart, and K. Dolder. Measurements of Absolute Photoionisation Cross Sections of Sr^+ Ions. *Journal of Physics B: Atomic and Molecular Physics*, 20:1925, 1987.

[66] J. M. Bizau, C. Blancard, D. Cubaynes, F. Folkmann, D. Kilbane, G. Faussurier, H. Luna, J. L. Lemaire, J. Blieck, and F. J. Wuilleumier. Experimental and Theoretical Studies of the Photoionization Cross Section of Fe^{4+} . *Phys. Rev. A*, 73(2):020707, Feb 2006.

[67] R. Thissen, J. M. Bizau, C. Blancard, M. Coreno, C. Dehon, P. Franceschi, A. Giuliani, J. Lemaire, and C. Nicolas. Photoionization Cross Section of Xe^+ Ion in the Pure $5p^5\ ^2P_{3/2}$ Ground Level. *Phys. Rev. Lett.*, 100(22):223001, Jun 2008.

[68] J. M. Bizau, C. Blancard, D. Cubaynes, F. Folkmann, J. P. Champeaux, J. L. Lemaire, and F. J. Wuilleumier. Absolute Photoionization Cross Sections Along the Xe Isonuclear Sequence: Xe^{3+} to Xe^{6+}. *Phys. Rev. A*, 73(2):022718, Feb 2006.

[69] J.-M. Bizau, J.-P. Mosnier, E. T. Kennedy, D. Cubaynes, F. J. Wuilleumier, C. Blancard, J.-P. Champeaux, and F. Folkmann. Photoionization of the Ne-like Si^{4+} Ion in Ground and Metastable States in the 110–184-eV Photon Energy Range. *Phys. Rev. A*, 79(3):033407, Mar 2009.

[70] A. Müller, S. Schippers, R.A. Phaneuf, S.W.J. Scully, A. Aguilar, A.M. Covington, I. Álvarez, C. Cisneros, E.D. Emmons, M.F. Gharaibeh, et al. K-Shell Photoionization of Ground-State Li-like Carbon Ions [C^{3+}]: Experiment, Theory and Comparison with Time-Reversed Photorecombination. *Journal of Physics B: Atomic, Molecular and Optical Physics*, 42:235602, 2009.

[71] A.M. Covington, A. Aguilar, I.R. Covington, G. Hinojosa, C.A. Shirley, R.A. Phaneuf, I. Álvarez, C. Cisneros, I. Dominguez-Lopez, M.M. Sant'Anna, et al. Valence-Shell Photoionization of the C-like Ion Ar+: Experiment and Theory. In *Journal of Physics: Conference Series*, volume 194, page 022083. IOP Publishing, 2009.

[72] J.E. Hansen, H. Kjeldsen, F. Folkmann, M. Martins, and J.B. West. Absolute Photoionization Cross Sections of the Ions $Ca^+ 4 - Ni4^+$. *Journal of Physics B: Atomic, Molecular and Optical Physics*, 40:293, 2007.

[73] T. Koizumi, Y. Itoh, M. Sano, M. Kimura, TM Kojima, S. Kravis, A. Matsumoto, M. Oura, T. Sekioka, and Y. Awaya. Photoionization of Ba^+ Ions

Due to Creation of 4d Hole States. *Journal of Physics B: Atomic, Molecular and Optical Physics*, 28:609, 1995.

[74] Y. Itoh, T. Koizumi, Y. Awaya, S.D. Kravis, M. Oura, M. Sano, T. Sekioka, and F. Koike. The 3d-Excited States of Sr^+ Ions Studied by Photoion-Yield Measurements. *Journal of Physics B: Atomic, Molecular and Optical Physics*, 28:4733, 1995.

[75] P. Auger. The Effect of a Photoelectric Compound. *Journal De Physique Et Le Radium*, 6:205–U12, 1925.

[76] J.B. West. Photoionization of Atomic Ions. *Journal of Physics B: Atomic, Molecular and Optical Physics*, 34:R45, 2001.

[77] A.P. Lukirskii, I.A. Brytov, and T.M. Zimkina. Photoionization Absorption of He, Kr, Xe, CH_4, and Methylal in the 23.6-250 Å Region. *Optics and Spectroscopy*, 17:234, 1964.

[78] M.G. Mayer. Rare-Earth and Transuranic Elements. *Physical Review*, 60(3):184–187, 1941.

[79] U. Fano and J.W. Cooper. Spectral Distribution of Atomic Oscillator Strengths. *Reviews Of Modern Physics*, 40(3):441–507, 1968.

[80] M. Ya. Amusia and N.A. Cherepkov. *Case Studies in Atomic Physics*, 5(2):47, 1975.

[81] T. B. Lucatorto, T. J. McIlrath, J. Sugar, and S. M. Younger. Radical Redistribution of the $4d$ Oscillator Strength Observed in the Photoabsorption of the Ba, Ba^+, and Ba^{++} Sequence. *Phys. Rev. Lett.*, 47(16):1124–1128, Oct 1981.

[82] C. McGuinness, G. O'Sullivan, P.K. Carroll, D. Audley, and M.W.D. Mansfield. 3d Absorption Spectra of Sr I Through Sr IV. *Phys. Rev. A*, 51(3):2053–2062, Mar 1995.

[83] M. Richter, M. Meyer, M. Pahler, T. Prescher, E.V. Raven, B. Sonntag, and H.E. Wetzel. Experimental Study of Atomic 4d Giant Resonances by Photoabsorption and Photoelectron Spectroscopy: Ba, La, and Ce. *Phys. Rev. A*, 39(11):5666–5675, Jun 1989.

[84] M. Richter, M. Meyer, M. Pahler, T. Prescher, E. v. Raven, B. Sonntag, and H.-E. Wetzel. Experimental study of atomic 4d giant resonances by photoabsorption and photoelectron spectroscopy: Sm, eu, and gd. *Phys. Rev. A*, 40(12):7007–7019, Dec 1989.

[85] G. Kutluk, H. Ishijima, M. Kanno, T. Nagata, and A.T. Domondon. A Systematic Study of Photoionization of Free Lanthanide Atoms in the 4d Giant Resonance Region. *Journal of Electron Spectroscopy and Related Phenomena*, 169(2-3):67–79, 2009.

[86] M.Y. Amusia and J.P. Connerade. The theory of Collective Motion Probed by Light. *Reports on Progress in Physics*, 63:41–70, 2000.

[87] M. Ya. Amusia, N.A. Cherepkov and L.V. Chernysheva. *Sov. Phys. JETP*, 33:90, 1971.

[88] G. O'Sullivan. Charge-Dependent Wavefunction Collapse in Ionised Xenon. *Journal of Physics B: Atomic and Molecular Physics*, 15:L765, 1982.

[89] J. P. Connerade and M. W. D. Mansfield. Term-Dependent Hybridization of the $5f$ Wave Functions of Ba and Ba^{++}. *Phys. Rev. Lett.*, 48(3):131–134, Jan 1982.

[90] J. Blackburn, P.K. Carroll, J. Costello, and G. OSullivan. Spectra of Xe VII, VIII, and IX in the Extreme Ultraviolet: 4d-mp, nf Transitions. *JOSA*, 73(10):1325–1329, 1983.

[91] W.T. Hill III, K.T. Cheng, W.R. Johnson, T.B. Lucatorto, T.J. McIlrath, and J. Sugar. Influence of Increasing Nuclear Charge on the Rydberg Spectra of Xe, Cs^+, and Ba^{++}: Correlation, Term Dependence, and Autoionization. *Physical Review Letters*, 49(22):1631–1635, 1982.

[92] J.E. Hansen, J. Brilly, E.T. Kennedy, and G. O'Sullivan. Rise and Fall of the $4d^{10} \rightarrow 4d^9$4f Resonance in the Xe Isoelectronic Sequence. *Phys. Rev. Lett.*, 63(18):1934–1937, Oct 1989.

[93] M. Göppert-Mayer. Uber Elementarakte mit Zwei Quantensprüngen. *Annalen der Physik*, 401(3):273–294, 1931.

[94] H. Barry Bebb. Quantitative Theory of the Two-Photon Ionization of the Alkali Atoms. *Phys. Rev.*, 149(1):25–32, Sep 1966.

[95] H. Barry Bebb and Albert Gold. Multiphoton Ionization of Hydrogen and Rare-Gas Atoms. *Phys. Rev.*, 143(1):1–24, Mar 1966.

[96] P. Koval. *Two-Photon Ionization of Atomic Inner-Shells*. Doctoral Thesis, University of Kassel, Germany, 2004.

[97] C.J. Foot. *Atomic Physics*. Oxford University Press, USA, 2005.

[98] B.H. Bransden and C.J. Joachain. *Physics of Atoms and Molecules*. Pearson Education, 2003.

[99] L.V. Keldysh. Ionization in the Field of a Strong Electromagnetic Wave. *Soviet Physics JETP*, 20(5):1307–1314, 1965.

[100] P. Radcliffe, S. Düsterer, A. Azima, W.B. Li, E. Plönjes, H. Redlin, J. Feldhaus, P. Nicolosi, L. Poletto, J. Dardis, et al. An experiment for Two-Color Photoionization Using High Intensity Extreme-UV Free Electron and Near-IR Laser Pulses. *Nuclear Inst. and Methods in Physics Research, A*, 583(2-3):516–525, 2007.

[101] K. Tiedtke, J. Feldhaus, U. Hahn, U. Jastrow, T. Nunez, T. Tschentscher, SV Bobashev, A.A. Sorokin, JB Hastings, S. Möller, et al. Gas Detectors for X-ray Lasers. *Journal of Applied Physics*, 103:094511, 2008.

[102] M. Richter, A. Gottwald, U. Kroth, A.A. Sorokin, S.V. Bobashev, L.A. Shmaenok, J. Feldhaus, C. Gerth, B. Steeg, K. Tiedtke, et al. Measurement of Gigawatt Radiation Pulses from a Vacuum and Extreme Ultraviolet Free-Electron Laser. *Applied Physics Letters*, 83:2970, 2003.

[103] A.A. Sorokin, A. Gottwald, A. Hoehl, U. Kroth, H. Schöppe, G. Ulm, M. Richter, SV Bobashev, I.V. Domracheva, D.N. Smirnov, et al. Method Based on Atomic Photoionization for Spot-Size Measurement on Focused Soft X-ray Free-Electron Laser Beams. *Applied Physics Letters*, 89:221114, 2006.

[104] A.M. Rijs, E.H.G. Backus, C.A. de Lange, N.P.C. Westwood, and M.H.M. Janssen. Magnetic Bottle Spectrometer as a Versatile Tool for Laser Photoelectron Spectroscopy. *Journal of Electron Spectroscopy and Related Phenomena*, 112(1-3):151–162, 2000.

[105] J.H.D. Eland, O. Vieuxmaire, T. Kinugawa, P. Lablanquie, RI Hall, and F. Penent. Complete Two-Electron Spectra in Double Photoionization: The Rare Gases Ar, Kr, and Xe. *Physical Review Letters*, 90(5):53003, 2003.

[106] S. Dusterer, P. Radcliffe, G. Geloni, U. Jastrow, M. Kuhlmann, E. Plonjes, K. Tiedtke, R. Treusch, J. Feldhaus, and P. Nicolosi. Spectroscopic Characterization of Vacuum Ultraviolet Free Electron Laser Pulses. *Optics letters*, 31(11):1750, 2006.

[107] M. Vidal-Dasilva, M. Fernández-Perea, J.I. Larruquert, J.A. Méndez, and J.A. Aznárez. Narrowband Multilayer Mirrors for the Extreme Ultraviolet Spectral Range of 50 to 95 nm. In *Proceedings of SPIE*, volume 7448, page 74480N, 2009.

[108] T. Feigl, S. Yulin, N. Benoit, and N. Kaiser. EUV Multilayer Optics. *Microelectronic Engineering*, 83(4-9):703–706, 2006.

[109] K.M. Skulina, C.S. Alford, R.M. Bionta, D.M. Makowiecki, E.M. Gullikson, R. Soufli, J.B. Kortright, and J.H. Underwood. Molybdenum/ Beryllium Multilayer Mirrors for Normal Incidence in the Extreme Ultraviolet. *Applied Optics*, 34(19):3727–3730, 1995.

[110] http://henke.lbl.gov/opticalconstants/multi2.html.

[111] Ray Tracing performed using the ZEEMAX suite of codes by Dr. Stefan Duesterer, DESY, and Dr. Torsten Feigel, Fraunhofer Institute, Jena.

[112] J. Dardis. Interactions of Intense Optical and Extreme-Ultraviolet Lasers with Atoms and Solids , PhD Thesis, Dublin City University,. 2009.

[113] P. Radcliffe, S. Düsterer, A. Azima, H. Redlin, J. Feldhaus, J. Dardis, K. Kavanagh, H. Luna, J.P. Gutierrez, P. Yeates, et al. Single-Shot Characterization of Independent Femtosecond Extreme Ultraviolet Free Electron and Infrared Laser pulses. *Applied Physics Letters*, 90:131108, 2007.

[114] A. Einstein. Über einen die Erzeugung und Verwandlung des Lichtes betreffenden heuristischen Gesichtspunkt. *Annalen der Physik*, 322(6):132–148, 1905.

[115] G.S. Voronov and N.B. Delone. Many-Photon Ionization of the Xenon Atom by Ruby Laser Radiation. *Soviet Journal of Experimental and Theoretical Physics*, 23:54, 1966.

[116] TM Barhudarova, GS Voronov, GA Delone, NB Delone, and NK Martakova. Multiphoton Ionization of the Noble Gas Atoms. In *Phenomena in Ionized Gases, VIII International Conference*, page 266, 1967.

[117] P. Agostini, G. Barjot, J. Bonnal, G. Mainfray, C. Manus, and J. Morellec. Multiphoton Ionization of Hydrogen and Rare Gases. *IEEE Journal of Quantum Electronics*, 4(10):667–669, 1968.

[118] W. Zernik. Two-Photon Ionization of Atomic Hydrogen. I. *Phys. Rev*, 135:A51, 1964.

[119] W. Zernik and R.W. Klopfenstein. Two-Photon Ionization of Atomic Hydrogen. II. *Journal of Mathematical Physics*, 6:262, 1965.

[120] P. Lambropoulos. Spin-Orbit Coupling and Photoelectron Polarization in Multiphoton Ionization of Atoms. *Phys. Rev. Lett.*, 30(10):413–416, Mar 1973.

[121] Lloyd Armstrong, P. Lambropoulos, and N. K. Rahman. Photon-Correlation Effects in Resonant Two-Photon Ionization. *Phys. Rev. Lett.*, 36(16):952–955, Apr 1976.

[122] P. Lambropoulos. Topics on Multiphoton Processes in Atoms. *Advances in Atomic and Molecular Physics*, 12:87–164, 1976.

[123] R.N. Compton, J.C. Miller, A.E. Carter, and P. Kruit. Resonantly Enhanced Multiphoton Ionization of Xenon: Photoelectron Energy Analysis. *Chemical Physics Letters*, 71(1):87–90, 1980.

[124] L. A. Lompre, G. Mainfray, C. Manus, and J. Thebault. Multiphoton Ionization of Rare Gases by a Tunable Wavelength 30-psec Laser Pulse at 1.06 μm. *Phys. Rev. A*, 15(4):1604–1612, Apr 1977.

[125] M.D. Perry and O.L. Landen. Resonantly Enhanced Multiphoton Ionization of Krypton and Xenon with Intense Ultraviolet Laser Radiation. *Physical Review A*, 38(6):2815–2829, 1988.

[126] Y. Gontier, M. Poirier, and M. Trahin. Multiphoton Absorptions Above the Ionisation Threshold. *Journal of Physics B: Atomic and Molecular Physics*, 13:1381, 1980.

[127] P. Lambropoulos. Reaching VUV Transitions with Multiphoton Processes. *Applied Optics*, 19(23):3926–3933, 1980.

[128] P. Agostini, M. Clement, F. Fabre, and G. Petite. Multiphoton Ionisation Involving Multiphoton Continuum-Continuum Transitions. *Journal of Physics B: Atomic and Molecular Physics*, 14:L491, 1981.

[129] T. S. Luk, H. Pummer, K. Boyer, M. Shahidi, H. Egger, and C. K. Rhodes. Anomalous Collision-Free Multiple Ionization of Atoms with Intense Picosecond Ultraviolet Radiation. *Phys. Rev. Lett.*, 51(2):110–113, Jul 1983.

[130] K. Boyer and C. K. Rhodes. Atomic Inner-Shell Excitation Induced by Coherent Motion of Outer-Shell Electrons. *Phys. Rev. Lett.*, 54(14):1490–1493, Apr 1985.

[131] A. Szöke and C.K. Rhodes. Theoretical Model of Inner-Shell Excitation by Outer-Shell Electrons. *Physical review letters*, 56(7):720–723, 1986.

[132] P. Lambropoulos and X. Tang. Multiple Excitation and Ionization of Atoms by Strong Lasers. *Journal of the Optical Society of America B*, 4(5):821–832, 1987.

[133] L.F. DiMauro, D. Kim, M.W. Courtney, and M. Anselment. Nonresonant Multiphoton Ionization of Calcium Atoms in an Intense Laser Field. *Physical Review A*, 38(5):2338–2346, 1988.

[134] Dalwoo Kim, S. Fournier, M. Saeed, and L. F. DiMauro. Magnesium Atoms in an Intense Nonresonant Laser Field. *Phys. Rev. A*, 41(9):4966–4973, May 1990.

[135] D. N. Fittinghoff, P. R. Bolton, B. Chang, and K. C. Kulander. Observation of Nonsequential Double Ionization of Helium with Optical Tunneling. *Phys. Rev. Lett.*, 69(18):2642–2645, Nov 1992.

[136] B. Walker, B. Sheehy, L. F. DiMauro, P. Agostini, K. J. Schafer, and K. C. Kulander. Precision Measurement of Strong Field Double Ionization of Helium. *Phys. Rev. Lett.*, 73(9):1227–1230, Aug 1994.

[137] D. N. Fittinghoff, P. R. Bolton, B. Chang, and K. C. Kulander. Polarization Dependence of Tunneling Ionization of Helium and Neon by 120 fs Pulses at 614 nm. *Phys. Rev. A*, 49(3):2174–2177, Mar 1994.

[138] P.B. Corkum. Plasma Perspective on Strong Field Multiphoton Ionization. *Physical Review Letters*, 71(13):1994–1997, 1993.

[139] P. Dietrich, N. H. Burnett, M. Ivanov, and P. B. Corkum. High-Harmonic Generation and Correlated Two-Electron Multiphoton Ionization with Elliptically Polarized Light. *Phys. Rev. A*, 50(5):R3585–R3588, Nov 1994.

[140] J. Ullrich, R. Moshammer, R. Dörner, O. Jagutzki, V. Mergel, H. Schmidt-Böcking, and L. Spielberger. Recoil-Ion Momentum Spectroscopy. *Journal of Physics B: Atomic, Molecular and Optical Physics*, 30:2917, 1997.

[141] N.A. Papadogiannis, L.A.A. Nikolopoulos, D. Charalambidis, GD Tsakiris, P. Tzallas, and K. Witte. Two-Photon Ionization of He Through a Superposition of Higher Harmonics. *Physical review letters*, 90(13):133902, 2003.

[142] Y. Nabekawa, H. Hasegawa, E.J. Takahashi, and K. Midorikawa. Production of Doubly Charged Helium Ions by Two-Photon Absorption of an Intense Sub-10-fs Soft X-ray Pulse at 42 eV Photon Energy. *Physical review letters*, 94(4):43001, 2005.

[143] N. Miyamoto, M. Kamei, D. Yoshitomi, T. Kanai, T. Sekikawa, T. Nakajima, and S. Watanabe. Observation of Two-Photon Above-Threshold Ionization of Rare Gases by XUV Harmonic Photons. *Physical Review Letters*, 93(8):83903, 2004.

[144] A. Rudenko, L. Foucar, M. Kurka, Th. Ergler, K. U. Kühnel, Y. H. Jiang, A. Voitkiv, B. Najjari, A. Kheifets, S. Lüdemann, T. Havermeier, M. Smolarski, S. Schössler, K. Cole, M. Schöffler, R. Dörner, S. Düsterer, W. Li, B. Keitel, R. Treusch, M. Gensch, C. D. Schröter, R. Moshammer, and J. Ullrich. Recoil-Ion Momentum Distributions for Two-Photon Double Ionization of He and Ne by 44 eV Free-Electron Laser Radiation. *Phys. Rev. Lett.*, 101(7):073003, Aug 2008.

[145] L.A.A. Nikolopoulos and P. Lambropoulos. Time-dependent Theory of Double Ionization of Helium Under XUV Radiation. *Journal of Physics B: Atomic, Molecular and Optical Physics*, 40:1347, 2007.

[146] M. Richter, M.Y. Amusia, S.V. Bobashev, T. Feigl, PN Juranić, M. Martins, A.A. Sorokin, and K. Tiedtke. Extreme Ultraviolet Laser Excites Atomic Giant Resonance. *Physical Review Letters*, 102(16):163002, 2009.

[147] J. P. Connerade, J. M. Esteva, and R. C. Karnatak. *Giant Resonances in Atoms, Molecules and Solids.* Plenum Press, New York and London, 1987.

[148] Eljko Crljen and Göran Wendin. Many-Body Theory of Effective Local Potentials for Electronic Excitations III. Application to Giant Dipole Resonances. *Phys. Rev. A*, 35(4):1571–1581, Feb 1987.

[149] J. H. D. Eland, O. Vieuxmaire, T. Kinugawa, P. Lablanquie, R. I. Hall, and F. Penent. Complete Two-Electron Spectra in Double Photoionization: The Rare Gases Ar, Kr, and Xe. *Phys. Rev. Lett.*, 90(5):053003, Feb 2003.

[150] B. W. Yates, K. H. Tan, L. L. Coatsworth, and G. M. Bancroft. High-Resolution Gas-Phase Photoelectron Spectra Using Synchrotron Radiation: Xe 4d Linewidths and the $4d_{5/2}$:$4d_{3/2}$ Branching Ratio. *Phys. Rev. A*, 31(3):1529–1534, Mar 1985.

[151] H. Aksela, S. Aksela, G. M. Bancroft, K. H. Tan, and H. Pulkkinen. $N_{4,5}OO$ Resonance Auger Spectra of Xe Studied with Selective Excitation by Synchrotron Radiation. *Phys. Rev. A*, 33(6):3867–3875, Jun 1986.

[152] A. Gottwald, Ch. Gerth, and M. Richter. $4d$ Photoionization of Free Singly Charged Xenon Ions. *Phys. Rev. Lett.*, 82(10):2068–2070, Mar 1999.

[153] S. Heinäsmäki, H. Aksela, J. Nikkinen, E. Kukk, A. Kivimäki, S. Aksela, and S. Fritzsche. Lifetime and Auger Decay of Strongly Correlated 4p Hole States of Xenon. *Journal of Electron Spectroscopy and Related Phenomena*, 137:281–285, 2004.

[154] http://physics.nist.gov/PhysRefData/ASD/levelsform.html. NIST Atomic Spectra Database.

[155] A. Kikas, SJ Osborne, A. Ausmees, S. Svensson, O.P. Sairanen, and S. Aksela. High-Resolution Study of the Correlation Satellites in Photoelectron Spectra of the Rare Gases. *Journal of Electron Spectroscopy and Related Phenomena*, 77(3):241–266, 1996.

[156] V. Richardson, J. T. Costello, D. Cubaynes, S. Düsterer, J. Feldhaus, H. W. van der Hart, P. Juranic, W.B. Li, M. Meyer, M. Richter, A.A. Sorokin, and K. Tiedke. Two-Photon Inner-Shell Ionization in the Extreme Ultraviolet. *Phys. Rev. Lett.*, 105(1):013001, Jun 2010.

[157] F. Wuilleumier and M. O. Krause. Photoionization of Neon Between 100 and 2000 eV: Single and Multiple Processes, Angular Distributions, and Subshell Cross Sections. *Phys. Rev. A*, 10(1):242–258, Jul 1974.

[158] L.O. Werme, T. Bergmark, and K. Siegbahn. The High Resolution $L_{2,3}MM$ and $M_{4,5}NN$ Auger Spectra from Krypton and $M_{4,5}NN$ and $N_{4,5}OO$ Auger Spectra from Xenon. *Physica Scripta*, 6:141, 1972.

[159] K. Siegbahn, C. Nordling, G. Johansson, J. Hedman, P.F. Heden, K. Hamrin, U. Gelius, T. Bergmark, L.O. Werme, R. Manne, et al. *ESCA Applied to Free Atoms*. North-Holland Amsterdam, 1969.

[160] V. Schmidt, N. Sandner, W. Mehlhorn, M. Y. Adam, and F. Wuilleumier. Post-Collision Interaction in the Xenon $N_{4,5}OO$ Auger Spectrum Excited by Photon Impact. *Phys. Rev. Lett.*, 38(2):63–66, Jan 1977.

[161] V. Schmidt, S. Krummacher, F. Wuilleumier, and P. Dhez. Post-Collision Interaction in Inner-Shell Ionization: The Xenon Case. *Phys. Rev. A*, 24(4):1803–1811, Oct 1981.

[162] W. Eberhardt, G. Kalkoffen, and C. Kunz. Measurement of the Auger Decay after Resonance Excitation of Xe $4d$ and Kr $3d$ Resonance Lines. *Phys. Rev. Lett.*, 41(3):156–159, Jul 1978.

[163] H. Aksela, S. Aksela, H. Pulkkinen, G. M. Bancroft, and K. H. Tan. Resonance Auger Decay After Selective Excitation of Kr 3d States by Synchrotron Radiation. *Phys. Rev. A*, 33(6):3876–3884, Jun 1986.

[164] H. Aksela, S. Aksela, G. M. Bancroft, K. H. Tan, and H. Pulkkinen. $N_{4,5}OO$ Resonance Auger Spectra of Xe Studied with Selective Excitation by Synchrotron Radiation. *Phys. Rev. A*, 33(6):3867–3875, Jun 1986.

[165] G.C. King, M. Tronc, F.H. Read, and R.C. Bradford. An Investigation of the Structure Near the $L_{2,3}$ Edges of argon, the $M_{4,5}$ Edges of Krypton and the $N_{4,5}$ Edges of Xenon, Using Electron Impact with High Resolution. *Journal of Physics B: Atomic and Molecular Physics*, 10:2479, 1977.

[166] Thomas A. Carlson, David R. Mullins, Charles E. Beall, Brian W. Yates, James W. Taylor, Dennis W. Lindle, B. P. Pullen, and Frederick A. Grimm. Unusual Degree of Angular Anisotropy in the Resonant Auger Spectrum of Kr. *Phys. Rev. Lett.*, 60(14):1382–1385, Apr 1988.

[167] Thomas A. Carlson, David R. Mullins, Charles E. Beall, Brian W. Yates, James W. Taylor, Dennis W. Lindle, and Frederick A. Grimm. Angular Distribution of Ejected Electrons in Resonant Auger Processes of Ar, Kr, and Xe. *Phys. Rev. A*, 39(3):1170–1185, Feb 1989.

[168] B. Kammerling, B. Krassig, and V. Schmidt. Connection Between the Angular Distribution of Auger Electrons and Spectator Autoionization Electrons Following 4d Ionization/ Excitation in Xenon. *Journal of Physics B: Atomic, Molecular and Optical Physics*, 23:4487, 1990.

[169] J. Tulkki, H. Aksela, and N. M. Kabachnik. Influence of the Initial- and Final-State Configuration Interaction on the Anisotropy of the Resonant Auger Decay of Kr $3d^{-1}5p$ and Xe $4d^{-1}6p$ States. *Phys. Rev. A*, 50(3):2366–2375, Sep 1994.

[170] H. Aksela, J. Jauhiainen, E. Nõmmiste, S. Aksela, S. Sundin, A. Ausmees, and S. Svensson. Angular Anisotropy of the Kr $3d^{-1}_{3/2,5/2}5p \rightarrow 4p^{-2}5p$ Resonant Auger Decay Studied by Utilizing the Auger Resonant Raman Effect. *Phys. Rev. A*, 54(1):605–612, Jul 1996.

[171] Zhen-Sheng Yuan, Lin-Fan Zhu, Xiao-Jing Liu, Wen-Bin Li, Hua-Dong Cheng, Jian-Min Sun, and Ke-Zun Xu. Inner-Shell Excitations of Krypton $3d$ Investigated by Electron Impact with High Resolution. *Phys. Rev. A*, 71(6):064701, Jun 2005.

[172] L.F. DiMauro and P. Agostini. Ionization Dynamics in Strong Laser Fields. *Advances in Atomic, Molecular, and Optical Physics*, 35:79–120, 1995.

[173] Carsten Winterfeldt, Christian Spielmann, and Gustav Gerber. Colloquium: Optimal Control of High-Harmonic Generation. *Rev. Mod. Phys.*, 80(1):117–140, Jan 2008.

[174] W. Becker, F. Grasbon, R. Kopold, D.B. Milosevic, G.G. Paulus, and H. Walther. Above-threshold Ionization: From Classical Features to Quantum Effects. *Advances In Atomic, Molecular, and Optical Physics*, 48:35–98, 2002.

[175] http://xfel.desy.de.

[176] http://lcls.slac.stanford.edu.

[177] M. Kurka, A. Rudenko, L. Foucar, K.U. Kühnel, Y.H. Jiang, T. Ergler, T. Havermeier, M. Smolarski, S. Schössler, K. Cole, et al. Two-Photon Double Ionization of Ne by Free-Electron Laser Radiation: a Kinematically Complete Experiment. *Journal of Physics B: Atomic, Molecular and Optical Physics*, 42:141002, 2009.

[178] R. Moshammer, Y.H. Jiang, L. Foucar, A. Rudenko, T. Ergler, CD Schröter, S. Lüdemann, K. Zrost, D. Fischer, J. Titze, et al. Few-Photon Multiple Ionization of Ne and Ar by Strong Free-Electron-Laser Pulses. *Physical Review Letters*, 98(20):203001, 2007.

[179] R. Mitzner, A.A. Sorokin, B. Siemer, S. Roling, M. Rutkowski, H. Zacharias, M. Neeb, T. Noll, F. Siewert, W. Eberhardt, M. Richter, P. Juranic, K. Tiedtke, and J. Feldhaus. Direct Autocorrelation of Soft X-ray Free-Electron-Laser Pulses by Time-Resolved Two-Photon Double Ionization of He. *Phys. Rev. A*, 80(2):025402, Aug 2009.

[180] M. Meyer, D. Cubaynes, V. Richardson, JT Costello, P. Radcliffe, WB Li, S. Düsterer, S. Fritzsche, A. Mihelic, KG Papamihail, et al. Two-Photon Excitation and Relaxation of the 3d-4d Resonance in Atomic Kr. *Physical Review Letters*, 104(21):213001, 2010.

[181] F.A. Parpia, C.F. Fischer, and I.P. Grant. GRASP92: A Package for Large-Scale Relativistic Atomic Structure Calculations. *Computer physics communications*, 94(2-3):249–271, 1996.

[182] S. Fritzsche. RATIP - A Toolbox for Studying the Properties of Open-Shell Atoms and Ions. *Journal of Electron Spectroscopy and Related Phenomena*, 114:1155–1164, 2001.

[183] M. Meyer, D. Cubaynes, J. Dardis, P. Hayden, P. Hough, V. Richardson, ET Kennedy, JT Costello, S. Düsterer, WB Li, et al. Two-Color Experiments in the Gas Phase at FLASH. *Journal of Electron Spectroscopy and Related Phenomena*, 181, p.111-115, 2010.

[184] M. Meyer, JT Costello, S. Düsterer, WB Li, and P. Radcliffe. Two-Colour Experiments in the Gas Phase. *Journal of Physics B: Atomic, Molecular and Optical Physics*, 43:194006, 2010.

[185] E.S. Toma, H.G. Muller, P.M. Paul, P. Breger, M. Cheret, P. Agostini, C. Le Blanc, G. Mullot, and G. Cheriaux. Ponderomotive Streaking of the Ionization Potential as a Method for Measuring Pulse Durations in the XUV Domain with fs Resolution. *Physical Review A*, 62(6):61801, 2000.

[186] L.A.A. Nikolopoulos. upcoming work. 2010.

[187] U. Fano. Propensity rules: An Analytical Approach. *Physical Review A*, 32(1):617–618, 1985.

[188] N. Berrah, J. Bozek, JT Costello, S. Dusterer, L. Fang, J. Feldhaus, H. Fukuzawa, M. Hoener, YH Jiang, P. Johnsson, et al. Non-Linear Processes in the Interaction of Atoms and Molecules With Intense EUV and X-ray Fields From SASE Free Electron Lasers (FELs). *Journal of Modern Optics*, 57(12):10151040, 2010.

[189] J.T. Costello. Photoionization Experiments with the Ultrafast EUV Laser'FLASH'-Free Electron Laser in Hamburg. In *Journal of Physics: Conference Series*, volume 88, page 012057. IOP Publishing, 2007.

[190] C. Bostedt, H.N. Chapman, J.T. Costello, J.R. Crespo López-Urrutia, S. Düsterer, S.W. Epp, J. Feldhaus, A. Föhlisch, M. Meyer, T. Möller, et al. Experiments at FLASH. *Nuclear Inst. and Methods in Physics Research, A*, 601(1-2):108–122, 2009.

[191] A.A. Sorokin, M. Wellhöfer, SV Bobashev, K. Tiedtke, and M. Richter. X-Ray-Laser Interaction with Matter and the Role of Multiphoton Ionization: Free-Electron-Laser Studies on Neon and Helium. *Physical Review A*, 75(5):51402, 2007.

[192] S. Cunovic, N. Müller, R. Kalms, M. Krikunova, M. Wieland, M. Drescher, T. Maltezopoulos, U. Frühling, H. Redlin, E. Plönjes-Palm, et al. Time-to-Space Mapping in a Gas Medium for the Temporal Characterization of Vacuum-Ultraviolet Pulses. *Applied Physics Letters*, 90:121112, 2007.

[193] T. Shintake, H. Tanaka, T. Hara, T. Tanaka, K. Togawa, M. Yabashi, Y. Otake, Y. Asano, T. Bizen, T. Fukui, et al. A Compact Free-Electron Laser for Generating Coherent Radiation in the Extreme Ultraviolet Region. *Nature Photonics*, 2(9):555–559, 2008.

[194] P. Emma, R. Akre, J. Arthur, R. Bionta, C. Bostedt, J. Bozek, A. Brachmann, P. Bucksbaum, R. Coffee, F.J. Decker, et al. First Lasing and Operation of an Angstrom-Wavelength Free-Electron Laser. *Nature Photonics*, 4(9):641–647, 2010.

[195] A. Rudenko, L. Foucar, M. Kurka, T. Ergler, KU Kühnel, Y.H. Jiang, A. Voitkiv, B. Najjari, A. Kheifets, S. Lüdemann, et al. Recoil-Ion momentum Distributions for Two-Photon Double Ionization of He and Ne by 44 eV Free-Electron Laser Radiation. *Physical Review Letters*, 101(7):73003, 2008.

[196] M. Kurka, J. Feist, DA Horner, A. Rudenko, YH Jiang, KU Kühnel, L. Foucar, TN Rescigno, CW McCurdy, R. Pazourek, et al. Differential Cross Sections for Non-Sequential Double Ionization of He by 52 eV Photons from the Free Electron Laser in Hamburg, FLASH. *New Journal of Physics*, 12:073035, 2010.

[197] H. Fukuzawa, E.V. Gryzlova, K. Motomura, A. Yamada, K. Ueda, A.N. Grum-Grzhimailo, S.I. Strakhova, K. Nagaya, A. Sugishima, Y. Mizoguchi, et al. Photoelectron Spectroscopy of Sequential Three-Photon Double Ionization of Ar Irradiated by EUV Free-Electron Laser Pulses. *Journal of Physics B: Atomic, Molecular and Optical Physics*, 43:111001, 2010.

[198] T. E. Glover, R. W. Schoenlein, A. H. Chin, and C. V. Shank. Observation of Laser Assisted Photoelectric Effect and Femtosecond High Order Harmonic Radiation. *Phys. Rev. Lett.*, 76(14):2468–2471, Apr 1996.

[199] J. M. Schins, P. Breger, P. Agostini, R. C. Constantinescu, H. G. Muller, G. Grillon, A. Antonetti, and A. Mysyrowicz. Laser-Assisted Auger Decay as Free-Free Transitions in a High-Intensity Laser Field. *Phys. Rev. A*, 52(2):1272–1278, Aug 1995.

[200] O. Guyétand, M. Gisselbrecht, A. Huetz, P. Agostini, R. Taieb, V. Véniard, A. Maquet, L. Antonucci, O. Boyko, C. Valentin, et al. Multicolour Above-Threshold Ionization of Helium: Quantum Interference Effects in Angular Distributions. *Journal of Physics B: Atomic, Molecular and Optical Physics*, 38(22):357, 2005.

[201] P. O'Keeffe, R. López-Martens, J. Mauritsson, A. Johansson, A. L'Huillier, V. Véniard, R. Taïeb, A. Maquet, and M. Meyer. Polarization Effects in Two-Photon Nonresonant Ionization of Argon with Extreme-Ultraviolet and Infrared Femtosecond Pulses. *Phys. Rev. A*, 69(5):051401, May 2004.

[202] L.H. Haber, B. Doughty, and S.R. Leone. Photoelectron Angular Distributions and Cross Section Ratios of Two-Color Two-Photon Above Threshold Ionization of Argon. *J. Phys. Chem. A*, 113(47):13152–13158, 2009.

[203] L.H. Haber and B. Doughty. Photoelectron Angular Distributions and Cross Section Ratios of Two-Color Two-Photon Above Threshold Ionization of Helium. *Mol. Phys*, 108(7):1241, 2010.

[204] M. Meyer, D. Cubaynes, D. Glijer, J. Dardis, P. Hayden, P. Hough, V. Richardson, ET Kennedy, JT Costello, P. Radcliffe, et al. Polarization Control in Two-Color Above-Threshold Ionization of Atomic Helium. *Physical Review Letters*, 101(19):193002, 2008.

[205] A. Maquet and R. Taieb. Two-Colour IR+XUV Spectroscopies: The Soft-Photon Approximation. *Journal of Modern Optics*, 54(13):1847–1857, 2007.

[206] J. M. Bizau, D. Cubaynes, M. Richter, F. J. Wuilleumier, J. Obert, J. C. Putaux, T. J. Morgan, E. Kallne, S. Sorensen, and A. Damany. First Observation of Photoelectron Spectra Emitted in the Photoionization of a Singly Charged Ion Beam with Synchrotron Radiation. *Phys. Rev. Lett.*, 67(5):576–579, Jul 1991.

[207] A. Gottwald, Ch. Gerth, and M. Richter. 4d Photoionization of Free Singly Charged Xenon Ions. *Phys. Rev. Lett.*, 82(10):2068–2070, Mar 1999.

[208] M. Förstel, B. Jordon-Thaden, C. Domesle, T. Arion, T. Lischke, M. Mucke, L. Lammich, HB Pedersen, S. Klumpp, M. Martins, et al. Electron Spectroscopy on an Ion Beam at FLASH, Hasylab Annual Report, 2009.

[209] M. Braune, A. Reinköster, J. Viefhaus, B. Lohmann, and U. Becker. Photoelectron Spectroscopy of Rare Gas Atoms Following Multi-Photon Ionization by FEL Radiation, Hasylab Annual Report, 2009.

[210] L.A.A. Nikolopoulos and P. Lambropoulos. Multichannel theory of two-photon single and double ionization of helium. *Journal of Physics B: Atomic, Molecular and Optical Physics*, 34:545, 2001.

[211] L. A. A. Nikolopoulos, Takashi Nakajima, and P. Lambropoulos. Direct versus Sequential Double Ionization of Mg with Extreme-Ultraviolet Radiation. *Phys. Rev. Lett.*, 90(4):043003, Jan 2003.

[212] A.I. Magunov, I. Rotter, and S.I. Strakhova. Strong Laser Field Effects in Autoionization. *Journal of Physics B: Atomic, Molecular and Optical Physics*, 32:1489, 1999.

[213] S.I. Themelis, P. Lambropoulos, and M. Meyer. Ionization Dynamics in Double Resonance Involving Autoionizing States in Helium: The Effect of Pulse Shapes. *Journal of Physics B: Atomic, Molecular and Optical Physics*, 37:4281, 2004.

[214] S.I. Themelis, P. Lambropoulos, and F.J. Wuilleumier. Laser-Induced Transitions Between Core Excited States of Na. *Journal of Physics B: Atomic, Molecular and Optical Physics*, 38:2119, 2005.

[215] N. E. Karapanagioti, D. Charalambidis, C. J. G. J. Uiterwaal, C. Fotakis, H. Bachau, I. Sánchez, and E. Cormier. Effects of Coherent Coupling of Autoionizing States on Multiphoton Ionization. *Phys. Rev. A*, 53(4):2587–2597, Apr 1996.

[216] H.W. van der Hart V. Richardson et al. upcoming work, 'Two and Three Photon Sequential Ionization of Neon in the Extreme Ultraviolet'. 2010.

[217] L.H. Haber, B. Doughty, and S.R. Leone. Photoelectron Angular Distributions and Cross Section Ratios of Two-Color Two-Photon Above Threshold Ionization of Argon. *J. Phys. Chem. A*, 113(47):13152–13158, 2009.

[218] L.H. Haber and B. Doughty. Photoelectron Angular Distributions and Cross Section Ratios of Two-Color Two-Photon Above Threshold Ionization of Helium. *Mol. Phys*, 108(7):1241, 2010.

[219] T. Prescher, M. Richter, E. Schmidt, B. Sonntag, and H.E. Wetzel. Decay of the Giant 4d Photoabsorption Resonance in Atomic Cs and Sm. *Journal of Physics B: Atomic and Molecular Physics*, 19:1645, 1986.